Test of the QCD Vacuum with the Sources in Higher Representations[1]

Yu. A. Simonov

Institute of Theoretical and Experimental Physics, Bol'shaya Cheremushkinskaya ul. 25, Moscow, 117259 Russia
Received December 20, 1999; in final form, January 20, 2000

Abstract—Recent accurate measurements [1, 2] of the static potentials between sources in various SU(3) representations provide a crucial test of the QCD vacuum and of different theoretical approaches to the confinement. In particular, the Casimir scaling of static potentials found for all measured distances implies strong suppression of higher cumulants and a high accuracy of the Gaussian stochastic vacuum. Most popular models are in conflict with these measurements. © 2000 MAIK "Nauka/Interperiodica".

PACS numbers: 12.38.Aw; 02.20.Qs

Recent accurate measurements of the static potentials between sources in the eight different representations of the SU(3) group [1] reveal a new quantitative picture of QCD vacuum and provide a crucial test of existing theoretical models. Other measurements of static interaction [2] are in general agreement with [1].

The most convenient way of writing static potentials $V_D(r)$ in the representations $D = 3, 8, 6, 15a, 10, 27, 24$, and 15s is to express them through a complete set of field correlators in the framework of the Field Correlator Method (FCM) [3]:

$$V_D(r) = -\lim_{T \to \infty} \frac{1}{T} \ln \langle W(C) \rangle, \qquad (1)$$

where the Wilson loop $W(C)$ for the rectangular contour $C = r \times T$ in the (34) plane is written as a cumulant expansion

$$\langle W(C) \rangle = Tr_D \exp \int_S \sum_{n=2,4\ldots} (ig)^n \qquad (2)$$
$$\times \langle\langle F(1)F(2)\ldots F(n) \rangle\rangle d\sigma(1)\ldots d\sigma(n).$$

Here $F(k)d\sigma(k) = F_{34}(u^{(k)}, x_0)d\sigma_{34}(k)$ and the component $F_{34}(u, x_0) \equiv E_3(u, x_0) = \phi(x_0, u)E_3(u)\phi(u, x_0)$, where ϕ is the parallel transporter and x_0 is an arbitrary point on the surface S inside the contour C; $Tr_D \hat{1} = 1$.

Equation (2) depends on D through the generators T^a, because $F(k) = F^a(k)T^a$ ($a = 1, \ldots, N_c^2 - 1$) and the quadratic Casimir operator C_D, $T^aT^a = \hat{1}C_D$, is the main characteristic of D, so that the invariant square of color charge in the representation D is $g^2 C_D$.

One can now express the connected correlators (cumulants) in (2) via C_D and D-independent averages as follows (for more details, see the last reference in [3] and [4]):

$$Tr_D \langle F(1)F(2) \rangle = C_D \frac{\langle F^a(1)F^a(2) \rangle}{N_c^2 - 1}, \qquad (3)$$

$$Tr_D \langle\langle F(1)F(2)F(3)F(4) \rangle\rangle$$

$$= \frac{C_D^2}{(N_c^2 - 1)^2} \Big\{ \langle F^a(1)F^a(2)F^b(3)F^b(4) \rangle$$

$$+ \langle F^a(1)F^b(2)F^b(3)F^a(4) \rangle \qquad (4)$$

$$- \langle F^a(1)F^a(2) \rangle \langle F^b(3)F^a(4) \rangle$$

$$+ \left(1 - \frac{N_c}{2C_D}\right) \langle F^a(1)F^b(2)F^a(3)F^b(4) \rangle \Big\} + O\left(\frac{1}{N_c^2}\right).$$

Note that the arguments of $F(k)$ in (4) and in (2) are ordered [e.g., clockwise, $u^{(1)} < u^{(2)} < u^{(3)} < u^{(4)}$] and, therefore, only the vacuum insertion is possible in the first term on the rhs of (4), leading to the mutual cancellation of the first and the third terms; hence, (4) is a connected correlator vanishing at large distances $|u^{(1)} + u^{(2)} - u^{(3)} - u^{(4)}| \longrightarrow \infty$.

In a similar manner, one can show that the nth cumulant in (2) contributes proportionally to C_D^n. As a result, the static potential $V_D(r)$ can be expanded as

$$V_D(r) = d_D V^{(2)}(r) + d_D^2 V^{(4)}(r) + \ldots, \qquad (5)$$

where [1] $d_D = C_D/C_F$ and C_F is the fundamental Casimir operator $C_F = (N_c^2 - 1)/2N_c$. The fundamental

---

static potential contains a perturbative Coulomb part V_{Coul}, confining linear and constant terms.

The Coulomb part, which can be obtained from the perturbative contribution to FC, is known up to two loops [5] and is proportional to C_D. Therefore, one may expect quartic contributions proportional to $C_D^2 \sim d_D^2$, to the constant and linear terms, writing (5) as

$$V_D(r) = d_D V^{(2)}(r) + d_D^2 (\overline{v}_0^{(4)} + \overline{\sigma}_4 r). \qquad (6)$$

Here, $\overline{v}_0$ and $\overline{\sigma}_4$ measure the contribution of the quartic cumulants to the constant term and string tension, respectively.

The measurements in [1] allow one to find $\overline{v}_0$ and $\overline{\sigma}_4$ from all eight data sets. To this end, one forms seven combinations $\zeta_D \equiv V_D(r) - d_D V_F(r) = d_D(d_D - 1)(\overline{v}_0^{(4)} + \overline{\sigma} r)$. As a typical example, take fundamental and adjoint potentials at distances r in the interval between 0.05 and 1.1 fm from the data [1] and the χ^2 fit yields for $\overline{v}_0$, $\overline{\sigma}_4$:

$$\overline{v}_0^{(4)} = (-0.6 \pm 0.67) \times 10^{-3} \text{ GeV}, \qquad (7)$$

$$\overline{\sigma}^{(4)} = (-2 \pm 0.69) \times 10^{-3} \text{ GeV}^2. \qquad (8)$$

The quality of the fit is reasonable: $\chi^2/N = 0.45$, $N = 43$. One obtains similar results for $D = 6$, 15a, and 10 (while three higher representations do not provide additional information), suggesting that $\overline{\sigma}^{(4)}$ is negative and $\overline{v}_0^{(4)}$ is compatible with zero, confirming in this way parametrization (6).

This analysis demonstrates the phenomenon of Casimir scaling, i.e., proportionality of the static potential $V_D(r)$ to the Casimir operator C_D with an accuracy better than one percent.

Physical consequences of the Casimir scaling are numerous and important.

First of all, the sign and magnitude of quartic correction (7), (8) can be understood in the framework of the FCM. Indeed, the quartic term enters the potential V_D with the factor $(-g^4)$, as compared to $+g^2$ for the quadratic (Gaussian) term. Second, estimate the $\langle E_3^2 \rangle$ term from the standard gluonic condensate as follows:

$$g^2 \langle E_3^a E_3^a \rangle \sim \frac{4\pi^2}{12}(0.04 \pm 0.02)$$
$$\sim (0.10 \pm 0.06) \text{ GeV}^4 \qquad (9)$$

and take into account that the cumulant expansion in (2) is actually in powers of the parameter

$$\xi \equiv g^2 \langle E_3^a E_3^a \rangle T_g^4. \qquad (10)$$

Here, T_g is the correlation length of the QCD vacuum; for bilocal correlator it was measured on the lattice [6] $T_g^{(2)} \sim 1$ GeV^{-1}. With the use of (10), one could expect that $\overline{\sigma}_4$ would be from 4 to 10% of the standard string tension, $\sigma = 0.2$ GeV^2 provided $T_g = T_g^{(2)}$. The value of $\overline{\sigma}^{(4)}$ calculated in (8) is at least six times smaller and suggests that the quartic correlation length $T_g^{(4)}$ may be smaller than the Gaussian one, $T_g^{(2)} \sim 0.2$ fm.

This result means that the Gaussian Stochastic Model (GSM), suggested in [3] and successfully used heretofore in many applications [7], can be more accurate than was even expected, at least in the processes where string tension plays the most important role. On the other hand, the smallness of quartic and higher contributions implies a very specific picture of vacuum correlations.

Indeed, the smallness of $T_g^{(4)}$ implies that color fields tend to form compact white bilocal combinations $F^a(1)F^a(2)$ which are almost noninteracting between themselves and therefore not contributing to the higher connected correlators. This looks like the picture of small white dipoles made of fields FF (or of vector potentials $A_\mu A_\mu$ connected to FF in the Fock–Schwinger or contour gauge).

One can also understand qualitatively the difference between $T_g^{(2)}$ and $T_g^{(4)}$, since $T_g^{(2)}$ measures correlation length between adjoint fields $E_3^a(x)$ and $E_3^a(y)$ in the Gaussian correlator $\langle E_3^a(x) E_3^a(y) \rangle$, while $T_g^{(4)}$ refers to the correlation of two white complexes and should be connected to the lowest glueball mass $M_G \approx 2$ GeV; hence, $T_g^{(4)} \sim 1/M_G \sim 0.1$ fm $< T_g^{(2)}$.

Finally, the Casimir scaling imposes severe restrictions on the existing models of QCD vacuum. For example, the center-symmetry flux model was tested and ruled out in [1], since in the original formulation it predicts vanishing adjoint string tension, whereas in the later modification, the fat vertex model [9], it is still far from the accurate data [1].

Next, one should mention models of the Abelian projected vacuum which fail to provide Casimir scaling [11], at least in the simplest version [12].

Consider now a dilute instanton gas model and the SU(2) group. The instantons may be present in the confining vacuum as an important source of chiral symmetry breaking. Then the Casimir scaling [1] imposes a strict bound on the admixture of instantons in the QCD vacuum. Indeed, insertion in (2) and (4) of the instanton field strength $g F_{34}^a(x, z) = 4\delta_{a3}\rho^2/[(x - z)^2 + \rho^2]^2$, ($\rho$ is the instanton size and z is its position; the contribution of the parallel transporters is neglected for simplicity,

since it gives a reduction of 20–30% for bilocal correlators, see [11] for details) yields the following expression for the quartic contribution to the potential generated by instantons at small distances $r \leq \rho$ [in the SU(2) group]:

$$V_D^{(4)} = -\frac{N}{V}\frac{r^4}{\rho}\frac{\pi^6}{320}\frac{3C_D^2 - C_D}{15}, \qquad (11)$$

where N/V is the instanton density in the vacuum. With the limit (8) on $\bar{v}_0^{(4)}$ and taking the distance $r = \rho = 0.3$ fm, one obtains an upper bound for density of instantons:

$$N/V \leq 0.2 \text{ fm}^{-4}, \qquad (12)$$

which is much smaller than the normal instanton density of 1 fm^{-4}.

With such density, the role of instantons in chiral symmetry breaking and other effects would be rather small. Even more stringent bounds can be obtained from the quartic string tension; however, the nonzero value of $\bar{\sigma}_4$ for instantons does not imply confinement. One should take into account that at large distances the sum of all partial string tensions $\sum_{n = 2, 4, \ldots} \bar{\sigma}^{(n)}$ for the dilute instanton gas vanishes [12, 13].

In the previous discussion, we ignored the fact that at large enough distances the adjoint charges are screened by the vacuum gluons, and the limiting value of the adjoint potential is equal to the doubled gluelump mass $2M_{gl}$. This leads to an estimate of the screening distance r_0 from the relation $V_{adj}(r_0) = 2M_{gl}$, where M_{gl} from [4] is around 1.4 GeV and, therefore, $r_0 \approx 1.4$ fm, which is beyond the distance where Casimir scaling was measured in [1].

Thus, the Casimir scaling is a stringent test for all models considered and displays a strong suppression of quartic and higher correlators and, hence, supports a good accuracy of the GSM. At this point one may wonder how, with negligibly small higher FCs one can have a screening regime at $r > r_0$. The answer was suggested in [14], where it was demonstrated that screening terms appear as an additive contribution to the Wilson loop, which is not included in the cumulant expansion (2) and has a small coefficient $O(N_c^{-2})$. Therefore, the transition from the Casimir scaling regime to the screening regime occurs sharply at large T and $r = r_0$ due to the definition of the static potential (1) and cannot be seen in the one-loop cumulant expansion in (2). For details, the reader is referred to [4] and subsequent papers.

REFERENCES

1. G. Bali, hep-lat/9908021.
2. N. A. Campbell, I. H. Jorysz, and C. Michael, Phys. Lett. B **167**, 91 (1986); C. Michael, Nucl. Phys. B (Proc. Suppl.) **26**, 417 (1992); C. Michael, hep-ph/9809211; S. Deldar, hep-lat/9809137; hep-lat/9909077.
3. H. G. Dosch, Phys. Lett. B **190**, 177 (1987); H. G. Dosch and Yu. A. Simonov, Phys. Lett. B **205**, 339 (1988); Yu. A. Simonov, Nucl. Phys. B **307**, 512 (1988); Yu. A. Simonov, Usp. Fiz. Nauk **166**, 337 (1996) [Phys. Usp. **39**, 313 (1996)].
4. V. I. Shevchenko and Yu. A. Simonov, submitted to Phys. Rev. Lett.
5. M. Peter, Phys. Rev. Lett. **78**, 602 (1997); Nucl. Phys. B **501**, 471 (1997); Y. Schroeder, Phys. Lett. B **447**, 321 (1999).
6. A. Di Giacomo and H. Panagopoulos, Phys. Lett. B **285**, 133 (1992); A. Di Giacomo, E. Meggiolaro, and H. Panagopoulos, Nucl. Phys. B **483**, 371 (1997); M. D'Elia, A. Di Giacomo, and E. Meggiolaro, Phys. Lett. B **408**, 315 (1997).
7. Yu. A. Simonov, Yad. Fiz. **54**, 192 (1991) [Sov. J. Nucl. Phys. **54**, 115 (1991)]; H. G. Dosch, Prog. Part. Nucl. Phys. **33**, 121 (1994); O. Nachtmann, Lect. Notes Phys. **479**, 49 (1996); Yu. A. Simonov, hep-ph/9911237.
8. M. Faber, J. Greensite, and Š. Olejnik, Phys. Rev. D **57**, 2603 (1998); hep-lat/9710039; S. Deldar, hep-ph/9912428.
9. L. Del Debbio, M. Faber, J. Greensite, and Š. Olejnik, Phys. Rev. D **53**, 5891 (1996).
10. G. Poulis, Phys. Rev. D **54**, 6974 (1996); hep-lat/9608054.
11. E. M. Ilgenfritz, B. V. Martemyanov, S. V. Molodtsov, *et al.*, Phys. Rev. D **58**, 114508 (1998).
12. Yu. A. Simonov, Yad. Fiz. **50**, 500 (1989) [Sov. J. Nucl. Phys. **50**, 310 (1989)].
13. C. G. Callan, R. Dashen, and D. J. Gross, Phys. Lett. B **66**, 375 (1977); A. I. Veselov and M. I. Polikarpov, Pis'ma Zh. Éksp. Teor. Fiz. **45**, 113 (1987) [JETP Lett. **45**, 139 (1987)]; D. I. Diakonov, V. Yu. Petrov, and P. V. Pobylitsa, Phys. Lett. B **226**, 471 (1989); E. V. Shuryak, Nucl. Phys. B **328**, 85, 102 (1989).
14. J. Greensite and M. B. Halpern, Phys. Rev. D **27**, 2545 (1983).

Self-Reconstruction of an Optical Vortex

M. V. Vasnetsov*, I. G. Marienko, and M. S. Soskin

Institute of Physics, National Academy of Sciences of Ukraine, pr. Nauki 144, Kiev, 252650 Ukraine
*e-mail: mvas@marion.iop.kiev.ua

Abstract—The results of experiments devoted to the diffraction of a light beam with an axial optical vortex from the edge of an opaque screen are presented. The reconstruction of an optical vortex in the transmitted beam is observed under conditions when the screen cuts off the central part of the incident beam. © *2000 MAIK "Nauka/Interperiodica"*.

PACS numbers: 42.25.Fx

Currently, optical vortices (OVs), i.e., areas of circular motion of energy flow in an electromagnetic wave, are being actively studied in optics. Optical vortices can be divided into longitudinal OVs, where the axis of circular motion coincides with the direction of wave propagation (or is slightly tilted with respect to this direction), and transverse OVs, where the axis is perpendicular to the wave propagation. Laguerre–Gauss doughnut LG_0^{-1} modes of a laser cavity [1] are typical examples of longitudinal OVs. Airy rings in the focal plane of a lens [2] may serve as an example of transverse OVs. In both cases, the OV axis coincides with the line where the field amplitude is equal to zero. Going around the OV axis along any closed contour not enclosing another OV, we find that the phase is changed by 2π or $2m\pi$ in the case of an m-fold vortex. For a longitudinal OV, the integer $m\pi$ is called the topological charge of the vortex. Due to the $m\pi$ jump, the phase is assumed to be uncertain, or singular, along the OV axis.

In the case of a longitudinal OV, a combination of circular and translational motion of energy in the electromagnetic wave gives rise to the formation of a helicoidal surface of equal phase (helical wave-front dislocation) [3, 4]. The surface of the wave front under these conditions is smooth everywhere except for the helicoid axis. In the case of coaxial interference with a plane wave, the wave surface with such a shape gives rise to spiral interference fringes and a "fork" of interference fringes for oblique-incidence waves. The appearance of such a fork unambiguously indicates the presence of an OV [4]. An important specific feature of longitudinal OVs is that a light beam may have a nonzero orbital angular momentum, which can be transferred to particles trapped inside the beam, leading to the rotation of such particles [5, 6].

As shown earlier [7], the screening of the peripheral part of the beam does not suppress an OV in the transmitted beam but shifts the OV with respect to the beam center due to the existence of partial sources with a

π-shifted phase. However, it is not clear whether an OV can survive in the case when the central part of the beam is cut off, since, in such a situation, there are no reasons for destructive interference of partial sources on the wave front, which is necessary for the appearance of a zero point of the field amplitude.

The purpose of this letter is to describe the regeneration of a longitudinal OV, i.e., the reconstruction of an OV with a phase-singularity point from the smooth part of the wave front. The main idea of our experimental and numerical studies was to cut off the central part of a beam including the axis of an axial OV with an opaque screen.

Figure 1 presents the results of numerical simulations of OV regeneration in a beam represented in the $z = 0$ plane as the waist of an LG_0^1 mode of a beam where the central part is cut off with a screen,

$$E(x, y)$$
$$= \begin{cases} 0, & y \le y_0 \\ \sqrt{(x^2 + y^2)}\exp[-(x^2 + y^2)/r_0^2 + i\varphi], & y > y_0. \end{cases} \quad (1)$$

Here, r_0 is the transverse size parameter; φ is the azimuthal angle, which is equal to $\arctan(x/y)$; $y = y_0$ is the cutoff line of the beam transmitted through an opaque screen; and $y_0 = \frac{1}{3}r_0$. The fact that formula (1) involves the phase factor $\exp(i\varphi)$ implies that we are dealing with an axial OV with the charge $m = 1$. As can be seen from (1), a beam diaphragmed by a half-plane with $y_0 > 0$ (the dashed line in Fig. 1 shows the edge of the screen blocking the lower part of the beam) contains only the peripheral part, which involves no phase singularity. However, the phase of such a beam varies in its cross section in accordance with (1). The images presented at the left of Fig. 1 display intensity distributions in the cross section of the beam. The dashed circle
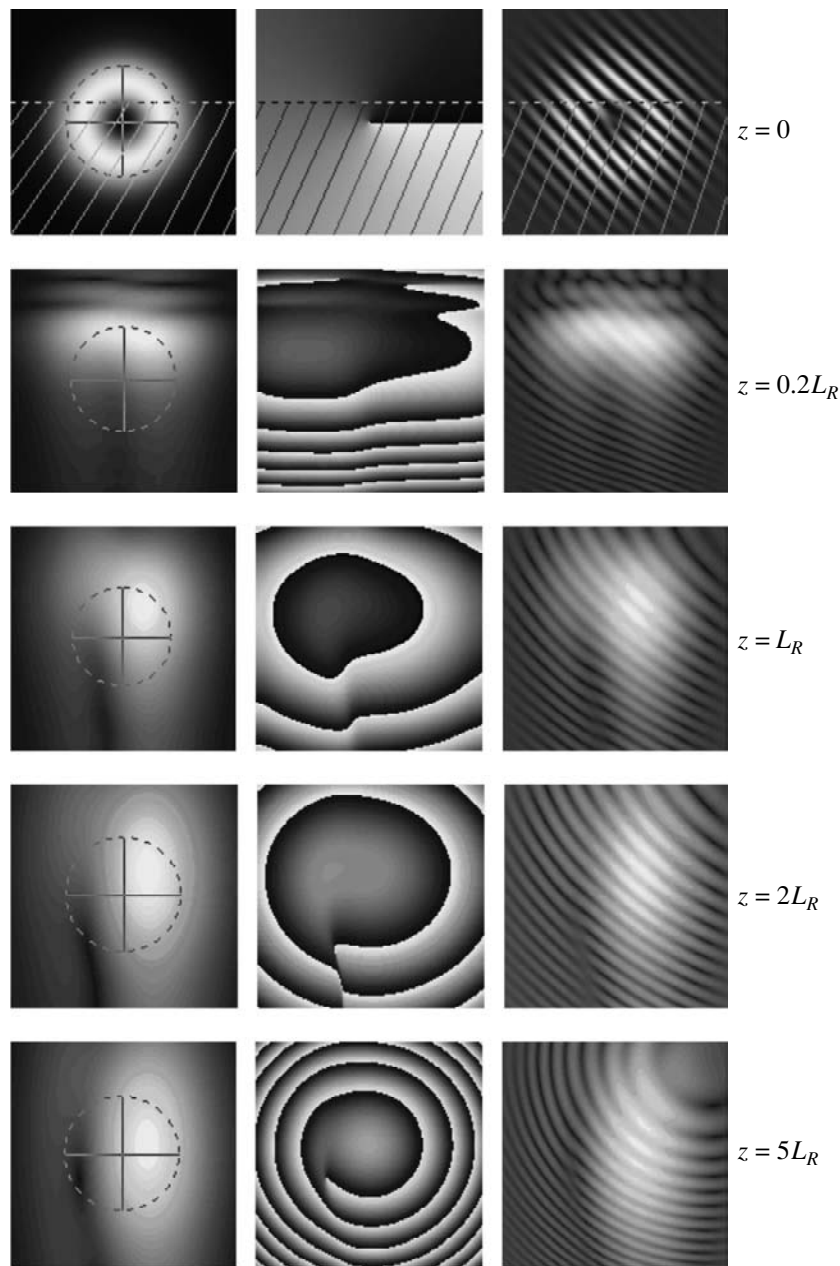
Fig. 1. Results of calculations for (left) intensity distributions in the transverse section of a beam with an axial OV with $m = -1$ at different distances behind the screen cutting off the dashed part of the beam at $z = 0$ (upper row), (center) the corresponding phase distributions, and (right) patterns of interference with a plane wave. The transverse size of an unperturbed beam for the same distances is shown with a dashed circle.

shows the current size of a freely propagating beam. The wave phase is represented by levels of gray scale in the central part of Fig. 1 (with black corresponding to a zero phase and white corresponding to the phase equal to 2π). The patterns corresponding to interference with an off-axis plane wave are shown at the right of Fig. 1.

As the beam propagates behind the screen, the light is diffracted to the area of geometric shadow, which is accompanied by the rotation of the light spot as a whole. The direction of this rotation is determined by

the sign of the OV charge [4]. The phase structure in the cross section of the beam in the near-field zone changes considerably under these conditions (the distance along the z-axis is normalized to the Rayleigh length of an unperturbed beam, $L_R = \pi r_0^2/\lambda$, where λ is the wavelength). For distances less than the Rayleigh wavelength, diffraction bands arise and the light asymmetrically penetrates into the area of geometric shadow. The latter effect was described in [7] as the rotation of a light beam around the z-axis. Optical vortices are not
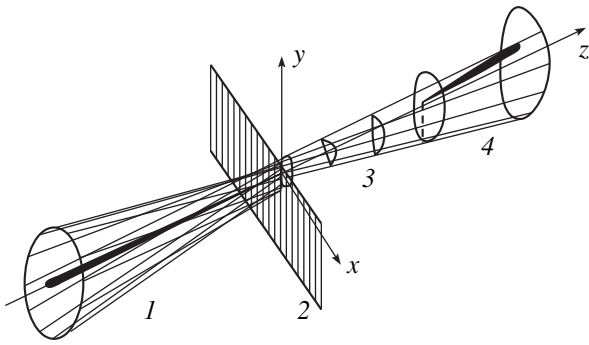
Fig. 2. Optical scheme of experiments: (*1*) optical axial vortex (the LG_0^1 mode), (*2*) opaque screen cutting off the center of the vortex, (*3*) diffraction in the near-field zone containing no singularities, and (*4*) vortex reconstruction in the far-field zone. The dashed line shows the phase step of the vortex front preceding vortex formation.

observed in the field of view in this case. Within the interval from one to two Rayleigh lengths, we observe the formation of a phase step, which subsequently gives rise to a unit OV with the same sign as the initial beam. For $z = 5L_R$, the interference fringe is split, which indicates the appearance of an OV. Note that, in contrast to intermediate states, the final result, i.e., the reconstruction of a unit vortex in the far-field zone, is independent of the degree of beam screening.

The regeneration of an optical vortex from some part of the initial beam was experimentally implemented in the optical scheme shown in Fig. 2. A beam of a He–Ne laser ($\lambda = 633$ nm) was directed to a synthesized diffraction grating, and a beam with an axial OV was produced in the first order of diffraction [8].

The beam thus produced was focused by a lens with a focal length of 50 cm. The beam waist diameter was equal to $r_0 \approx 0.25$ mm. An opaque screen cutting off some part of the beam at the level $y_0 \approx \frac{1}{4} r_0$ was placed
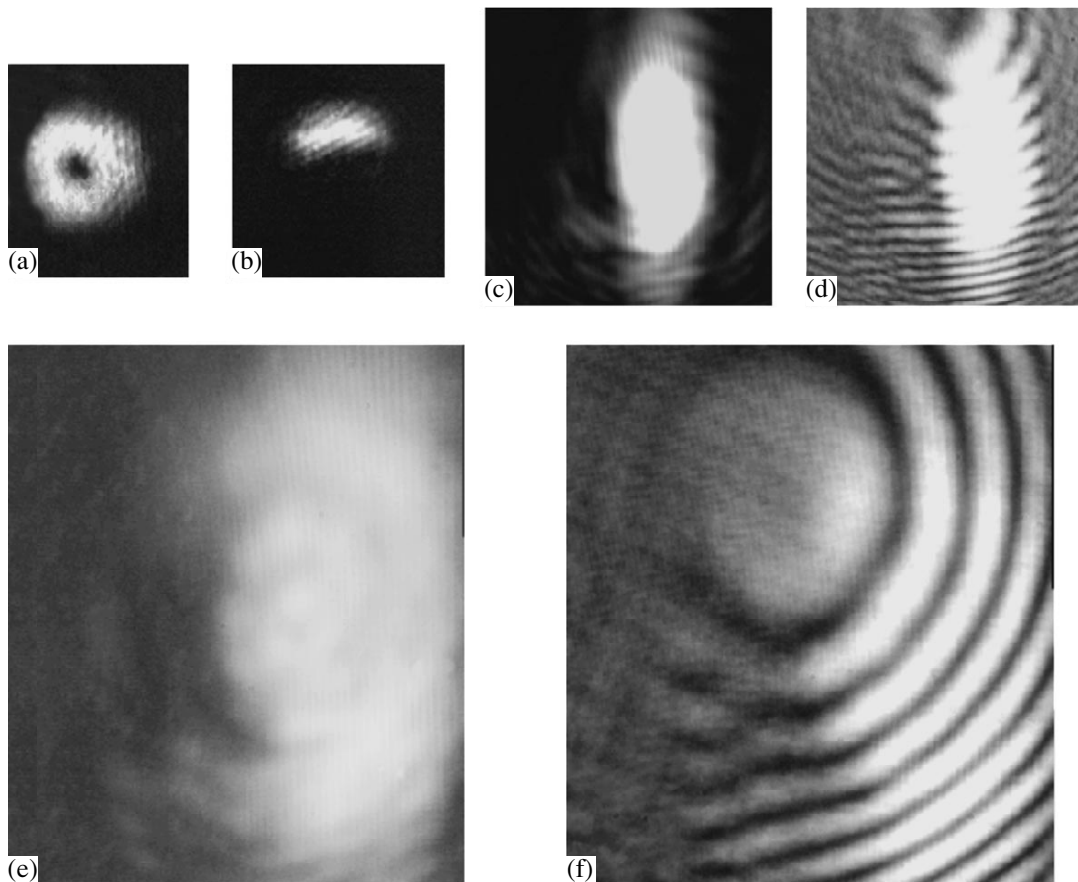
Fig. 3. Intensity distribution in the axial unit OV at different distances behind a diaphragming screen cutting off the dashed part of the beam: (a) intensity distribution in the plane of an opaque screen, (b) the part of OV behind the screen containing no zero point of field amplitude, (c) intensity distribution at $z = L_R$, (d) the corresponding pattern of interference with a plane wave, and (e, f) intensity distribution and interference pattern in the far-field zone.

in the plane of the beam waist. The degree of beam screening was visualized with the use of an auxiliary lens, which imaged the edge of the screen.

Intensity distributions in the light beam and the pattern of interference of the beam with a reference plane wave exactly coincided with the results of simulations. Figure 3 shows the results of experiments obtained in the near- and far-field zones. Interference analysis reveals a fork to the left of the bright spot, which indicates the appearance of an OV.

Thus, the results of our study demonstrate the reconstruction of an optical vortex, i.e., an optical beam with a helicoidal wave front, from some part of this beam that does not contain the vortex axis. In our opinion, this effect can be accounted for by the redistribution of the orbital angular momentum in the cross section of the beam propagating behind the screen. The existence of a residual orbital angular momentum leads to the formation of an OV carrying this momentum. The shift of the OV center with respect to the beam axis is due to the presence of a dislocation-free component [9].

REFERENCES

1. Yu. A. Anan'ev, *Optical Cavities and the Divergence of Laser Radiation* (Nauka, Moscow, 1979).
2. A. Boivin, J. Dow, and E. Wolf, J. Opt. Soc. Am. **57**, 1171 (1967).
3. J. F. Nye and M. V. Berry, Proc. R. Soc. London A **336**, 165 (1973).
4. *Optical Vortices*, Ed. by M. Vasnetsov and K. Staliunas (Nova Science, New York, 1999).
5. L. Allen, M. W. Beijersbergen, R. J. Spreeuw, and J. P. Woerdman, Phys. Rev. A **45**, 8185 (1992).
6. H. He, M. E. J. Friese, N. R. Heckenberg, *et al.*, Phys. Rev. Lett. **75**, 826 (1995).
7. M. V. Vasnetsov, I. V. Basistiy, L. V. Kreminskaya, *et al.*, Proc. SPIE **3487**, 34 (1998).
8. V. Yu. Bazhenov, M. V. Vasnetsov, and M. S. Soskin, Pis'ma Zh. Éksp. Teor. Fiz. **52**, 1037 (1990) [JETP Lett. **52**, 429 (1990)].
9. M. S. Soskin, V. N. Gorshkov, M. V. Vasnetsov, *et al.*, Phys. Rev. A **56**, 4064 (1997).

Translated by A. Zheltikov

CONDENSED MATTER

Lowering of Magnetic Field Intensity at the Surfaces of α-Fe₂O₃ and FeBO₃ Single Crystals

A. S. Kamzin[1], B. Stahl[2], R. Gellert[1], M. Muller[2], E. Kankeleit[1], and D. B. Vcherashnii[3]

[1] *Institute of Nuclear Physics, Technical University, Darmstadt, 64289 Germany*

[2] *Materials Science Department, Technical University, Darmstadt, 64287 Germany*

[3] *Ioffe Physicotechnical Institute, Russian Academy of Sciences, Politekhnicheskaya ul. 26, St. Petersburg, 194021 Russia*

Received December 28, 1999

Abstract—Depth-selective conversion electron Mössbauer spectroscopy was used to study magnetic properties of the thin surface layers of the α-Fe₂O₃ and FeBO₃ single crystals. An analysis of the experimental spectra indicates that the magnetic properties of the layers at a depth of more than ~100 nm from the surface are similar to the properties of crystal bulk, and the corresponding spectra consist of narrow lines. The lines gradually broaden as the crystal surface is approached. The spectra of the ~10-nm-thick surface layers consist of broad lines, indicating a wide distribution $\delta = 2.1$ T of the effective magnetic field about its mean value of 32.2(4) T. The experimental spectra were used to determine the effective magnetic fields (H_{eff}) for the iron ions situated in the surface layers of thickness ~100 nm. The effective fields in these layers were found to gradually decrease at room temperature (291 K) as the crystal surface was approached. The H_{eff} values in the 2.4(9)-nm-thick surface layer of the α-Fe₂O₃ crystal and 4.9(9)-nm layer of FeBO₃ are 0.7(2) and 1.2(3)%, respectively, smaller than for the nuclei of the ions in the bulk of these crystals. © 2000 MAIK "Nauka/Interperiodica".

PACS numbers: 75.70.Ak; 76.80.+y

The elaboration of theoretical methods for the description of surface magnetism and the development of new experimental methods for studying the properties of thin surface layers have stimulated much work devoted to the study of surface magnetic properties.

The ground-state magnetic moment ($T = 0$ K), the magnetic moment at nonzero temperatures, and its temperature dependence are among the most important parameters of the theory of surface magnetism. Theoretical calculations suggest that the zero-temperature mean magnetic moment increases, compared to its bulk value at a depth of four monolayers beneath the surface, by 20% in the surface layer of Ni (001) and by 34% for Fe (001) [1].

Mössbauer spectroscopy is widely used in studying the bulk and surface magnetic properties on the microscopic or local level, because the measured H_{eff} value is directly related to the local moment and is determined without applying an external magnetic field, independently of the orientation of the local spin moment. In [2, 3], Mössbauer spectroscopy was used for measuring the effective magnetic field as a function of the layer depth. The measurements were made for the films consisting of a certain number of layers of Fe⁵⁶ atoms and a layer of Fe⁵⁷ deposited at a distance of d from the surface. It was found for a series of films with $0 < d < d_n$, where n is the number of layers in the sample [3, 4], that the effective magnetic field increased as the surface

was approached at $T = 0$ K and decreased at room temperature. The depth-selective conversion electron Mössbauer spectroscopy (DSCEMS) studies of a thin film of α-Fe₂O₃ also suggested that at room temperature the H_{eff} value in a thin surface layer is 2% smaller than in the bulk of the sample [3]. It was experimentally found in [4] that the surface effective field at $T = 4.2$ K is weaker than in the bulk. On the assumption that $H_{\text{eff}}(T)$ and $M_s(T)$ are proportional to each other both in the bulk and at the sample surface, the results [4] are similar to the conclusions of the theory presented in [5]. However, the experimental data for other materials show much worse agreement with the theory.

Measurements of the spin dependence for the polarized electrons scattered from the Fe (110) surface have shown that the magnetic moment at the sample surface is 30% larger than in its bulk [6]. This is a somewhat unexpected result, because the measurements in [4] were carried out at room temperature, when the surface magnetization is expected to be reduced owing to the surface spin waves.

Thus, the influence of a surface on the magnetic properties of a surface layer calls for further investigation. This should be done with the use of experimental methods that allow the surface data to be directly compared with the bulk data. In addition, almost all studies of the surface properties were carried out for metallic
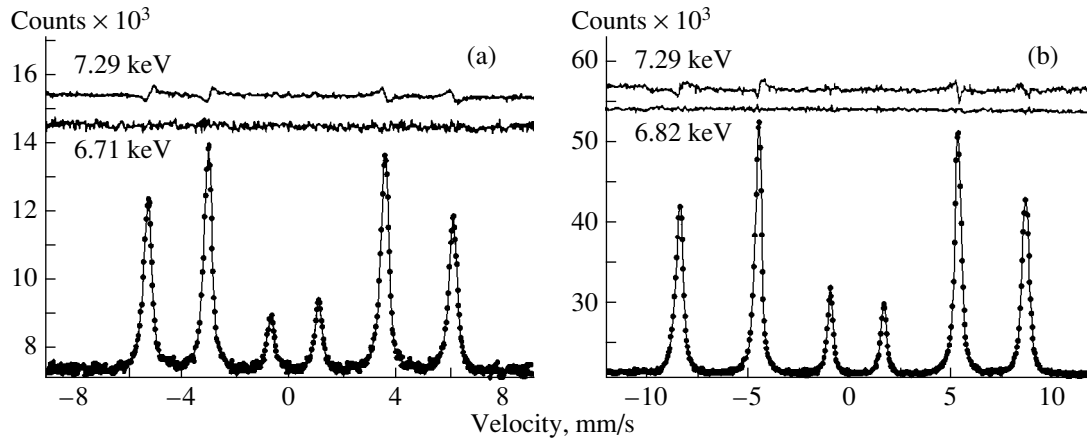
Fig. 1. Mössbauer spectra recorded for the (a) $FeBO_3$ and (b) α-Fe_2O_3 single crystals at temperature 291 K by detecting electrons at energies 6.71 and 6.82 keV, respectively. The wave vector of gamma quanta is parallel to the crystallographic C-axis. The experimental and theoretical spectra are shown by dots and lines, respectively. Above the spectra are shown the curves corresponding to the difference between the spectra recorded for the crystal bulk and by detecting electrons with energies of 7.29 and 6.71 keV for α-Fe_2O_3 and 7.29 and 6.82 keV for $FeBO_3$.

films whose surfaces may be easily oxidized, thereby introducing errors in the experimental results.

This work presents the results of experimental investigations of the effective magnetic field as a function of the layer depth from the surfaces of the α-Fe_2O_3 and $FeBO_3$ crystals. Below the Neél temperature (~961 K for α-Fe_2O_3 and ~348 K for $FeBO_3$), these compounds are antiferromagnets with weak ferromagnetic moments. The layer-by-layer studies of the surface layers were carried out by the DSCEMS method first suggested and developed in [7]. This method is based on the recording of Mössbauer spectra by detecting electrons ejected from the crystal in a narrow energy interval. To accomplish energy selection for electrons, a high-resolution magnetostatic electron analyzer was designed and constructed with a transmission capacity of 21% of 4π and energy resolution of 0.2–2%, depending on the sample size [8, 9]. The use of calibration samples in the form of films composed of the deposited Fe^{56}–Fe^{57}–Fe^{56} layers has shown that the resolution of such spectrometers is equal to 5–10 Å from the sample surface [3]. The thickness of a layer under study and its depth were calculated by the Monte Carlo method [9, 10].

The α-Fe_2O_3 and $FeBO_3$ antiferromagnets with weak ferromagnetic moments were chosen for the studies, because the iron ions occupy a single crystallographic position in these crystals, so that their room-temperature Mössbauer spectra consist of a single well-resolved Zeeman sextet. In addition, the bulk properties of these crystals are well known [11], allowing the results of our bulk experiments to be compared with the published data.

The α-Fe_2O_3 and $FeBO_3$ single crystals were synthesized from solutions in melts. The Fe^{57} isotope content in the compounds was 100%. Slabs ~5 mm in

diameter were selected from single crystals. X-ray measurements suggested that the crystallographic C-axis was perpendicular to the slab planes. When preparing the crystals, particular attention was given to the quality of the surfaces under study. Preliminary experiments have shown [12] that high-quality surface can be obtained by chemical polishing in orthophosphoric acid at a temperature of 90°C for 1 min.

The DSCEMS method was used to obtain experimental spectra of α-Fe_2O_3 and $FeBO_3$ in the energy range from 6.6 to 7.8 keV at room temperature. The gamma-ray beam was parallel to the crystallographic C-axis. Figure 1 shows the experimental spectra (dots) of $FeBO_3$ and α-Fe_2O_3 recorded for electrons with energies 6.71 and 6.82 keV. The results of mathematical processing of these spectra in the form of theoretical spectra and as difference curves are also shown in Fig. 1. One can see from the difference curve marked 6.71 keV in Fig. 1a that the $FeBO_3$ spectrum recorded for electrons with energy 6.71 keV is nicely described by the bulk parameters of the sample. The use of the same parameters for the mathematical description of the spectrum obtained for the electron energy of 7.29 keV brings about a sizable divergence between the theoretical and experimental spectra. This is clearly seen from the 7.29-keV difference curve obtained for $FeBO_3$ (Fig. 1a). A similar situation occurs for α-Fe_2O_3, as is seen from the difference curves in Fig. 1b.

The following new experimental fact is noteworthy. The spectra in Fig. 1 show noticeable asymmetry in the intensities of the outer and inner line pairs corresponding to the $\Delta m = 1$ transitions. An analysis of the causes for this effect has led to the following conclusion. The electric field gradient in the crystals of interest is aligned with the crystallographic C-axis, whereas the effective magnetic field is perpendicular to the C-axis.
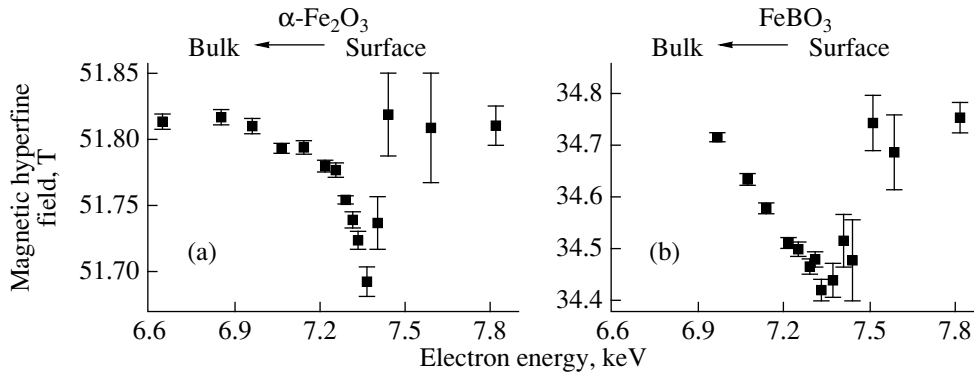
Fig. 2. Effective magnetic fields in (a) α-Fe_2O_3 and (b) $FeBO_3$ as functions of electron energy. The energy change from 6.71 to 7.29 keV corresponds to the change in the layer depth from 100 to 2.4(9) nm in α-Fe_2O_3 and from 100 to 4.9(9) nm in $FeBO_3$.

We assume [13] that, because of the interaction between these hyperfine fields, the absorption line intensities depend on the angle between them. The orthogonal orientation results in the asymmetry of the resonance lines, although the total intensity is retained.

The intensity ratio calculated from the experimental spectra for the lines of the Zeeman sextet was found to be 3 : 4 : 1. This provides additional support for the X-ray structural data indicating that the magnetic moments of the Fe atoms are oriented parallel to the crystal surface and perpendicular to the crystallographic C-axis. The effective magnetic fields calculated from the experimental spectra of electrons with energies ranging from 6.6 to 7.8 keV are presented in Fig. 2 as functions of the electron energy.

To explain the dependences obtained for the effective fields (Fig. 2), the electron yields were analyzed. It was found that the electrons with energies lower than 6.9 keV were ejected from a depth of more than 100 nm from the surface, whereas electrons with energy of 7.25 keV carry information from a 2- to 4-nm-thick surface layer. The Mössbauer spectra in the energy range from 6.9 to 7.25 keV carry information from the near-surface layers lying at a depth from 100 to ~2 nm. An analysis also showed that the electrons with energies ranging from 7.3 keV and higher relate to the L electrons that lose most of their energy because they are ejected from the surface layers lying at a depth deeper than 100 nm. This explains the shape of Mössbauer spectra recorded in this range, namely, the fact that the line widths are considerably larger than in the spectra obtained for the electrons with energies from 6.9 to 7.21 keV. Because of this, the accuracy of determining the effective magnetic fields from the data for electrons with energies higher than 7.3 keV also decreases (Fig. 2).

One can see from Fig. 2 that the effective magnetic fields at the nuclei of iron ions situated at a depth of more than 100 nm from the crystal surface (in Fig. 2, this corresponds to the electron energies of 6.9 keV and lower) are equal to 51.83 T for α-Fe_2O_3 and 34.72 T for

$FeBO_3$. These values coincide with the ones obtained in studying the bulk properties of the crystals [11, 12]. As is seen from Fig. 2, the effective magnetic fields decrease with increasing electron energy (i.e., on approaching the crystal surface). For the electron energy of 7.21 keV, the effective fields are equal to 51.69 T for α-Fe_2O_3 and 34.42 T for $FeBO_3$. Thus, the effective fields in the α-Fe_2O_3 crystal at the ion nuclei located in a surface layer of thickness 2.4(9) nm are 0.14 T lower than their bulk values. With $FeBO_3$, the effective fields decrease by 0.3 T upon approaching a surface layer of thickness 4.9 nm. In percentage terms, the effective fields in the surface layers decrease by 0.7(2)% for α-Fe_2O_3 and 1.2(3)% for $FeBO_3$. The difference in the extents of decrease of the effective fields in these crystals can be explained by the fact that the measurements were carried out at $T = 291$ K. This corresponds to the reduced temperatures ((T/T_N)) of 0.30 for α-Fe_2O_3 and 0.84 for $FeBO_3$. It is conceivable that the effective magnetic fields at the surface of the α-Fe_2O_3 crystals are less subject to thermal perturbations because the experiments for α-Fe_2O_3 were carried out at temperatures well below its Néel point.

The Mössbauer spectra recorded for the crystals of interest using conversion electron Mössbauer spectroscopy (CEMS) provide further support for the above-mentioned finding. In this case, both the conversion and the Auger electrons ejected from the sample are detected, thus providing information on the state of a surface layer of thickness ca. 300 nm. The experimental spectra recorded using the CEMS method for the surfaces of the α-Fe_2O_3 and $FeBO_3$ crystals can be most satisfactorily described mathematically with the use of a set of spectra corresponding to the effective fields graphically presented in Fig. 2.

Thus, it is experimentally demonstrated in this work that the effective magnetic field (or magnetization) gradually decreases within a surface layer of thickness ~100 nm as the crystal surface is approached.

ACKNOWLEDGMENTS

REFERENCES

1. A. J. Freeman, J. Magn. Magn. Mater. **35**, 31 (1983); S. Ohnishi, A. J. Freeman, and M. Wienert, J. Magn. Magn. Mater. **31**–**34**, 889 (1983).
2. A. H. Owens, C. L. Chien, and J. C. Walker, J. Phys. (France) **40** (C2), 74 (1978); G. Bayreuter, J. Vac. Sci. Technol. A **1**, 19 (1983).
3. T. Yang, A. Krishnan, N. Banczer-Koller, and G. Bayreuther, Phys. Rev. Lett. **48**, 1292 (1982); T. Yang, J. Trooster, T. Kachnovski, and R. Benczer-Koller, Hyperfine Interact. **10**, 795 (1981).
4. A. J. Tyson, H. Owens, and J. C. Walker, J. Magn. Magn. Mater. **35**, 126 (1983); A. J. Tyson, H. Owens, J. C. Walker, and G. Bayreuter, J. Appl. Phys. **52**, 2487 (1981).
5. D. L. Mills and A. A. Maradudin, J. Phys. Chem. Solids **28**, 1855 (1967).
6. U. Gradmann, J. Walker, R. Feder, and E. Tamura, J. Magn. Magn. Mater. **31**–**34**, 1 (1983).
7. E. Moll and E. Kankeleit, Nukleonik **7**, 180 (1965).
8. B. Stahl and E. Kankeleit, Nucl. Instrum. Methods Phys. Res. B **122**, 149 (1997).
9. B. Stahl, R. Gellert, O. Geiss, *et al.*, GSI-Rep. **180** (1994); R. Gellert, O. Geiss, G. Klingelhofer, *et al.*, Nucl. Instrum. Methods Phys. Res. B **76**, 381 (1993).
10. D. Liljequist, T. Ekdahl, and L. Baverstam, Nucl. Instrum. Methods **155**, 5292 (1978).
11. M. Eibschutz and M. E. Lines, Phys. Rev. B **7**, 4907 (1973).
12. A. S. Kamzin and L. A. Grigor'ev, Fiz. Tverd. Tela (St. Petersburg) **36**, 1271 (1994) [Phys. Solid State **36**, 694 (1994)]; Zh. Éksp. Teor. Fiz. **104**, 3489 (1993) [JETP **77**, 658 (1993)].
13. E. Kankeleit (in press).

Translated by V. Sakun

Multicritical Behavior of the Phase Diagrams
of Ferromagnet/Superconductor Layered Structures

Yu. A. Izyumov*, Yu. N. Proshin**, and M. G. Khusainov***

* Institute of Metal Physics, Ural Division, Russian Academy of Sciences,
ul. S. Kovalevskoĭ 18, Yekaterinburg, 620219 Russia

** Kazan State University, ul. Lenina 18, Kazan, 420008 Tatarstan, Russia
e-mail: yurii.proshin@ksu.ru

*** Kazan State Technical University, Vostok Branch, Chistopol', 422950 Tatarstan, Russia
e-mail: mkhusainov@vector.ru

Received January 10, 2000

Abstract—For ferromagnet/superconductor (F/S) layered structures, new 3D Larkin–Ovchinnikov–Fulde–Ferrell (LOFF) states are predicted. In most cases, these states are characterized by a higher critical temperature T_c than the known 1D LOFF states. It is shown that the nonmonotonic behavior of T_c is determined by the oscillations of the Cooper pair flux through the F/S boundary, which occur as a result of the 3D–1D–3D phase transitions at the Lifshits triple points. The appearance of the new 3D LOFF states and the presence of nonmagnetic impurities leads to a strong damping of the 1D oscillations of the LOFF pair amplitude and to a considerable smoothing of the dependence of T_c on the F layer thickness d_f. An interpretation of the behavior of the experimental dependences $T_c(d_f)$ obtained for F/S structures is proposed. © *2000 MAIK "Nauka/Interperiodica"*.

PACS numbers: 74.80.Dm; 75.30.Kz; 74.62.-c

The competition between the superconducting and magnetic states in ferromagnetic metal/superconductor (F/S) layered structures gives rise to a number of nontrivial phenomena, which in many cases cannot be simultaneously observed in homogeneous materials. Specifically, in some experiments on Fe/V [1] and Gd/Nb [2] systems, the dependence of T_c on the ferromagnetic layer thickness d_f exhibited a rapid initial decrease followed by a plateau, while in other experiments on these systems ([3] and [4, 5], respectively), the plateau was preceded by an oscillatory behavior of the dependence $T_c(d_f)$. The first theoretical interpretations of the nonmonotonic behavior of $T_c(d_f)$ were based on the change of type of superconductivity from the conventional 0-phase to the π-phase, with the order parameter Δ changing sign in passing through the F layers [6, 7]. However, these theories are restricted to the case of a highly transparent F/S boundary and an extremely dirty ferromagnetic metal, and they cannot provide a generalized description of the two different types of behavior observed for the dependence $T_c(d_f)$. Moreover, it was found that oscillations of $T_c(d_f)$ also occur in Fe/Nb/Fe trilayer structures [8] in which the π-phase superconductivity is impossible. Therefore, we (Proshin and Khusainov) [9–11] developed a theory for describing the proximity effect without the aforementioned limitations. We attributed the oscillations of $T_c(d_f)$ to the oscillations of the Cooper pair flux, which occur at the F/S boundary because of the one-dimensional (1D) oscillations of the pair amplitude across the

F layer; the latter oscillations, in their turn, lead to a quantum coupling between the F layer boundaries. This theory allowed us not only to find an explanation for the qualitative difference in the behavior of T_c observed in different experiments [1–5, 8], but also to predict some new effects, such as pronounced oscillations of $T_c(d_f)$ and periodically recurrent superconductivity. However, these effects have not yet been confirmed by experiments [12–15], except for the single publication [16] reporting on damped oscillations of $T_c(d_f)$ in Co/Nb and Co/V systems.

In reality, for both bilayers and multilayers of the F/S type, only one local maximum can be observed in the dependence $T_c(d_f)$. In our opinion, the reason is that the previous theories [6, 7, 9–11] are valid only for F/S structures with F layers that are quasi-one-dimensional ferromagnets in which the spatial variations of the pair amplitude along the F/S boundaries can be neglected. In real three-dimensional (3D) F/S systems, the pair correlations induced by the S layers in the F layers (to the extent allowed by the transparency of the boundaries) should be three-dimensional and be described by a 3D pair wave vector **k**, according to the Larkin–Ovchinnikov–Fulde–Ferrell (LOFF) theory [17, 18] for isotropic ferromagnetic superconductors. In fact, the large exchange splitting $2I \gg \pi T_c$ of the conduction zone changes the pairing conditions and, in the ferromagnet, pairing will occur between the quasi-particles from the isoenergetic states **p**, ↑ and −**p** + **k**, ↓ with momenta that differ in magnitude, where $k \sim 2I/v_f$ for

$2I \ll E_f$, and E_f and v_f are the Fermi velocity and energy, respectively. The scattering by nonmagnetic impurities at a rate τ_f^{-1} does not affect the BCS pairing with the zero pair momentum, and this scattering will impede the formation of the LOFF phase in the F layers. Therefore, in relatively pure ferromagnetic layers with $2I\tau_f > 1$, the pair amplitude should exhibit oscillations which have the period $a_f = v_f/2I \sim k^{-1}$ and decay within the mean free path $l_f = v_f\tau_f$ from the F/S boundary. At the same time, the wave function of Cooper pairs in the S layers has a constant sign but an arbitrary phase. Thus, in F/S systems, the superconductivity is a combination of the BKS pairing in the S layers and LOFF pairing in the F layers. The study of the mutual adjustment of these two competing types of pairings is the subject of this paper.

An adequate theoretical description of the proximity effect in F/S structures should allow for the spatial variations of the pair amplitude not only across the F and S layers, but also in the F/S boundary plane. For this purpose, it is necessary to solve a 3D boundary-value problem for the Usadel function $F(\mathbf{r}, \omega)$, rather than the 1D problem considered in the cited publications [6, 7, 9–11]. The microscopic derivation of this boundary-value problem for a planar contact between an F layer occupying the region $-d_f < z < 0$ and an S layer occupying the region $0 < z < d_s$ is similar to the corresponding derivation for the 1D function $F(z, \omega)$ (see [11]). For brevity, we omit this derivation. However, unlike the aforementioned case [11], we use the translational invariance of the system in the $x - y$ plane and formulate the boundary-value problem for a contact between dirty metals F and S in terms of a two-dimensional Fourier transform of the Usadel function $F(\mathbf{q}, z, \omega)$, where $\mathbf{q}$ is a 2D wave vector. The diffusion-type differential equations for the S and F layers have the form

$$\left[\omega + \frac{D_s}{2}\left(q_s^2 - \frac{\partial^2}{\partial z^2}\right)\right]F_s(\mathbf{q}_s, z, \omega) = \Delta_s(\mathbf{q}_s, z),$$
$$\left[\omega + iI + \frac{D_f(I)}{2}\left(q_f^2 - \frac{\partial^2}{\partial z^2}\right)\right]F_f(q_{\mathbf{f}}, z, \omega) = \Delta_f(q_f, z). \tag{1}$$

Here, $\omega = \pi T(2n + 1)$ is the Matsubara frequency ($\omega > 0$) and $D_{s(f)} = v_{s(f)}l_{s(f)}/3$ and $\Delta_{s(f)}$ are the electron diffusion coefficients and the superconducting order parameters, respectively, in S and F layers. The complex diffusion coefficient $D_f(I)$ allows for the competition between different types of the quasi-particle motion in the F layer [9–11]: the diffusion-type motion ($2I\tau_f < 1$), where $D_f(I) = D_f/(1 + i2I\tau_f)$, and the spin-wave-type one ($2I\tau_f > 1$), where $D_f(I) \approx 3D_f/(1 + i2I\tau_f)$. The two-dimensional wave vectors $q_{s(f)}$ are responsible for the spatial variations of $F(\mathbf{r}, \omega)$ in the plane of con-

tact. The boundary conditions corresponding to equations (1) at the boundary $z = 0$ have the form

$$\frac{4D_s}{\sigma_s v_s}\frac{\partial F_s(\mathbf{q}_s, z, \omega)}{\partial z}\bigg|_{z = +0} = \frac{4D_f(I)}{\sigma_f v_f}\frac{\partial F_f(\mathbf{q}_f, z, \omega)}{\partial z}\bigg|_{z = -0} \tag{2}$$
$$= F_s(\mathbf{q}_s, +0, \omega) - F_f(\mathbf{q}_f, -0, \omega).$$

These conditions relate the pair amplitude flux to the pair amplitude drop at the F/S boundary. In expression (2), $\sigma_{s(f)}$ are the boundary transmissivities from the side of the S and F metals; these quantities satisfy the detailed balance relation $\sigma_s v_s N_s = \sigma_f v_f N_f$ [9–11], where N_s and N_f are the densities of states. The boundary-value problem (1), (2) obtained for the proximity effect in the F/S contact differs from the previously considered problems [6, 7] in three aspects. First, the boundary conditions used in [6, 7], $F_s(+0, \omega) = F_f(-0, \omega)$, are a particular case of equations (2) and correspond to the high transmissivity limit $\sigma_{s(f)} \longrightarrow \infty$, i.e., to the neglect of the $F(\mathbf{r}, \omega)$ flux through the F/S boundary. Second, in the ferromagnet, the quasi-particle motion is of a mixed diffusion-wave nature and is described by an effective complex diffusion coefficient $D_f(I)$ instead of the real one D_f used in [6, 7]. Third, the system of equations (1), (2) allows not only 1D solutions for the pair amplitude $F(\mathbf{r}, \omega)$, but also 3D ones, unlike all other problems considered earlier [6, 7, 9–11]. Below, we will show that it is precisely the competition between the previously known 1D and new 3D LOFF states that radically changes the dependence $T_c(d_f)$ from that obtained in the previous theories [6, 7, 9–11].

To calculate the dependences of the critical temperature T_c of an F/S contact on the transmissivity of the F/S boundary, the layer thickness, the parameter $2I\tau_f$, etc, we solve the system of equations (1), (2) in combination with the Gor'kov self-consistent equations (see [9–11])

$$\Delta_s(\mathbf{q}_s, z) = 2\lambda_s\pi T\mathrm{Re}\sum_{\omega > 0}' F_s(\mathbf{q}_s, z, \omega),$$
$$\Delta_f(\mathbf{q}_f, z) = 2\lambda_f\pi T\mathrm{Re}\sum_{\omega > 0}' F_f(\mathbf{q}_f, z, \omega), \tag{3}$$

where $\lambda_{s(f)}$ are the electron–electron interaction constants in the S and F layers.

We seek the solutions to equations (1)–(3) in the form that excludes the electron flux through the outer boundaries of the F/S contact: $F_s(\mathbf{q}_s, z, \omega) \propto \cos k_s(z - d_s)$, $F_f(\mathbf{q}_f, z, \omega) \propto \cos k_f(z + d_f)$. Here, $k_{s(f)}$ are the wave vector components that are independent of frequency ω ($\omega \ll I$) and describe the spatial variations of the pair amplitude $F(\mathbf{r}, \omega)$ across the layers (along the z-axis). As a result, for the reduced superconducting transition temperature of the F/S contact $t = T_c/T_{cs}$, we obtain an

equation similar to that obtained by Abrikosov and Gor'kov:

$$\ln t = \Psi\!\left(\frac{1}{2}\right) - \operatorname{Re}\Psi\!\left(\frac{1}{2} + D_s\frac{k_s^2 + q_s^2}{4\pi T_{cs}t}\right), \qquad (4)$$

where T_{cs} is the critical temperature of an isolated S layer, $\Psi(x)$ is the digamma function, and the pair-breaking parameter $D_s k_s^2$ is a solution to another transcendental equation

$$D_s k_s \tan k_s d_s = \frac{\sigma_s v_s}{4 - (\sigma_f v_f/D_f(I)k_f)\cot k_f d_f}. \qquad (5)$$

For $2I\tau_f < 1$ and $I \gg \pi T_{cs}$, the wave number k_f involved in equation (5) is determined by the expression

$$k_f^2 + q_f^2 = -\frac{2iI}{D_f(I)} = -\frac{2iI(1 + 2iI\tau_f)}{D_f}. \qquad (6)$$

From the condition of minimum free energy (maximum T_c), it follows that q_s is exactly equal to zero. This is no surprise, since in the case of the BCS pairing with the zero pair momentum, the pair amplitude $F_s(\mathbf{r}, \omega)$ should have a constant sign in the S layer. In the F layer, the LOFF pairing takes place with a nonzero three-dimensional coherent pair momentum $\mathbf{k} = (\mathbf{q}_f, k_f)$ and an oscillating pair amplitude $F_f(\mathbf{r}, \omega)$. From equations (4)–(6), it follows that the value of the 2D wave vector q_f remains arbitrary and should be determined by way of optimization, i.e., from the condition of maximum T_c.

From boundary conditions (2), it follows that the left-hand member of equality (5), which determines the pair-breaking parameter $D_s k_s^2$ in equation (4) for T_c, is proportional to the Cooper pair flux from the S layer to the F layer. The resonance denominator of the right-hand member of equality (5) is inversely proportional to the pair amplitude drop at the F/S boundary and determines the periodic variations of the aforementioned pair flux with increasing F layer thickness owing to the function $\cot k_f d_f$. However, in contrast to the previously obtained 1D solutions with $q_f = 0$ [9–11], the presence of new 3D solutions with real $q_f \neq 0$ considerably reduces $\operatorname{Re} k_f$ according to equation (6). This leads to an increase in the period of the pair amplitude $F_f(\mathbf{r}, \omega)$ oscillations along the z-axis. As this period becomes greater than the depth of pair penetration in the F layer ($\operatorname{Im} k_f > \operatorname{Re} k_f$), the coherent coupling of the two boundaries of the F layer is disrupted. As a result, the observation of the oscillations of $T_c(d_f)$ becomes difficult (except perhaps for the first peak).

The other mechanism that works in parallel with the mechanism described above and produces a similar effect, i.e., the disruption of the quantum coupling between the two boundaries of the F layer and a noticeable suppression of the oscillations of $T_c(d_f)$, is related

to the presence of nonmagnetic impurities [9–11]. As the concentration of the latter increases, the quasi-particle motion in the F layer will change from the wave-type motion characteristic of pure ferromagnets with $2I\tau_f > 1$ to a diffusion-type motion corresponding to $2I\tau_f < 1$. The transverse pair momentum k_f will become a poor quantum number, and the oscillations of the LOFF pair amplitude will be strongly damped ($\operatorname{Im} k_f > \operatorname{Re} k_f$). As a result, they will no longer provide coherent coupling between the boundaries of the F layer. Recall that, in the case of a pure F layer with $2I\tau_f > 1$, the substitution $D_f \longrightarrow 3D_f$ should be performed in formulas (5) and (6) (see [11]).

The results of the numerical analysis of the dependences $T_c(d_f)$ are shown in Figs. 1a–1f for different values of the parameters σ_s, $2I\tau_f$, $n_{sf} = N_s v_s/N_f v_f$, l_s, and d_s. In Fig. 1a, the thick solid line shows the behavior of $T_c(d_f)$ optimized with allowance for the competition between the 1D and 3D LOFF states. The periodically recurrent superconductivity, which was predicted earlier in the framework of the 1D theory [9–11], is shown by thin dashed lines and is completely spanned by the almost monotonically decreasing dependence $T_c(d_f)$. The only small rise in $T_c(d_f)$, as in the experiment [8] on Fe/Nb/Fe trilayers, is caused by a series of 3D–1D–3D alternating phase transitions. At the top of Fig. 1a, we present the magnitude of the two-dimensional wave vector q_f versus d_f. The region corresponding to the 1D LOFF phase ($q_f = 0$) is marked by shading, and the remaining part of the plot corresponds to the 3D LOFF phase ($q_f > 0$). The specific feature of the presented phase diagram $T_c(d_f)$ is that it contains Lifshits triple points (the intersections of the solid and dashed lines) at which three phases come together: two superconducting phases (the 1D commensurate phase with $q_f = 0$ and the 3D incommensurate one with $q_f \neq 0$) and one normal phase.

Figures 1b–1f present the dependences $T_c(d_f)$ optimized with respect to the quantity q_f with allowance for the competition between the 1D and 3D LOFF states. The dependences were obtained for different values of all main parameters of the theory. In each of the five figures, one can see all qualitatively different versions of the behavior of $T_c(d_f)$: from the monotonic decrease down to zero, which was taken as the initial version and was observed in many experiments [3, 13], to the recurrent superconductivity and a subsequent flattening, both through a single small rise [8] and without any nonmonotonic features [2]. We note that the regions corresponding to the recurrent superconductivity, which was predicted earlier [9–11] for the 1D case, are bounded in the 3D case by quite a narrow range of parameter values. This explains why the aforementioned phenomenon has not yet been observed experimentally in real F/S systems.

The derivation of the equations for T_c of an F/S superlattice formed by alternating F and S layers with
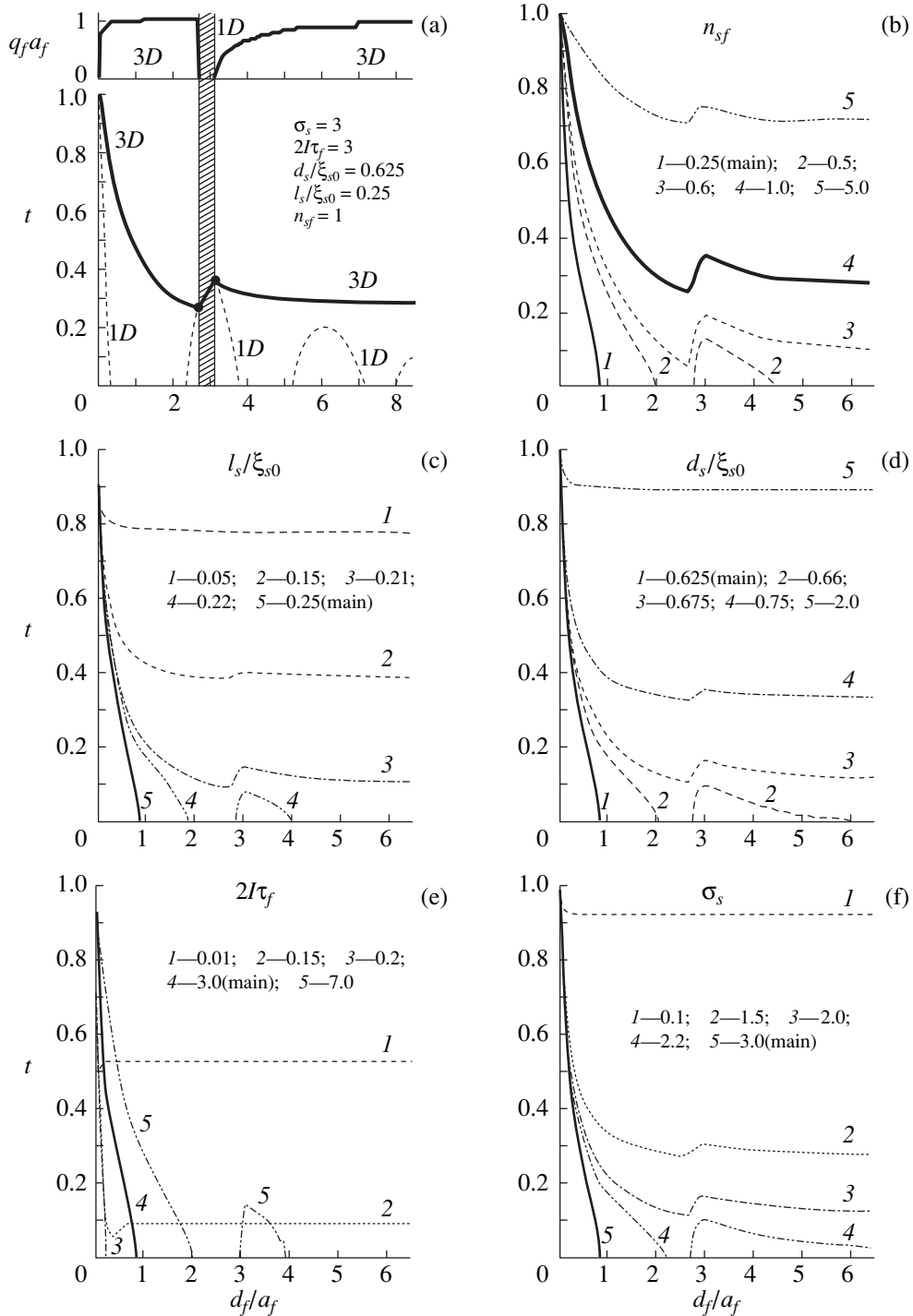
Fig. 1. Dependence of the reduced critical temperature of an F/S contact on the reduced F layer thickness for different values of five main parameters of the theory. (a) Optimized solutions $t(d_f/a_f)$ and $q_f a_f(d_f/a_f)$ are represented by thick solid lines; thin dashed lines correspond to proper 1D solutions; full circles show the Lifshits triple points; ξ_{s0} is the BCS coherence length. (b)–(f) Only one parameter indicated at the top is varied, while other parameters remain fixed; the main curve is the dependence corresponding to $2I\tau_f = 3$, $\sigma_s = 3$, $l_s/\xi_{s0} = 0.25$, $d_s/\xi_{s0} = 0.625$, and $n_{sf} = 0.25$. The optimized curve in Fig. 1a corresponds to curve 4 in Fig. 1b.

the thicknesses d_f and d_s, respectively, is similar to the corresponding derivation described in our previous paper (see [11]). However, we note that, in contrast to the F/S contacts, two stable LOFF states are possible

for a unit cell of an F/S superlattice. The difference between these states lies in the type of symmetry of the pair amplitude with respect to the center of the F layer: for the 0-phase state, we have $F_f(\mathbf{q}_f, z, \omega) \propto \cos k_f(z + d_f/2)$;
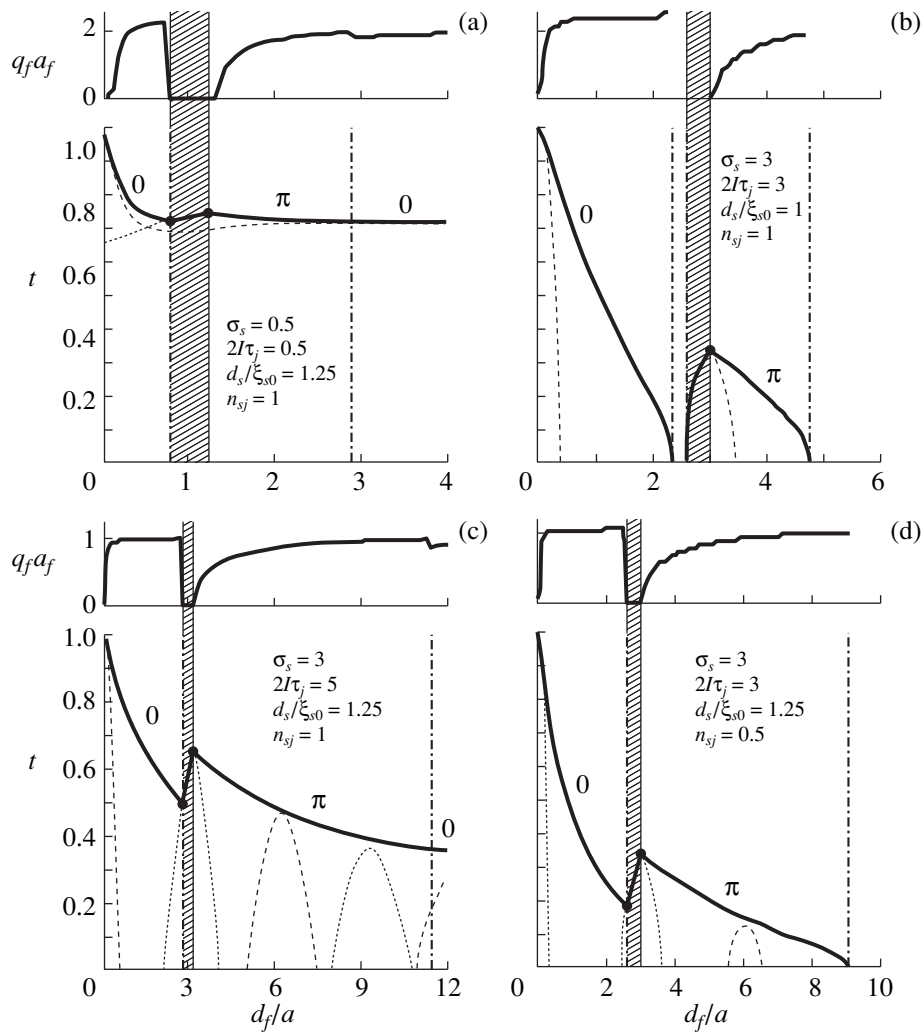
Fig. 2. Phase diagrams of F/S superlattices at $l_s/\xi_{s0} = 0.25$ for different values of the parameters of the theory. The main notations are the same as in Fig. 1a. Thin dashed lines represent the proper 1D 0-phase solutions, and the dotted lines correspond to the 1D π-phase ones. The regions of the realization of optimized 0- and π-phase states are separated by vertical dash-and-dot lines.

and for the π-phase state, we have $F_f(\mathbf{q}_f, z, \omega) \propto \sin k_f(z + d_f/2)$. For the 0-phase case, the equations for T_c are obtained from formulas (4)–(6), with d_i being replaced by $d_i/2$. To determine T_c in the π-phase case, the same procedure should be used with the additional substitution of the function $-\tan x$ for $\cot x$ in the right-hand member of equality (5).

The phase diagrams $T_c(d_f)$ obtained for F/S superlattices are shown in Figs. 2a–2d. The 0-phase and π-phase 1D solutions obtained earlier [9–11] are represented by thin dashed and dotted lines, respectively. The thick solid lines show the results of the optimization of the dependence $T_c(d_f)$ determined by the competition between the 1D and 3D solutions for both 0-phase and π-phase LOFF states. According to Fig. 2c, at some values of the superlattice parameters, the function $T_c(d_f)$ exhibits a single small rise caused by the 3D(0)–1D(π)–3D(π) transition. Such behavior of the

critical temperature was observed experimentally for Gd/Nb multilayers [4, 5] and for Co/Nb and Co/V superlattices [16]. At lower values of σ_s and $2I\tau_f$, the rise feature is suppressed and the monotonic decrease in $T_c(d_f)$ is immediately followed by a plateau (Fig. 2a). Such behavior of $T_c(d_f)$) was observed for Fe/V [1], Gd/Nb [2], and $V_{1-x}Fe_x/V$ [13] superlattices. In addition, we predict new versions of the nonmonotonic behavior of $T_c(d_f)$ that are characteristic only of F/S superlattices: the recurrent superconductivity in the form of a single 1D–3D(π) peak (Fig. 2b) and an oscillatory decrease in T_c down to zero as a result of the 3D(0)–1D(π)–3D(π) transitions (Fig. 2d). The points of the phase transitions at which the period of the 2D modulation of the pair amplitude along the F/S boundaries becomes infinite ($q_f = 0$) correspond to the Lifshits triple points. Thus, the seemingly simple (as in Fig. 2a) behavior of $T_c(d_f)$, which was observed in many exper-

iments, may be determined by the nontrivial physics of F/S systems, namely, by the combined (BCS + LOFF) mechanism of superconductivity and by the competition between the 1D and 3D LOFF states in the F layers.

The 1D LOFF states with pronounced oscillations of $T_c(d_f)$, which are shown in Figs. 1a and 2a–2d by thin dashed lines, presumably could be realized in pure state in F/S structures, in which the F layers are quasi-one-dimensional ferromagnets with conducting filaments oriented normally to the F/S boundary. Another possibility for the realization of only 1D LOFF states consists in the replacement of the F layers by quasi-one-dimensional ferromagnetic bridges (whiskers). In these cases, the appearance of 3D states with spatial variations of the pair amplitude along the F/S boundaries can be neglected.

It is significant that, for both F/S bilayers and F/S superlattices, the appearance of new 3D LOFF states in addition to the 1D states prevents T_c from rapidly becoming zero with increasing d_f and leads to an increase in the area of the superconducting regions in the phase diagrams in Figs. 1 and 2. Moreover, the competition between the 1D and 3D states, which leads to the multicritical behavior of the phase diagrams, is the factor that is responsible for the nonmonotonic behavior of $T_c(d_f)$ at some thicknesses of the F layer and for the absence of oscillations in the case of large d_f. Our analysis shows that the difference in the dependences $T_c(d_f)$ obtained from different experiments for F/S multilayers of identical composition is presumably explained by the differences in the values of the parameters σ_s, $2I\tau_f$, l_s, and d_s, i.e., in the transparency of the F/S boundaries and the purity of the F and S layers. In their turn, these differences may be caused the variations in the methods and conditions of the sample preparation.

ACKNOWLEDGMENTS

REFERENCES

1. P. Koorevaar, Y. Suzuki, R. Coehoorn, *et al.*, Phys. Rev. B **49**, 441 (1994).

2. C. Strunk, C. Sürgers, U. Paschen, *et al.*, Phys. Rev. B **49**, 4053 (1994).

3. H. K. Wong, B. Y. Jin, H. Q. Yang, *et al.*, J. Low Temp. Phys. **63**, 307 (1986).

4. J. S. Jiang, D. Davidović, D. H. Reich, *et al.*, Phys. Rev. Lett. **74**, 314 (1995).

5. J. S. Jiang, D. Davidović, D. H. Reich, *et al.*, Phys. Rev. B **54**, 6119 (1996).

6. Z. Radović, M. Ledvij, L. Dobrosavljević-Grujić, *et al.*, Phys. Rev. B **44**, 759 (1991).

7. A. I. Buzdin, B. Bujicić, and M. Yu. Kupriyanov, Zh. Éksp. Teor. Fiz. **101**, 231 (1992) [Sov. Phys. JETP **74**, 124 (1992)].

8. Th. Mühge, N. N. Garif'yanov, Yu. V. Goryunov, *et al.*, Phys. Rev. Lett. **77**, 1857 (1996).

9. Yu. N. Proshin and M. G. Khusainov, Pis'ma Zh. Éksp. Teor. Fiz. **66**, 527 (1997) [JETP Lett. **66**, 562 (1997)].

10. M. G. Khusainov and Yu. N. Proshin, Phys. Rev. B **56**, 14283 (1997).

11. Yu. N. Proshin and M. G. Khusainov, Zh. Éksp. Teor. Fiz. **113**, 1708 (1998) [JETP **86**, 930 (1998)].

12. N. N. Garif'yanov, Yu. V. Goryunov, Th. Mühge, *et al.*, Eur. Phys. J. B **1**, 405 (1998).

13. J. Aarts, I. M. E. Geers, E. Brück, *et al.*, Phys. Rev. B **56**, 2779 (1997).

14. Th. Mühge, K. Theis-Bröhl, K. Westerholt, *et al.*, Phys. Rev. B **57**, 5071 (1998).

15. G. Verbank, C. D. Potter, V. Metlushko, *et al.*, Phys. Rev. B **57**, 6029 (1998).

16. Y. Obi, V. Ikebe, T. Kubo, *et al.*, Physica C **317**–**318**, 149 (1999).

17. A. I. Larkin and Yu. N. Ovchinnikov, Zh. Éksp. Teor. Fiz. **47**, 1136 (1965) [Sov. Phys. JETP **20**, 762 (1965)].

18. P. Fulde and R. A. Ferrell, Phys. Rev. A **135**, 550 (1964).

Translated by E. Golyamina

CONDENSED
MATTER

Magnetic Resonance Spectrum of a Two-Phase State in Single Crystals of La$_{0.7}$Pb$_{0.3}$MnO$_3$ Lanthanum Manganite

G. A. Petrakovskiĭ*, N. V. Volkov, V. N. Vasil'ev, and K. A. Sablina

Kirenskiĭ Institute of Physics, Siberian Division, Russian Academy of Sciences, Akademgorodok,
Krasnoyarsk, 660036 Russia
*e-mail: gap@cc.krascience.rssi.ru
Received January 10, 2000

Abstract—Two absorption lines are observed over a wide temperature range below T_c in the magnetic resonance spectrum of an La$_{0.7}$Pb$_{0.3}$MnO$_3$ single crystal. These lines correspond to two magnetic phases in the sample. The frequency–field dependence of spectra obtained in the range of microwave radiation frequencies 10–77 GHz allows these phases to be interpreted as ferromagnetic and paramagnetic phases. The phase volume ratio depends on the temperature and the magnitude of the external magnetic field. Features in the temperature behavior of parameters of the magnetic absorption line are observed in the region of the highest magnetic resistance of the sample. The results are interpreted within the mechanism of electronic phase separation. © 2000 MAIK "Nauka/Interperiodica".

PACS numbers: 76.50.+g; 72.20.My

At present, the mechanism of electronic phase separation is one of the most widely discussed mechanisms of colossal magnetic resistance in ferromagnetic manganites with the perovskite structure [1]. Direct evidence for the coexistence in the material bulk of a ferromagnetic metallic phase and a phase with localized charge carriers was obtained in experiments on studying NMR [2], optical properties [3], electron diffraction [4], and neutron scattering [5]. It is evident that such a mixed two-phase state must be manifested in an investigation by the magnetic resonance method, which is rather sensitive to the magnetic inhomogeneity of materials. Moreover, because the two-phase state in electronic separation is controlled by the external magnetic field, magnetic resonance spectra recorded at different frequencies of microwave radiation can differ significantly. The few previous investigations of magnetic resonance in lanthanum manganite materials were ambiguous, and the problem was stated differently in these works. At the same time, the results of almost all works gave evidence of the magnetic inhomogeneity of the materials under study, although these materials were homogeneous in the crystallographic respect [6, 7].

In this work, we report the results of investigating the magnetic resonance spectra of La$_{0.7}$Pb$_{0.3}$MnO$_3$ single crystals, which exhibit the effect of colossal magnetic resistance. Measurements were carried out on spectrometers with (1) the working frequency $\nu = 10$ GHz and a constant magnetic field and (2) a tunable frequency in the range $\nu = 37$–77 GHz and a pulsed magnetic field. Single crystals of La$_{0.7}$Pb$_{0.3}$MnO$_3$ were grown by spontaneous crystallization from a molten mixture [8]. The samples under study were shaped like thin plates ($4 \times 2 \times 0.1$ mm) whose plane coincided with one of the main crystal planes. The magnetic field was applied along the plane of the sample.

The main feature of the magnetic resonance spectra in the crystals under study is the occurrence of two well-resolved lines of magnetic absorption in a wide temperature range. The temperature behavior of the parameters of absorption lines for the frequency $\nu = 10$ GHz is shown in Fig. 1. We believe that the line designated in Fig. 1 as F corresponds to a resonance from the crystal domains that occur in the ferromagnetic state. Line F appears only below the Curie point $T_c \approx 360$ K; and its intensity increases with decreasing temperature, which may be associated with an increase in crystal magnetization M_0 and also with an increase in the volume of the ferromagnetic phase in the sample. A decrease in the resonance field H_r^F with decreasing temperature is associated with anisotropic interactions, that is, with a rise in magnetic crystallographic anisotropy and with sample shape anisotropy. Additional orientational investigations of the magnetic resonance in samples of spherical shape showed that the effective field of magnetic crystallographic anisotropy H_A does not exceed 100 Oe. Variations of H_r^F are mainly associated with a rise in degaussing fields, which are proportional to the magnetic moment. The following equation may be written for the geometry in which our experiment was carried out ($H_{0\parallel}$ is parallel to the sample plane):

$$\omega/\gamma = (H_0 + 4\pi M_{\text{eff}})^{1/2}, \tag{1}$$
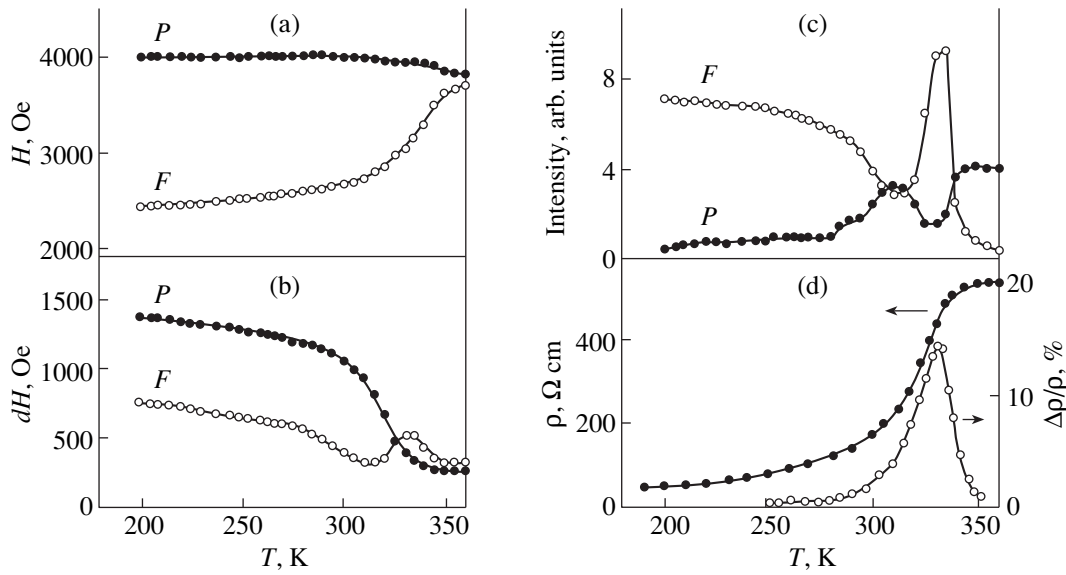
Fig. 1. Temperature dependence of the parameters of lines F and P in the magnetic resonance spectrum of an $La_{0.7}Pb_{0.3}MnO_3$ single crystal ($v = 10$ GHz): (a) resonance field, (b) line width, and (c) line intensity; (d) temperature dependence of the resistivity ρ_0 and the magnetic resistance $\Delta\rho/\rho_0$ in the field $H = 7$ kOe.

where $\omega = 2\pi v$ is the angular frequency, $\gamma = (g\mu_B/\hbar)$ is the gyromagnetic ratio, H_0 is the resonance field, and M_{eff} is the effective magnetization. In the general case, M_{eff} will differ from M_0 because of the effect of crystallographic anisotropy, which is neglected in (1), and also because of possible magnetic inhomogeneity of the crystal (which, as will be shown below, does occur). At the same time, the temperature behavior of the quantity $4\pi M_{eff}(T)$ determined from (1) qualitatively repeats the behavior of the quantity $4\pi M_0(T)$ obtained from static measurements.

Line P, which is observed in the paramagnetic state of the sample ($T > T_c$), virtually retains its position as the temperature decreases below T_c, and its resonance field H_r^P does not depend on the sample shape and the orientation of H_0 in the crystal. The insignificant increase in H_r^P in the temperature range 340–350 K may be associated with the change in the g-factor due to local distortions of the crystal lattice. Such distortions arising from strong electron–phonon coupling were revealed for a number of compositions of impurity manganese perovskites in the temperature range corresponding to the transition to the ferromagnetic state [9]. The decrease in the intensity of line P with decreasing temperature indicates that the fraction of the paramagnetic phase in the sample decreases.

A significant broadening of the ferromagnetic resonance line dH_r^F with decreasing temperature has also been observed previously by various authors in studying crystalline and film manganite samples. However, a thorough analysis of the mechanisms leading to an increase in dH_r^F has not been presented yet. From our point of view, the electrical conductivity of the samples is the main factor that affects dH_r^F. Actually, the resistivity ρ of the crystals rapidly drops below T_c (Fig. 1). This means an increase in either the mobility or the concentration of charge carriers, which, in its turn, exerts a significant effect on dynamic magnetic phenomena. The contribution of charge carriers to dissipation processes can have several mechanisms as its basis [10]. An inhomogeneous two-phase magnetic state must also exert a significant effect on dH_r^F. This state will lead to nonuniform magnetization of ferromagnetic domains and, consequently, to a broadening of the ferromagnetic resonance line.

The features in the behavior of magnetic absorption line intensities and widths at a temperature $T \sim 325$ K engage the attention. It is interesting that the maximum in the temperature dependence of $\Delta\rho/\rho$ corresponds to just the same temperature (Fig. 1).

Undoubtedly, the behavior of the frequency–field dependence for the absorption lines (Fig. 2) is an important argument in favor of the statement that the observed lines P and F correspond to resonance absorption from paramagnetic and ferromagnetic domains, respectively. An extrapolation of the experimental points in the frequency–field dependence for line P indicates that the dependence is linear and passes through the origin of the coordinates. This pattern is observed for any orientation of the external magnetic field H_0. This fact confirms that line P is associated with the domains in the crystal that occur in the paramagnetic state even below T_c. The behavior of the fre-
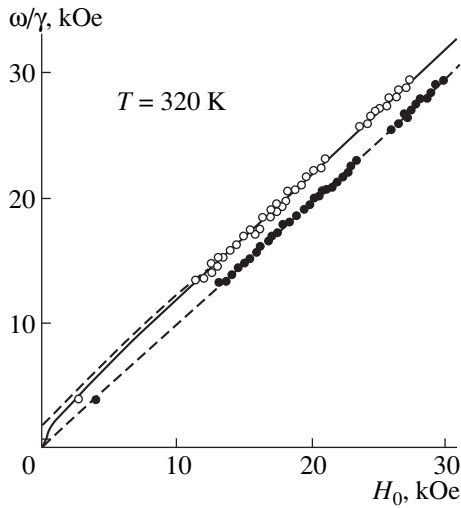
Fig. 2. Frequency–field dependence of lines *F* and *P* in the magnetic resonance spectrum of an $La_{0.7}Pb_{0.3}MnO_3$ crystal, *T* = 320 K. Solid line represents dependence (1) (see text), and dashed lines are linear extrapolations of experimental points.
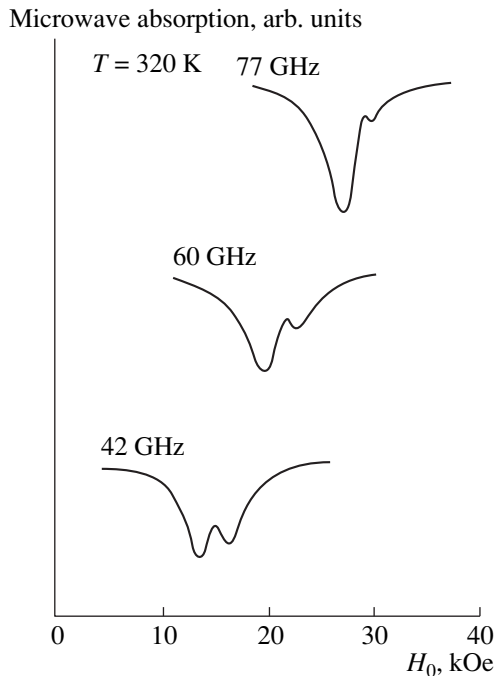
Fig. 3. Magnetic resonance absorption spectra of an $La_{0.7}Pb_{0.3}MnO_3$ crystal recorded at various microwave radiation frequencies ν (42, 60, and 77 GHz); *T* = 320 K.

quency–field dependence for line *F* is characteristic of uniform magnetic oscillations in a ferromagnetic material. The shift of the dependence with respect to the origin is determined in our case mainly by the anisotropy of the sample shape (see (1)).

The dependence of the intensities of lines *P* and *F* on the microwave radiation frequency at which the magnetic resonance spectrum has been recorded is another important experimental result in addition to the demonstration of the two-phase paramagnetic–ferromagnetic state (Fig. 3). If the frequency ν and, hence, the magnitude of the external magnetic field H_0 were increased at a fixed temperature, the intensity of line *F* increased and that of line *P* decreased. This fact can be interpreted as control of the ratio between the phase volumes by the external magnetic field. An increase in H_0 gives rise to an increase in the volume of the ferromagnetic phase and to a decrease in the volume of the paramagnetic phase in the sample. It should be noted that some other factors, for example, a change in the value of magnetization M_0, can also contribute to the intensity of the ferromagnetic resonance absorption line. However, the frequency–field dependence for line *F* is described well by equation (1) with a constant value $4\pi M_{eff} \approx 2$ kOe (see Fig. 2). Hence, the ferromagnetic domains in the crystal in magnetic fields used for measurements were magnetized to saturation.

As noted above, the mechanism of electronic phase separation is considered one of the possible mechanisms responsible for colossal magnetic resistance in lanthanum manganites. In this case, domains with various concentrations of carriers form in a crystal homogeneous in the crystallographic (chemical) sense. These domains differ in their conductivity and magnetic state. This heterophase state of the crystal corresponds to the state with minimal energy, that is, to the ground state. The inhomogeneous two-phase state must be very sensitive to the action of external parameters, for example, temperature, and the external magnetic field, which provides an explanation for the high value of magnetic resistance.

The occurrence of features in the width and intensity of magnetic resonance lines in the region of the highest magnetic resistance confirms that the two-phase magnetic state observed in this work is connected with anomalous magnetoresistive properties in $La_{0.7}Pb_{0.3}MnO_3$ single crystals (Fig. 1).

The situation when magnetic impurity phase separation is accomplished because the impurity is nonuniformly distributed in the process of synthesis of the crystals cannot be excluded. However, strong effects of the external magnetic field can hardly be expected in this case.

Thus, a two-phase magnetic (paramagnetic–ferromagnetic) state controlled by the magnitude of the external magnetic field was observed in $La_{0.7}Pb_{0.3}MnO_3$ single crystals by the magnetic resonance method.

REFERENCES

1. É. L. Nagaev, Usp. Fiz. Nauk **168**, 917 (1998) [Phys. Usp. **41**, 831 (1998)].
2. G. Allodi, Phys. Rev. B **56**, 6036 (1997).

3. N. N. Loshkareva, Yu. P. Sukhorukov, S. V. Naumov, *et al.*, Pis'ma Zh. Éksp. Teor. Fiz. **68**, 89 (1998) [JETP Lett. **68**, 97 (1998)].

4. M. Uehara, S. Mori, C. H. Chen, and S. W. Cheong, Nature **399**, 560 (1999).

5. E. Wollan and W. Koehler, Phys. Rev. **100**, 545 (1955).

6. A. K. Srivastava, C. M. Srivastava, R. Mahesh, and C. N. R. Rao, Solid State Commun. **99**, 161 (1996).

7. S. E. Lofland, S. M. Bhagat, H. L. Ju, *et al.*, J. Appl. Phys. **79**, 5166 (1996).

8. N. V. Volkov, G. A. Petrakovskiĭ, K. A. Sablina, and S. V. Koval', Fiz. Tverd. Tela (St. Petersburg) **41**, 2007 (1999) [Phys. Solid State **41**, 1842 (1999)].

9. A. J. Millis, Nature **392**, 147 (1998).

10. A. G. Gurevich and G. A. Melkov, *Magnetic Oscillations and Waves* (Fizmatlit, Moscow, 1994).

Translated by A. Bagatur'yants

<div align="center">

CONDENSED
MATTER

</div>

Polariton Luminescence in High-Purity Layers of AlGaAs Solid Solutions

T. S. Shamirzaev*, K. S. Zhuravlev, A. I. Toropov, and A. K. Bakarov

Institute of Semiconductor Physics, Siberian Division, Russian Academy of Sciences,
pr. Akademika Lavrent'eva 13, Novosibirsk, 630090 Russia
*e-mail: tim@isp.nsc.ru
Received January 11, 2000

Abstract—An additional polariton emission line caused by a change in the polariton energy distribution function owing to the exciton–exciton scattering is observed experimentally. The energy shift of this line and the variation in its intensity with increasing excitation power agree well with the results of calculations performed in the framework of the theoretical model proposed by Bisti [Fiz. Tverd. Tela **18**, 1056 (1976)]. © *2000 MAIK "Nauka/Interperiodica"*.

PACS numbers: 78.55.Cr; 71.36.+c

It is well known that the exciton–photon interaction leads to the formation of new excitations in a crystal—polaritons [1]. The shape of the polariton emission spectrum is determined by the distribution of polaritons in energy and in space [2–7]. At high excitation levels, an important factor in the formation of the polariton energy distribution and, hence, of the polariton spectrum is the exciton–exciton scattering. According to Bisti [7], at sufficiently high exciton concentrations, an additional polariton emission line should appear near the exciton resonance. So far, no experimental observations of such a line have been reported in the literature. The main obstacle to the experimental observation of the additional polariton emission line has been that the exciton photoluminescence spectra contain the lines associated with the excitons bound to background impurities and/or defects, which mask the possible features of the photoluminescence spectra near the exciton resonance. In our previous publications [8, 9], we reported on the fabrication of high-purity layers of direct-gap AlGaAs solid solutions. Near the exciton resonance, these layers exhibit a dominant spectral line with an intensity exceeding the intensities of the lines of bound and/or defect excitons by one or two orders of magnitude.

In this paper, we report on the experimental observation of the additional polariton emission line that appears in the low-temperature photoluminescence spectra of high-purity layers of AlGaAs solid solutions as a result of the exciton–exciton scattering. The polariton emission line occurs in the exciton resonance region and is strongly shifted (by up to 9 meV) toward the low-energy part of the spectrum with increasing excitation intensity.

We studied deliberately undoped $Al_xGa_{1-x}As$ layers obtained by molecular-beam epitaxy with AlAs contents $x = 0.21$ and 0.27. The details of the layer growth

process and the system used for recording the photoluminescence spectra were described in our previous paper [9]. Photoluminescence was excited by an Ar^+ laser with the wavelength 488 nm. The excitation power density could be varied from 3×10^{-4} to 900 W cm^{-2} with the use of neutral filters. The diameter of the laser spot focused on the sample was 200 μm.

Figure 1 presents the photoluminescence spectra of $Al_xGa_{1-x}As$ with $x = 0.21$. The spectra were measured with different excitation power densities at a temperature of 4.2 K. One can see that, at all excitation powers, the spectra have a dominant X line whose position on the energy axis does not depend on the excitation power density. In our previous paper [9], it was shown that the position of the maximum of the X line coincides with the minimum in the transmission spectrum, which allows us to associate this line with the lower polariton branch (LPB) luminescence [10, 11]. As the excitation power density increases up to 1 W cm^{-2}, a new Y line appears on the low-energy side of the X line; with a further increase in the excitation power density, this new line shifts to lower energies. From the literature, we know that the appearance of photoluminescence lines on the low-energy side of the exciton resonance can be caused by several factors: (1) annihilation of excitons bound to shallow-level background impurities and/or defects [12]; (2) formation of biexcitons and exciton molecules [13, 14]; (3) radiative recombination of free excitons scattered from phonons and/or plasmons [15, 16]; and, finally, (4) in high-purity materials, the appearance of additional lines near the exciton resonance may be caused by the interaction of excitons with light [3, 4, 7].

To identify the Y line, we studied the dependence of its spectroscopic parameters on the excitation power density. Figure 2 shows the energy shift of the Y line

relative to the *X* line versus the excitation intensity for AlAs layers with $x = 0.21$ and 0.27. The displacement of the *Y* line in energy with increasing excitation power density unambiguously testifies that this line is unrelated to either the recombination of excitons localized at impurities and defects or to the radiative recombination of phonon-scattered free excitons, because the positions of lines related to these processes should not depend on the excitation intensity. In addition, the displacement of the *Y* line is much greater than that expected for the biexciton line (1–2 meV) [14, 17]. At the same time, the direction and the nonlinear character of the displacement of the *Y* line with increasing pump intensity coincide with those expected for the line caused by the radiative recombination of free plasmon-scattered excitons, as well as for the additional line caused by the LPB luminescence. To select one of these versions, we compared the experimental dependences with the calculated values of the position of the plasmon replica of the *X* line and the position of the additional line of LPB luminescence. The plasmon frequency ω_{pl} is determined by the expression [15]

$$\omega_{pl} = [4\pi\rho e^2/(\varepsilon_\infty\mu)]^{0.5},$$

where *e* is the electron charge, ρ is the electron–hole plasma density, ε_∞ is the high-frequency permittivity, and μ is the reduced mass ($\mu^{-1} = m_e^{-1} + m_h^{-1}$, where m_e and m_h are the effective masses of electrons and holes). The plasmon frequency increases with increasing concentration of electrons and holes. To calculate the value of ω_{pl}, we used the values of ε_∞ and μ presented in the literature [12] for AlGaAs with the corresponding AlAs content; we also estimated the variation in the concentration of nonequilibrium electrons and holes with increasing excitation power density by using the diffusion length (1 μm) and the lifetime (10^{-9} s) that are typical of nonequilibrium charge carriers in GaAs [12]. The calculated dependence of the plasmon energy $\hbar\omega_{pl}$ on the excitation power density is represented by the dashed line in Fig. 2. From this figure, one can see that the experimental positions of the *Y* line deviate widely from the calculated dependence. As for the additional LPB emission line, according to the calculations performed by Bisti [7], the dependence of the energy position of this line on the excitation intensity should obey a logarithmic law. The approximation of the experimental data by a function of the type $f(n) = \beta\log(n)$, where *n* is the exciton concentration and β is a constant factor, is represented in Fig. 2 by the solid line. One can see that this curve agrees well with the experimental data.

Bisti [7] also calculated the dependence of the intensity of the additional LPB emission line on the pump power. The calculations show that the intensity of this line increases faster than by the linear law, but somewhat slower than by the $n^{3/2}$ law. Since the intensity of the *X* line linearly increases with the excitation power
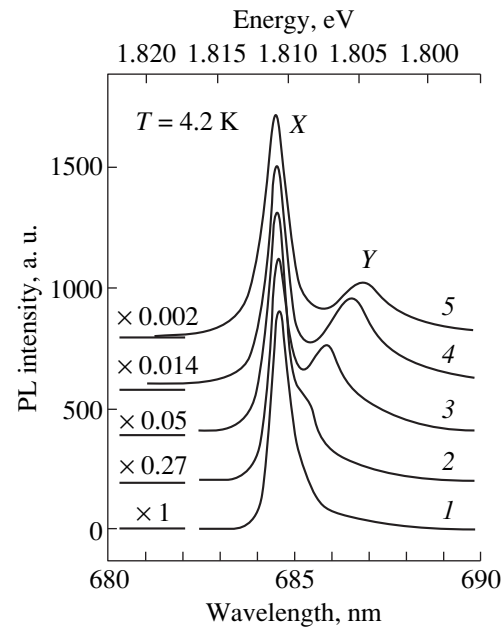

Fig. 1. Photoluminescence spectra of an $Al_xGa_{1-x}As$ layer with AlAs content $x = 0.21$ at 4.2 K for the excitation power densities (*1*) 0.3, (*2*) 1.2, (*3*) 6.3, (*4*) 23, and (*5*) 160 W cm^{-2}.
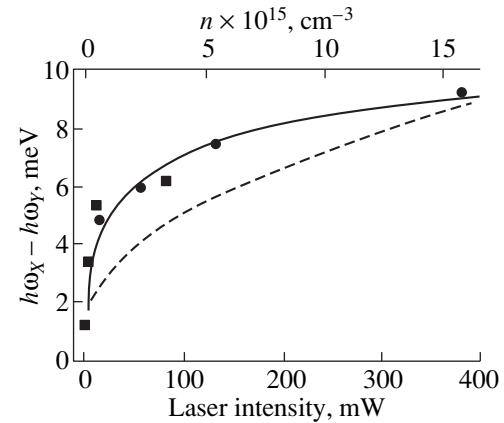
Fig. 2. Energy shift of the *Y* line relative to the *X* line as a function of the excitation power density for $Al_xGa_{1-x}As$ layers with $x =$ (■) 0.21 and (●) 0.27. The calculated dependences of the positions of the plasmon replica of a free exciton and the additional LPB emission line on the excitation intensity are represented by the dashed and solid lines, respectively.

density [9], it is convenient to analyze the behavior of the intensity of the polariton emission line for layers with different AlAs contents by considering the ratio of the intensities of the *Y* and *X* lines (I_Y/I_X). The dependences of the quantity I_Y/I_X on the excitation power for layers with $x = 0.21$ and 0.27 are shown in Fig. 3. One can see that the relative intensity of the *Y* line slightly increases with the pump intensity as the latter grows from 0.1 to 10 mW; with a further increase in the pump
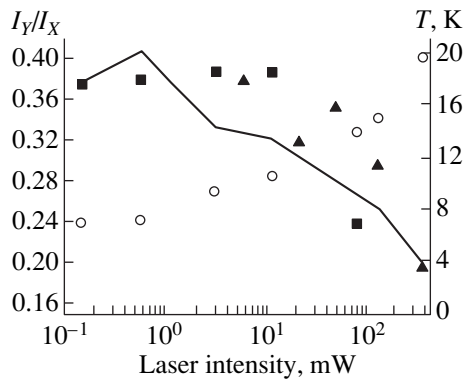
Fig. 3. Dependences of the intensity ratio of the X and Y lines for $Al_xGa_{1-x}As$ layers with x = (■) 0.21 and (▲) 0.27 (the left vertical axis) and (○) the dependence of the exciton temperature (the right vertical axis) on the excitation power. The solid line represents the approximation of the ratio I_Y/I_X by a function of the type $f(n) = n^{a-1}T(n)^{-5/4}$.

power, the Y line intensity decreases. The behavior of the relative intensity of the Y line differs from that predicted by Bisti [7]. However, it should be noted that an increase in the pump power leads to an increase not only in the concentration of excitons, but also in their temperature (T), which causes a decrease in the intensity of the additional polariton emission line in proportion to $T^{5/4}$ [7]. To determine the values of the exciton temperature for different excitation power densities, we used the approximation of the high-energy wing of the X line by a function of the type $b\exp(-\hbar\omega/kT)$, where b is a constant, $\hbar\omega$ is the photon energy, and k is the Boltzmann constant; the resulting values are presented in Fig. 3. Taking into account that the intensity of the X line linearly increases with increasing excitation power density [9], we approximated the experimental dependence of the intensity ratio of the X and Y lines on the excitation power by the formula $I_Y/I_X = n^{a-1}T(n)^{-5/4}$. The result of this approximation is shown by the solid line in Fig. 3. One can see that only qualitative agreement is achieved between the experimental data and the calculations; this occurs for the value of the adjustable parameter $a = 1.09$, which is less than the expected value $a = 3/2$ [9]. The discrepancy between the experimental and the calculated dependences can be explained, first, by the deviation of the spatial polariton distribution from the uniform one used by Bisti [7] and, second, by the deviation of the polariton energy distribution in the layers under study from that calculated by Bisti [7] because of the presence of the additional mechanism of polariton scattering, namely, the scattering from the inhomogeneities of the spatial distribution of Ga and Al atoms in the AlGaAs solid solutions; the contribution of this mechanism to the formation of the polariton energy distribution was neglected by Bisti [7].

Thus, in our experiments, we studied the polariton photoluminescence in high-purity AlGaAs layers. It was found that, when the excitation power density

exceeds 1 W cm^{-2}, a new line appears in the exciton resonance region of the photoluminescence spectra. With increasing excitation intensity, the maximum of this line shifts toward the low-energy part of the spectrum in proportion to the logarithm of the excitation intensity. The experimental results are explained on the basis of the assumption that the appearance of the new line is related to the change produced by the exciton–exciton scattering in the energy distribution of polaritons belonging to the lower polariton branch.

REFERENCES

1. J. J. Hopfleld, Phys. Rev. **112**, 1555 (1958).
2. Yu. Toyozawa, Prog. Theor. Phys. Suppl. **12**, 111 (1959).
3. W. C. Tait and R. L. Weiher, Phys. Rev. **178**, 1404 (1967).
4. G. Weisbuch and R. G. Ulbrich, Phys. Rev. Lett. **39**, 654 (1977).
5. V. V. Travnikov and V. V. Krivolapchuk, Zh. Éksp. Teor. Fiz. **85**, 2087 (1983) [Sov. Phys. JETP **58**, 1210 (1983)].
6. V. V. Rossin, Fiz. Tverd. Tela (Leningrad) **31**, 218 (1989) [Sov. Phys. Solid State **31**, 472 (1989)].
7. V. E. Bisti, Fiz. Tverd. Tela (Leningrad) **18**, 1056 (1976) [Sov. Phys. Solid State **18**, 603 (1976)].
8. K. S. Zhuravlev, A. I. Toropov, T. S. Shamirzaev, *et al.*, Pis'ma Zh. Tekh. Fiz. **25**, 8 (1999) [Tech. Phys. Lett. **25**, 595 (1999)].
9. K. S. Zhuravlev, A. I. Toropov, T. S. Shamirzaev, and A. K. Bakarov, Appl. Phys. Lett. **76** (2000) (in press).
10. Yu. V. Zhilyaev, G. R. Markaryan, V. V. Rossin, *et al.*, Fiz. Tverd. Tela (Leningrad) **28**, 2688 (1986) [Sov. Phys. Solid State **28**, 1506 (1986)].
11. D. D. Sell, S. E. Stokowski, R. Dingle, and J. V. DiLorenzo, Phys. Rev. B **7**, 4568 (1973).
12. L. Pavesi and M. Guzzi, J. Appl. Phys. **75**, 4779 (1994).
13. R. T. Phillips, D. J. Lovering, G. J. Denton, and G. W. Smith, Phys. Rev. B **45**, 4308 (1992).
14. T. W. Steiner, A. G. Steele, S. Charboneau, *et al.*, Solid State Commun. **69**, 1139 (1989).
15. A. A. Klochikin, B. S. Razbirin, T. Amand, *et al.*, J. Phys. C **19**, 4237 (1986).
16. A. A. Klochikin, B. S. Razbirin, D. K. Nelson, *et al.*, Phys. Status Solidi B **147**, 727 (1988).
17. O. Akimoto and E. Hanamura, J. Phys. Soc. Jpn. **33**, 1537 (1972).

Translated by E. Golyamina

Elastic and Inelastic Tunneling of Photoelectrons from the Dimensional Quantization Band at a p^+-GaAs-(Cs,O) Interface into Vacuum

D. A. Orlov[1], V. É. Andreev[2], and A. S. Terekhov[1, 2]

[1] *Institute of Semiconductor Physics, Siberian Division, Russian Academy of Sciences,*
pr. Akademika Lavrent'eva 13, Novosibirsk, 630090 Russia
[2] *Novosibirsk State University, ul. Pirogova 2, Novosibirsk, 630090 Russia*

Received January 20, 2000

Abstract—The photoemission of electrons from a p^+-GaAs surface with negative electron affinity was studied experimentally at 4.2 K. A narrow peak and its phonon replicas were observed in the distribution of emitted electrons over the energies of longitudinal motion. These replicas are caused by elastic and inelastic electron tunneling from the bottom of the dimensional quantization band in the near-surface spatial-charge region through the potential barrier of the (Cs,O) activating coverage with emission of LO phonons. The measured position of the peak corresponding to elastically tunneling electrons is close to the calculated one. © *2000 MAIK "Nauka/Interperiodica".*

PACS numbers: 73.40.Gk; 79.60.Jv

More than 30 years ago, it was found [1] that an atomically clean p^+-GaAs surface covered with cesium and oxygen occurs in the state that is characterized by negative electron affinity (NEA). In this state, the vacuum level in the near-surface region is below the bottom of the conduction band in the semiconductor bulk. A remarkable property of GaAs with negative electron affinity is a high probability of the egress of thermalized photoelectrons into vacuum. This property of the p^+-GaAs-(Cs,O) surface is widely used for creating light-sensitive devices, sources of spin-polarized electrons, and sources of electrons with a small spread in kinetic energies. In spite of the long history of investigations, the electronic processes at a surface with negative electron affinity that determine the emission probability, the distribution of emitted electrons over energy, and the angular distributions of these electrons are still not understood. For example, the theoretical predictions that the dimensional quantization of the electronic spectrum and electron–phonon interaction in the near-surface spatial-charge region is important in photoemission from semiconductors with negative electron affinity have not received theoretical corroboration so far. Finding the corresponding features of the energy distribution (spectrum) of photoemitted electrons can serve as such corroboration. However, weak features in the derivative spectra of photoemitted electrons measured at 293 and 77 K were interpreted as the results of emission of an LO phonon by an electron in the near-surface spatial-charge region in only one of the previously published works [2]. The lack of reliable experimental data obtained at helium temperatures, when the thermal broadening does not prevent observ-ing the features in the energy distributions of emitted electrons associated with dimensional quantization levels and with the processes of single-phonon emission by photoelectrons, hinders the development of a detailed picture of photoemission from semiconductors with negative electron affinity.

In this work, spectra of electrons $N_e(\varepsilon)$ photoemitted from GaAs with NEA into vacuum were measured at a temperature of 4.2 K. The position of features observed in the spectra indicated that these features are due to the elastic and inelastic tunneling of electrons from the bottom of the dimensional quantization band in the near-surface region of the semiconductor into vacuum through the surface potential barrier of the (Cs,O) activating coverage with emission of LO phonons of gallium arsenide.

Vacuum photodiodes were made for the experiments. These photodiodes consisted of a semitransparent GaAs photocathode on a glass [3] and a flat metallic anode; both electrodes were hermetically fixed with an indium gasket on the opposite ends of a cylindrical case made of alumina-based ceramics. The diameters of the photocathode and anode were 18 mm, and the distance between them was 0.5 mm. Photocathodes were made of epitaxial GaAs layers with the (100) surface orientation doped with zinc to a concentration of 7×10^{18} cm^{-3}, which provided the highest value of the quantum yield [3]. The procedure used for preparing an atomically clean GaAs surface, its atomic structure, and electronic properties were described in [4]. The activation of GaAs and the encapsulation of photodiodes were carried out in a vacuum of 10^{-9} Pa. For measurements,

photodiodes were placed in an optical cryostat with liquid helium. The photocathode was illuminated from the glass side by monochromatic light in a spot 1 mm in diameter. The measurement of the spectrum of photoemitted electrons was performed by the retarding potential method with the use of modulation of the retarding field between the photocathode and anode. The variable component of the photocurrent proportional to $N_e(\varepsilon)$ was recorded by the synchronous detection method. It is evident that a parallel-plate analyzer with a uniform retarding field integrates the angular distribution of electrons and allows the distribution to be measured only along the longitudinal component of the kinetic energy $\varepsilon_{\parallel} = p_{\parallel}^2/2m_0$, where $p_{\parallel}$ is the electron momentum component parallel to the photocurrent vector. Because of angular averaging, the analyzer with a uniform retarding field measures a wide energy distribution over the longitudinal energy even in the case of emission of monoenergetic electrons if their angular distribution is smeared over a solid angle of 2π.

Figure 1 displays a spectrum of photoelectrons measured at 4.2 K. The energy of exciting photons was 1.70 eV. It is evident in the figure that the main part of the spectrum represents a wide band lying in the range of energies from the bottom of the conduction band ε_c in the semiconductor bulk to the vacuum level ε_{vac}. A high-energy wing due to the emission of ballistic and hot electrons is observed at energies larger than ε_c. The observed emission of nonthermalized electrons is caused by the small thickness (0.2 µm) of the p^+-GaAs layer in the given photocathode at which a significant part of the primary photoelectrons are excited at small distances from the emitting surface. These distances are smaller than the length of electron thermalization in p^+-GaAs [5]. The features due to emission into vacuum of

ballistic photoelectrons excited by light from the band of light and heavy holes to the conduction band ($lh \longrightarrow c$ and $hh \longrightarrow c$ transitions, respectively) are evident in the $\partial N_e/\partial\varepsilon_{\parallel}$ spectrum in Fig. 1. A comparison of the calculated and measured energies of ballistic electrons was used for calibrating the energy scale of the energy analyzer. The accuracy of calibration was ±10 meV or better.

The most interesting features of the spectrum of photoelectrons in Fig. 1 are designated as I_0–I_2. The I_0 peak is located 25 ± 5 meV below the bottom of the conduction band in the semiconductor bulk. The shape of this peak in the vicinity of its maximum and in the high-energy wing is described well by the Gaussian profile with a half-width of 30 meV. Weaker features I_1 and I_2 are observed on the low-energy side of the I_0 peak. The occurrence of these features becomes quite evident after computing the derivative $\partial N_e/\partial\varepsilon_{\parallel}$, which is also shown in Fig. 1. The energy gaps I_0–I_1 and I_1–I_2 between the features turned out to be approximately the same and equal to 38 ± 3 meV. This value coincides, within the accuracy of the experiment, with the energy of longitudinal long-wave optical phonons $\hbar\omega_{LO} = 36.7$ meV in GaAs.

In order to determine the origin of the line I_0, the position of quasistationary levels of dimensional quantization for electrons in the near-surface region of band bend was calculated. The general view of the potential at the surface of p-GaAs with negative electron affinity shown in Fig. 2 includes the potential $V_{bb}(z)$ in the spatial-charge region in GaAs, the Coulomb potential $V_m(z)$ of mirror image forces in vacuum, and also a thin potential barrier of a triangular shape $V_{bar}(z)$ due to the electrostatic potential of the (Cs,O) dipole layer. The height of the triangular barrier was assumed in calculations to be equal to the electron affinity 4.0 eV at the initial Ga-stabilized GaAs(100)c(8 × 2) reconstructed surface. The barrier width at the base was taken coincident with the thickness of the activating (Cs,O) layer, which, according to the estimate [6], approximately equals 0.7 nm. The band bend φ_0 at the GaAs surface with negative electron affinity was assumed to be uniform along the surface and equal to 0.5 eV. The screening of the surface charge by both the ionized acceptors and free holes was taken into account in the calculation of the $V_{bb}(z)$ potential in the semiconductor. In spite of the low temperature, it was suggested that the acceptors are fully ionized, because the ionization energy of Zn in GaAs decreases to zero at the given doping level [7]. The discreteness of charges and fluctuations in their spatial distribution were not taken into account. The Poisson and Schrödinger equations were solved numerically. The results of calculations are displayed in Fig. 2. It is evident in the figure that two dimensional quantization bands—ε_1 and ε_2—occur in the spatial-charge region at the given doping level. Their minima are located 20 and 100 meV below the bottom of the
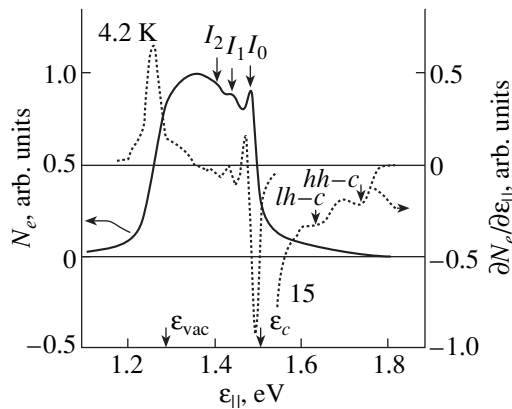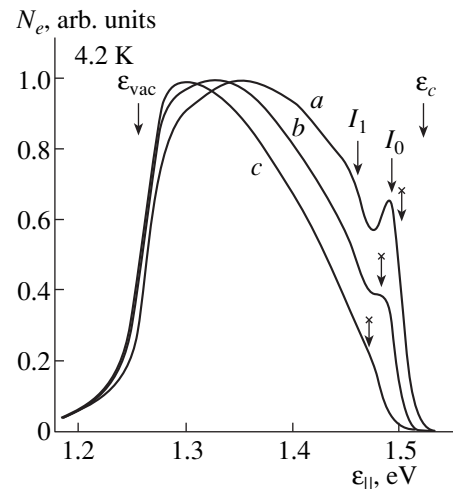

Fig. 1. Low-temperature spectrum of photoelectrons and derivative spectrum of photoemitted electrons measured at the energy of photons equal to 1.7 eV.

conduction band ε_c in the semiconductor bulk. It is also evident that the wave function $\psi(z)$ of an electron residing at the level ε_1 has a maximum in the vicinity of the boundary of the spatial-charge region and a tail extended into the semiconductor bulk. The results obtained suggest the following interpretation of the spectrum of electrons shown in Fig. 1. Nonequilibrium electrons thermalized in the semiconductor bulk and reaching the surface through diffusion are captured at the upper dimensional quantization band. The probability of such a capture is rather high because of the small value of $\varepsilon_c - \varepsilon_1$ and the tail $|\psi|^2$ extended into the semiconductor bulk. Part of the captured electrons tunnel into vacuum. The I_0 peak corresponds to elastic and the I_1 and I_2 peaks, to inelastic tunneling of electrons with emission of one and two LO phonons, respectively. The small width ($\delta\varepsilon = 30$ meV) of the I_0 peak as compared to the total kinetic energy ($\varepsilon_0 = 220$ meV) of electrons in this peak means that elastic tunneling proceeds within a small angle θ relative to the normal to the surface. If it is supposed that the peak width is determined by a small broadening of the angular distribution of electrons, then the value of θ, equal to $\frac{1}{2}\sqrt{\delta\varepsilon/2\varepsilon_0}$, does not exceed 7°.

The broadening of the I_0 peak can be caused both by the angular distribution of the emitted electrons and by fluctuations in the position of the bottom of the dimensional quantization band. These fluctuations are caused by fluctuations of the potential in the spatial-charge region due to the random nature of the spatial distribution of surface states and acceptors. In order to elucidate the effect of band bottom smearing on the broadening of the I_0 peak, the spectra of photoelectrons were measured at various energies of exciting photons. The results of measurements are shown in Fig. 3. Note that these measurements were performed on another photodiode in which the I_0–I_2 features were considerably weaker. The I_1 feature at the threshold of LO phonon emission manifested itself as a weak bend in the spectrum, and the I_2 feature was observed only in the derivative spectrum of photoemitted electrons. Figure 3 demonstrates that the I_0 peak was observed under excitation of electrons by light with the energy of photons equal to 1.52 eV, which is close to the band gap width of GaAs. However, this peak virtually disappeared on decreasing the $\hbar\omega$ by as little as 30 meV. The half-width of the level determined from this experiment was approximately equal to 30 meV, which, within the accuracy of the experiment, coincides with the half-width of the I_0 peak in the spectrum of photoelectrons. Hence, the half-width of the I_0 peak is mainly determined by the broadening of the dimensional quantization level near the semiconductor surface with negative electron affinity. The angular distribution of electrons emitted in the I_0 peak is apparently considerably
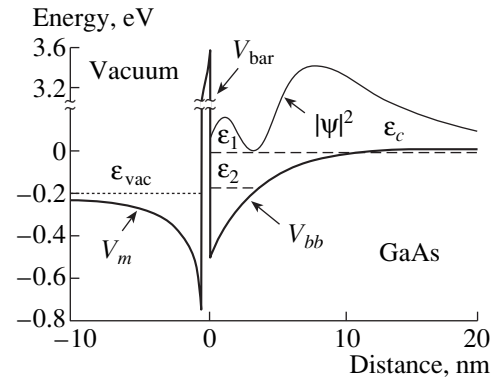
Fig. 2. Energy diagram of the near-surface region of GaAs with negative electron affinity. The $|\psi(z)|^2$ function that corresponds to the stationary solution of the Schrödinger equation with the energy ε_1 in GaAs is given in the figure.

Fig. 3. Low-temperature spectra of photoelectrons measured at the energies of photons equal to (*a*) 1.52, (*b*) 1.50, and (*c*) 1.49 eV. The initial energies of photoelectrons are marked with crosses. The maximums of spectra a–c are normalized.

smaller than 7°, which indicates that the tangential component of the electron momentum is conserved.

In addition to elastic tunneling with the conservation of the momentum component parallel to the surface, which explains the small angular broadening of the I_0 peak, diffuse tunneling of electrons is possible without conservation of the momentum component parallel to the surface. This diffuse tunneling is caused by the elastic scattering of the electron momentum by the structurally disordered surface and activating coverage. As was noted previously, if the angular distribution of electrons is close to isotropic, the $N_e(\varepsilon_\parallel)$ measured by a parallel-plate analyzer with a uniform retarding field is broadened. We believe that this mechanism is responsible for the monotonic part of the spectrum of photoe-

mitted electrons extending from the bottom of the conduction band to the vacuum level. Experimental evidence for the validity of this statement was obtained in [8].

Thus, the emission of electrons from a semiconductor with negative electron affinity represents their tunneling from the upper subband of dimensional quantization in the near-surface potential well into vacuum. Elastic tunneling of electrons with conservation of the tangential momentum component, inelastic tunneling of electrons with emission of LO phonons, and also tunneling without conservation of the tangential momentum component due to electron scattering by surface defects and fluctuations of the potential near the surface exert a significant effect on the spectrum of emitted electrons. The role of the lower band of dimensional quantization calls for further investigation.

ACKNOWLEDGMENTS

REFERENCES

1. J. J. Sheer and J. van Laar, Solid State Commun. **3**, 189 (1965).
2. A. S. Terekhov and D. A. Orlov, Pis'ma Zh. Éksp. Teor. Fiz. **59**, 827 (1994) [JETP Lett. **59**, 864 (1994)].
3. Yu. B. Bolkhovityanov, B. V. Morozov, A. G. Paulish, *et al.*, Pis'ma Zh. Tekh. Fiz. **16**, 25 (1990) [Sov. Tech. Phys. Lett. **16**, 253 (1990)].
4. O. E. Tereshchenko, S. I. Chikichev, and A. S. Terekhov, Appl. Surf. Sci. **214**, 7580 (1998).
5. B. P. Zakharchenya, D. N. Mirlin, V. I. Perel', and I. I. Reshina, Usp. Fiz. Nauk **130**, 459 (1982) [Sov. Phys. Usp. **25**, 143 (1982)].
6. C. Y. Su, W. E. Spicer, and I. Lindau, J. Appl. Phys. **54**, 1413 (1983).
7. F. Ermanis and K. Wolfstirn, J. Appl. Phys. **37**, 1963 (1966).
8. S. Pastuszka, D. Kratzman, D. Schwalm, *et al.*, Appl. Phys. Lett. **71**, 2967 (1997).

Translated by A. Bagatur'yants

CONDENSED
MATTER

Resonance Interaction of Optical Phonons with Localized States

L. A. Falkovsky

Landau Institute for Theoretical Physics, Russian Academy of Sciences, ul. Kosygina 2, Moscow, 117334 Russia
Received January 17, 2000; in final form, January 25, 2000

Abstract—The optical-phonon Green's function averaged over the positions of defects—both point and line—is calculated with allowance for possible localized states near the boundary of the continuous spectrum and for their intrinsic damping. The frequency-transfer dependence of the cross section for Raman scattering is calculated with the aid of this Green's function. © *2000 MAIK "Nauka/Interperiodica"*.

PACS numbers: 78.30.-j; 61.72.Ji; 61.72.Lk

1. Interest in studying the effect of defects on the dynamical properties of crystals has been rekindled in recent years (see, for example, [1]). This is explained by a few factors. First, the desire to work with high-purity samples, samples of small dimensions, and samples subjected to external pressures calls for studying the effect of impurities or boundaries, in particular, strain fluctuations that exist near heterointerfaces owing, for example, to interfacial lattice mismatch. Second, inelastic light scattering seems the most appropriate method of investigation in the case being discussed, since the positions and shapes of Raman lines of optical phonons are highly sensitive to the effect of defects [2]. At the same time, the present-day micro-Raman procedure, which employs a focused laser spot about 1 μ in diameter, makes it possible to explore spatial changes in defect or strain concentrations with a high spatial resolution.

It should be noted—to the best of my knowledge, it was I.M. Lifshits [3] who was the first to indicate this—that the problem of the effect of defects on phonon spectra is very similar to the corresponding problem of electron interaction with impurities in a metal or a semiconductor. In either case, defects reduce the mean free path of band particles, electrons, or phonons. Moreover, there can arise localized states. For semiconductors, this situation is treated in terms of tails that the density of states develops in the forbidden band (it is the problem that was considered in greatest detail in the studies of I.M. Lifshits; see also [4]). Owing to the presence of defects, some states in the conduction band (in some neighborhood of its boundary in general and everywhere in the one- and two-dimensional cases) may also prove to be localized (more precisely, non-propagating). Localization in electron systems still remains one of the hot points in mesoscopic physics; for the system of acoustic phonons, it was considered in [5–7].

There are, however, some important distinctions between the cases electrons and phonons, and two of these are drastic—the type of statistics and the fact that there is no long-range Coulomb interaction for phonons (at least in nonpolar dielectrics). Further, it should be recalled that, even in perfect crystals, optical phonons have an intrinsic damping Γ^{intr}, which is associated with their decay into a pair of acoustic or optical phonons and which is proportional to the mean square of the displacement of atoms; that is, it is on the order of 10^{-2} of the natural frequency ω_0, amounting to a few Kelvin degrees, a value that determines the intrinsic width of a given Raman line. This entails yet another important distinction: the mean free path of optical phonons cannot be very large on the atomic scale, $l \simeq a\sqrt{\omega_0/\Gamma^{intr}}$. Finally, impurity states in a semiconductor are shallow because of a large dielectric permittivity and because of a small (as a rule) effective mass. In the case of a weak interaction with a defect, there are no phonon states localized near a point defect. Such states arise only if the potential of the above interaction exceeds some critical value. Weak interaction can result, however, in a localization of phonon states near an extended defect like a line dislocation or a crystallite boundary, which exemplifies a planar type of defect.

So far, the effect of intrinsic damping on the interaction of band and localized states has not been considered. In the present study, we will compare the effect of point and line defects, considering that localized states can be formed near the boundary of the optical phonon branch and taking into account their intrinsic damping. We will see that, owing to intrinsic damping, localized states contribute even in the linear approximation in the defect concentration.

2. Let us consider the optical branch of the phonon spectrum near its extremum. For the sake of definiteness, we assume that this extremum is a maximum and that it occurs at the center of the Brillouin zone. Under the conditions of a Raman experiment, the important values of the wave vector are those that are determined by the wavelength of incident light. Since these values are much smaller than the dimensions of the Brillouin

zone, it is quite legitimate to make use of an expansion of the spectrum near the extremum,

$$\omega^2 = \omega_0^2 - s^2 k^2 - i\omega\Gamma^{intr}.$$

In this representation of the spectrum, it is considered that the equations of lattice dynamics are invariant under time reversal. If we disregard the possible degeneracy of the branches, there exists only one dispersion parameter s, its value being on the order of the speed of sound $s \simeq \omega_0 a/\pi \simeq 10^6$ cm/s.

The interactions of phonons with defects can be represented as the sum over defects situated at the points $\mathbf{r}_n$,

$$U(\mathbf{r}) = \sum_n u(\mathbf{r} - \mathbf{r}_n) = \sum_{n, q} u(\mathbf{q}) e^{i\mathbf{q}(\mathbf{r} - \mathbf{r}_n)}.$$

For line defects, $(\mathbf{r} - \mathbf{r}_n)$ is a two-dimensional vector in the plane orthogonal to the defect axis z, while $u(\mathbf{q})$ is independent of q_z.

At present, distances at which the potential of a defect must decrease cannot be determined from experimental data. The scheme where the non-Coulomb part of the atom interaction can be taken into account in the approximation of a few nearest neighbors is appropriate for calculating phonon spectra. This is equivalent to the assumption that the interaction is short-range. In addition, the opinion that a significant part of the perturbation that is caused by lattice mismatch at heterointerfaces also relaxes at atomic distances from the interface is prevalent among the physics community. For this reason, we will consider short-range defects; that is, we assume that their radius r_0 is much smaller than the mean free path $r_0 \ll a\sqrt{\omega_0/\Gamma^{intr}}$ and that the Fourier component of the interaction potential can be set to a constant $u(\mathbf{q}) = u_0$. For an isotopic defect, this statement is rigorous; in this case, the quantity u_0 is proportional to the mass difference between the defect and the host atom, $u_0 = (m_0 - m) r_0^3 \omega^2/m_0$, m and m_0 being the masses of the defect atom and the host atom, respectively.

3. The cross section for single-phonon Raman scattering, a quantity that can be directly measured in experiments, is proportional to the imaginary part of the retarded Green's function for phonons. It must be averaged over defect positions. An appropriate method for this is represented by a version of the well-known diagram technique for impurities [8]; a detailed account of this version is given in [9]. Expanding the equation for the Green's function in the interaction with defects, performing averaging over their positions, and summing the resulting series of leading nonintersecting diagrams, we arrive at the Dyson equation for the Fourier component of the averaged Green's function in the form

$$D(\mathbf{k}, \omega)^{-1} = D_0(k, \omega)^{-1} + cu_0\left(1 + u_0\sum_q D(\mathbf{q}, \omega)\right)^{-1}, \quad (1)$$

where

$$D_0(k, \omega) = (\omega_0^2 - s^2 k^2 - i\omega\Gamma^{intr} - \omega^2)^{-1}$$

is the Green's function in the absence of defects, while c is the concentration of defects. Summation (integration) is performed with respect to the three-dimensional vector $\mathbf{q}$ for point defects and with respect to the two-dimensional vector $\mathbf{q}_\perp$ in the case of line defects, the third component q_z being coincident, in the latter case, with the corresponding component of the vector $\mathbf{k}$ on the left-hand side of equation (1). The condition that makes it possible to disregard diagrams with intersections can be represented as $\omega_0/\Gamma \gg 1$ for point defects and as $\ln/(\omega_0/\Gamma) \gg 1$ for line defects.

Instead of $D(\mathbf{k}, \omega)$, we introduce an unknown function ζ via the relation $D(\mathbf{k}, \omega)^{-1} = \zeta - s^2 k^2$ and an independent complex variable $\zeta_0 = \omega_0^2 - i\omega\Gamma^{intr} - \omega^2$. Substituting these quantities into equation (1) and performing relevant integrations, we arrive at an algebraic equation for ζ instead of the above integral equation. Specifically, we have

$$\zeta = \zeta_0 + n_c\omega_0^3\left(\frac{\kappa}{\lambda} - \kappa + \frac{\pi}{2}\sqrt{-\zeta}\right)^{-1} \quad (2)$$

for point defects and

$$\zeta = \zeta_0 + n_c\omega_0^2\left(\lambda^{-1} - \ln\frac{\kappa^2}{s^2 k_z^2 - \zeta}\right)^{-1} \quad (3)$$

for line defects. The dimensionless coupling constant for interactions with defects λ (it can be negative) and the number of defects n_c in the region of atomic dimensions are related to the original quantities u_0 and c as $\lambda = u_0\kappa/6\pi^2 s^3$, $u_0 \sim \omega_0^2 a^3$, and $n_c = 6\pi^2 cs^3/\omega_0^3$ for point defects and as $\lambda = u_0/4\pi s^2$, $u_0 \sim \omega_0^2 a^2$, and $n_c = 4\pi cs^2/\omega_0^2$ for line defects, where the cutoff parameter κ has the scale of the frequency ω_0. The cutoff parameter for the integrals that are divergent at the upper limit is determined by the fact that integration with respect to $\mathbf{q}$ is actually performed over the Brillouin zone. For the region $|\omega_2 - \omega_0^2| \ll \omega_0^2 \sim \kappa^2$ (and this is precisely the region of our interest), where the peak of Raman scattering occurs (that is, under the condition $|\zeta| \ll \kappa$), the use of this cutoff is quite legitimate, since, for such ζ values, only the analytic properties of the spectrum in the vicinity of its boundary are of importance. In this case, the resulting dependences on κ can, of course, be
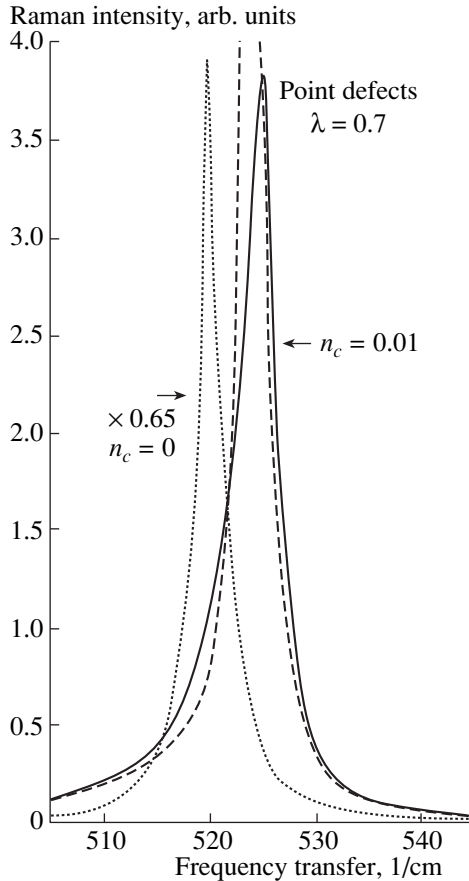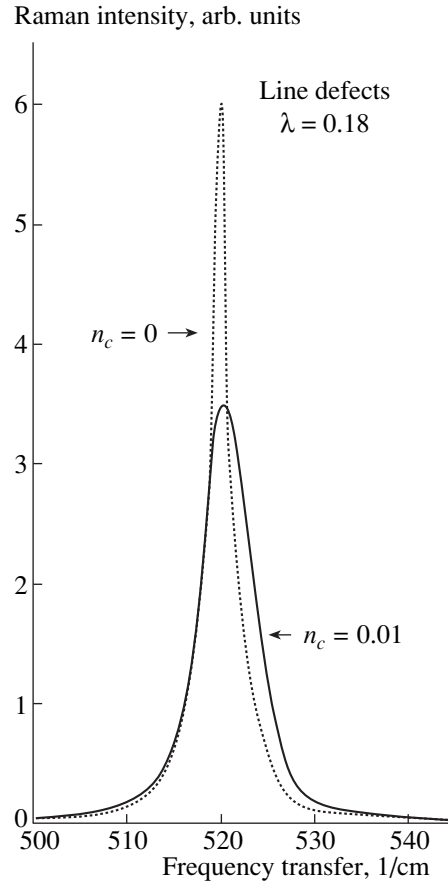
Fig. 1.

Fig. 2.

considered only as qualitative ones. Finally, we must specify the choice of the branches of the logarithm and the squared root: in equations (2) and (3), we imply their values in the upper complex half-plane. As a matter of fact, each of these equations appears to be a pair of equations for the real and imaginary parts.

4. In Figs. 1–4, we present the cross section for the Raman scattering [apart from the Bose factor $1 - \exp(-\omega/T)$], namely, $\mathrm{Im}(1/\zeta)$, as a function of frequency transfer ω at $k = 0$. These results were obtained by solving equations (2) and (3). For the sake of definiteness, the calculations were performed with the values of $\omega_0 = 520$ cm^{-1} and $\Gamma^{\mathrm{intr}} = 3.2$ cm^{-1}, which correspond to pure silicon; the results for this case are illustrated by dotted curves. Here, the Raman spectrum shows the Lorentzian frequency-transfer dependence

$$\mathrm{Im}\frac{1}{\zeta} = \omega\Gamma^{\mathrm{intr}}/[(\omega_0^2 - \omega^2)^2 + (\omega\Gamma^{\mathrm{intr}})^2]$$

with a width equal to Γ^{intr} at half-maximum.

For a first approximation, a qualitative analysis of equations (2) and (3) at small n_c can be performed by substituting ζ_0 instead of ζ into the expressions on the right-hand sides of these equations and by separating

the real and imaginary parts. This approximation—it will be referred to as the unrenormalized one—corresponds to substituting $D_0(k, \omega)$ for $D(k, \omega)$ in the expression on the right-hand side of (1). The unrenormalized approximation was analyzed in detail elsewhere [9], the corresponding dependences being shown in Figs. 1, 3, and 4 by dashed curves.

It is obvious from equations (2) and (3) that the coupling constant for phonon interaction with defects and the cutoff parameter appear only in the combination $1/\lambda^* = (\lambda^{-1} - 1)\kappa$ for point defects and in the combination $1/\lambda^* = \lambda^{-1} - \ln(\kappa^2/\omega_0\Gamma^{\mathrm{intr}})$ for line defects. For the sake of definiteness, the graphs were plotted for the cutoff parameter κ set to ω_0.

There are no localized states for point defects when $\lambda < 1$ and for line defects when $\lambda < 1/\ln(\kappa^2/\omega_0\Gamma^{\mathrm{intr}})$. In those cases, defects manifest themselves only in the fact that phonons of the continuous spectrum are elastically scattered on them, whereby the phonon line shifts toward higher frequencies and broadens. The contribution of scattering to the phonon width increases with increasing distance from the boundary ($\omega^2 < \omega_0^2$), because the number of final states for scattered phonons increases. The curve ceases to be of a Lorent-
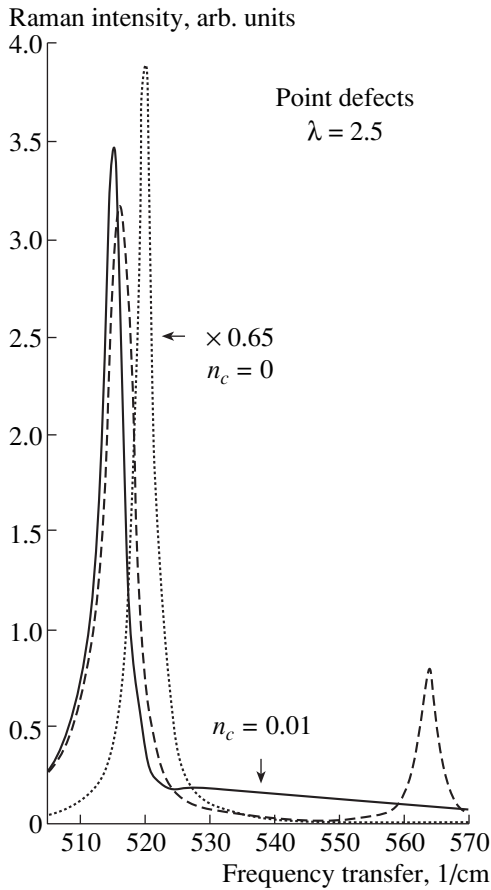
Raman intensity, arb. units
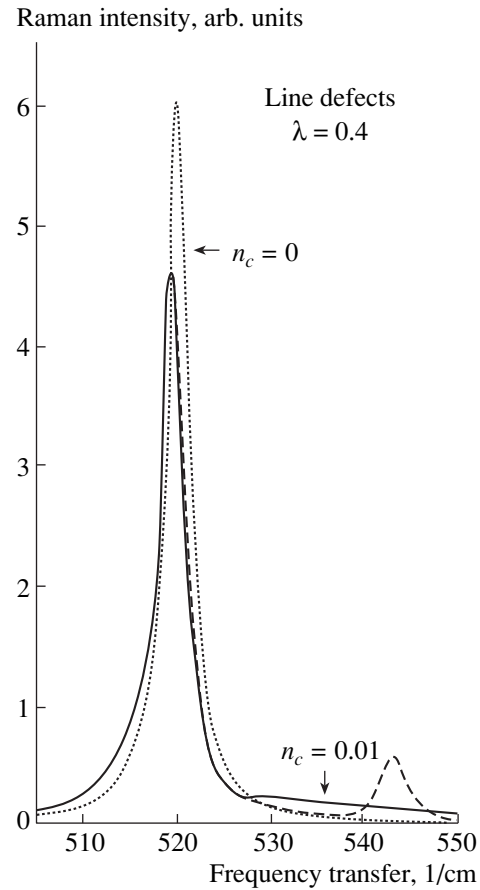

Fig. 3.

Raman intensity, arb. units

Fig. 4.

zian shape and becomes flatter on the low-frequency side (Figs. 1, 2). This effect was observed for longitudinal optical phonons in SiC [2] (see Fig. 2 in the first article quoted in [2]).

The behavior of the cross section changes significantly when the quantity $1/\lambda^*$ passes through zero. Localized states appear to the right of the boundary of the continuous spectrum for $\lambda > 1$ in the case of point defects and for $\lambda > 1/\ln(\kappa^2/\omega_0\Gamma^{intr})$ in the case of line defects (see Figs. 3, 4); this corresponds to the vanishing of the real parts of the denominators in (2) and (3). It should be emphasized that the results are qualitatively different for different dimensionalities of defects. At point defects, localized states arise only if the coupling constant exceeds a finite critical value. At line defects, localized states can emerge in the case of weak coupling owing to a large value of $\kappa^2/\omega_0\Gamma^{intr} \simeq \omega_0/\Gamma^{intr}$; for this, it is sufficient that the radius of the emerging bound state is less than the mean free path of phonons that belong to some neighborhood of the boundary of the continuous spectrum. The above distinction is in accord with the well-known statement in quantum mechanics that there is a bound state in a shallow two-dimensional potential well.

The data in Figs. 3 and 4 reveal that the accurate result represented by solid curves differs considerably from that obtained in the unrenormalized approximation and shown by dashed curves in the region where localized states contribute. In the accurate calculation, the maximum that was found in the unrenormalized approximation is washed out, transforming into a plateau extending to the boundary of the continuous spectrum. As a matter of fact, this effect represents resonance interaction between states of the continuous spectrum and localized states. In interpreting experimental data, it is often stated that, due to the effect of defects, the line shape seems to develop a shoulder similar to that depicted in Figs. 3 and 4.

One of the most intriguing examples, however, is provided by diamond-like substances, which show a line at 1600 cm^{-1}, as in the case of graphite, or a line at 1300 cm^{-1}, as in the case of diamond. When defects are added to graphite, the low-frequency wing of the line at 1600 cm^{-1} flattens (see Figs. 1 and 2 in [10]) in just the same way as depicted in Figs. 1 and 2 of the present study. But if it is diamond samples that are impaired, a similar change is suffered by the high-frequency wing of the line at 1300 cm^{-1}—it becomes more gently sloping (see Fig. 7 in [10] and Fig. 2 in [11]). The explana-

tion is based on the fact that quite an atypical situation is realized in diamond—in the optical-phonon band, there is a minimum at the center of the Brillouin zone [12]. So far, we have assumed in this study that the optical-phonon branch has a maximum at the center of the Brillouin zone. For the case of a minimum, the sign of $\omega^2 - \omega_0^2$ must be reversed in all the above statements, which leads to results explaining the diamond anomaly.

In conclusion, it is worth noting that all the features considered in the present study emerge even in the linear approximation in the defect concentration and are due to the finiteness of the intrinsic lifetime of optical phonons. As to fluctuations in the defect distribution (cluster corrections), they contribute only in the next (quadratic) approximation.

ACKNOWLEDGMENTS

REFERENCES

1. A. Göbel, T. Ruf, J. M. Zhang, *et al.*, Phys. Rev. B **59**, 2749 (1999).

2. L. A. Falkovsky, J. M. Bluet, and J. Camassel, Phys. Rev. B **55**, R14697 (1997); Phys. Rev. B **57**, 11283 (1998).

3. I. M. Lifshits, Zh. Éksp. Teor. Fiz. **17**, 1017 (1947); I. M. Lifshits, Nuovo Cimento Suppl. **3**, 716 (1956); Usp. Fiz. Nauk **83**, 617 (1964) [Sov. Phys. Usp. **7**, 571 (1965)].

4. M. A. Ivanov and Yu. G. Pogorelov, Zh. Éksp. Teor. Fiz. **72**, 2198 (1977) [Sov. Phys. JETP **45**, 1155 (1977)].

5. T. R. Kirkpatrick, Phys. Rev. B **31**, 5746 (1985).

6. Yu. M. Kagan and Yu. A. Ioselevskiĭ, Zh. Éksp. Teor. Fiz. **45**, 819 (1963) [Sov. Phys. JETP **18**, 562 (1963)].

7. I. Ya. Polishchuk, A. L. Burin, and L. A. Maksimov, Pis'ma Zh. Éksp. Teor. Fiz. **51**, 644 (1990) [JETP Lett. **51**, 730 (1990)].

8. A. A. Abrikosov, L. P. Gor'kov, and I. E. Dzyaloshinskiĭ, *Methods of Quantum Field Theory in Statistical Physics* (Nauka, Moscow, 1962; Prentice-Hall, Englewood Cliffs, 1963).

9. L. A. Falkovsky, Zh. Éksp. Teor. Fiz. **117** (2000) (in press) [JETP **90** (2000) (in press)].

10. J. Wagner, M. Ramsteiner, Ch. Wild, and P. Koidl, Phys. Rev. B **40**, 1817 (1989).

11. J. W. Ager, III, D. K. Veirs, and G. M. Rosenblatt, Phys. Rev. B **43**, 6491 (1991).

12. M. Schwoerer-Böhning, A. T. Macrander, and D. A. Arms, Phys. Rev. Lett. **80**, 5572 (1998).

Translated by A. Isaakyan

CONDENSED
MATTER

Scaling Analysis of the Magnetic Field–Tuned Quantum Transition in Superconducting Amorphous In–O Films[1]

V. F. Gantmakher*, M. V. Golubkov, V. T. Dolgopolov,
G. E. Tsydynzhapov, and A. A. Shashkin

Institute of Solid-State Physics, Russian Academy of Sciences, Chernogolovka, Moscow oblast, 142432 Russia
*e-mail: gantm@issp.ac.ru
Received January 27, 2000

Abstract—We studied the magnetic field–tuned superconductor–insulator transition (SIT) in amorphous In–O films with different oxygen contents and, hence, different electron densities. Whereas the two-dimensional scaling behavior was confirmed for the states of the film near the zero-field SIT, the SIT scenario changed for the deeper states in the superconducting phase; in addition to the scaling function describing the conductivity of the fluctuation-induced Cooper pairs, the temperature-dependent contribution to the film resistance emerged. This contribution can originate from the conductivity of normal electrons. © *2000 MAIK "Nauka/Interperiodica".*

PACS numbers: 74.20.Mn; 74.25.Dw

Scaling analysis is an important experimental tool for studying quantum phase transitions. For the two-dimensional (2D) disordered superconductors, along with the zero-field superconductor–insulator transition (SIT) driven by the disorder change in a film, a SIT induced by the normal magnetic field also occurs. The scenario of the field-induced 2D quantum SIT was proposed in [1]: at zero temperature, the normal magnetic field alters the state of a disordered film from superconducting at low fields to metallic at the critical field $B = B_c$, with the universal sheet resistance R_c close to $h/4e^2 \simeq 6.4$ kΩ, and to the insulating state at fields $B > B_c$. The SIT was supposed to be continuous, with the correlation length of quantum fluctuations ξ diverging as $\xi \propto (B - B_c)^{-\nu}$, where the critical index $\nu > 1$. At nonzero temperatures, the size of quantum fluctuations is restricted by the dephasing length $L_\phi \propto T^{-1/z}$, where the dynamical critical index z determines the characteristic energy $U \sim \xi^{-z}$ and is expected to be equal to $z = 1$ for SIT. The ratio of these two length parameters defines the scaling variable u such that near the transition point $(T = 0, B_c)$ all $R(T, B)$ data should fall on a curve for a universal function of u

$$R(T, B) \equiv R_c r(u), \quad u = (B - B_c)/T^{1/z\nu}. \quad (1)$$

Although small in the scaling region, temperature-dependent corrections with a leading quadratic term are expected to the critical resistance R_c [1, 2].

The above theoretical description is based on the electron-pair localization concept supported by a recent publication [3]. In that paper, it was shown for the 2D superconducting films with sufficiently strong disorder

that the region of fluctuation superconductivity, where the localized electron pairs (also called bosons [1] and cooperons [3]) occur, should extend down to zero temperature. In this region, the unpaired electrons are supposed to be localized because of the disorder in the film.

The theory of field-driven 3D quantum SIT has not been developed so far. The idea of considering quantum SIT for the disordered 3D systems in zero magnetic field in terms of charged boson localization [4] was at first not accepted, because the region of fluctuation superconductivity was assumed to be small. In fact, as was shown later in [5], the fluctuation region enlarges as the edge of single-electron localization is approached. This provides an opportunity to apply the scaling relation deduced for the 3D boson localization [6] to the field-induced SIT description

$$R(T, u) \sim T^{-1/z} \bar{r}(u), \quad (2)$$

where $\bar{r}(u)$ is a universal function and the scaling variable u is assumed to have the same form as defined by (1). From (1) and (2), it follows that in the vicinity of B_c the $R(B)$ isotherms are straight lines with slopes

$$\frac{\partial R}{\partial B} \propto T^{-(d-2+1/\nu)/z}, \quad (3)$$

where d is the system dimensionality. Since the resistance behaves in (1) and (2) in very different fashions, the problem of film dimensionality is of major importance.

The data obtained in the experimental studies of a-In–O [7], a-Mo–Ge [8], and a-Mo–Si [9] films followed by 2D scaling relation (1), except for the universality of the R_c value, and thus confirmed the existence of quan-

---

[1] This article was submitted by the authors in English.

tum SIT. The resistance drop observed for a-In–O films at high fields was also explained in the framework of localized bosons [10, 11]. On the other hand, the scaling was found to fail for the ultrathin Bi films. This was interpreted as evidence for the crossover between different flux–flow regimes [12].

In this work, we carried out a detailed study of the scaling relations near the field-induced SIT for different states of an amorphous In–O film. We have found that 2D scaling relation (1) holds for the film states near the zero-field SIT but progressively fails upon departure from it. This failure is manifested by the appearance of the extra temperature-dependent term in the film resistance.

The experiments were performed with 200-Å-thick a-In–O films grown by electron-gun evaporation of a high-purity In_2O_3 target onto a glass substrate.[2] This material proved to be very useful for investigations of the transport properties near the SIT [7, 10, 13–15]. Oxygen deficiency with respect to the fully stoichiometric insulating In_2O_3 compound causes the film conductivity. By changing the oxygen content, one can cover the range from a superconducting material to an insulator with activated conductance [14]. The methods for the reversible change of the film state are described in detail in [10]. To reinforce the superconducting properties of our films, we used heating in vacuum to a temperature of 70–110°C until the sample resistance became saturated. To shift the state in the opposite direction, the film was exposed to air at room temperature. Since the film remains amorphous during these manipulations, it is natural to assume that the treatment used results mainly in a change in the total carrier concentration n and that there is a certain critical concentration n_c corresponding to the zero-field SIT.

The low-temperature measurements were carried out using a four-terminal lock-in technique at a frequency of 10 Hz on two experimental setups: a He^3-cryostat down to 0.35 K or an Oxford TLM-400 dilution refrigerator in the temperature range 1.2 K–30 mK. The ac current was equal to 1 nA and corresponded to the linear response regime. The aspect ratio for the samples was close to unity.

We investigated three different homogeneous states of the same a-In–O film.[3] We characterize the sample state by its room-temperature resistance R_r. Assuming that the disorder is approximately the same for all states, we have for the carrier density $n \propto 1/R_r$; i.e., the

Parameters of the states studied for the sample

State	R_r, kΩ	R_c, kΩ	B_c, T	α, K^{-1}
1	3.4	7.8	2.2	0
2	3.1	8	5.3	−0.1
3	3.0	9.2	7.2	−0.6

smaller R_r, the deeper the state in the superconducting phase and, hence, the larger the value of B_c. The parameters of the states investigated are listed in the table. State 1 is closest to the zero-field SIT, and state 3 is the deepest in the superconducting phase.

The sets of isomagnetic curves $R(T)$ for all states studied are depicted in Fig. 1. For each set, the curves can be roughly divided into two groups according to the sign of the second derivative: the positive (negative) sign corresponds to the insulating (superconducting) behavior. In what follows, the isomagnetic curve $R_c(T)$ designating the boundary between superconductor and insulator and corresponding to the boundary metallic state at $T = 0$ is referred to as the separatrix. Whereas it is easy to identify a horizontal separatrix for state 1 in accordance with (1), the fan and separatrix are "tilted" for states 2 and 3; i.e., each of the curves in the lower part of the fan has a maximum at a temperature T_{max} that shifts with B. To determine the separatrix $R_c(T)$, one should extrapolate the maximum position to $T = 0$. To do this, it is desirable to know the extrapolation law, because the accessible temperature range is restricted.

The absence of a horizontal separatrix for states 2 and 3 can also be established from the behavior of isotherms $R(B)$ (Fig. 2). As seen from Fig. 2, the isotherms for state 1 intersect at the same point (B_c, R_c), whereas those for state 3 form an envelope.

To determine B_c and R_c for states 2 and 3, we use the simplest linear extrapolation to $T = 0$ for the functions $R(T_{max})$ and $B(T_{max})$ (see Fig. 4). The open symbols correspond to the maximum positions on the isomagnetic curves (Fig. 1), and the filled symbols represent the data obtained from the intersections of the consecutive isotherms[4] (Fig. 2); if two consecutive isotherms for close temperatures T_1 and T_2 intersect at a point (B_i, R_i), the isomagnetic curve for the field B_i reaches its maximum $\approx R_i$ at $T_{max} \approx (T_1 + T_2)/2$. As seen from Fig. 4, the $B(T_{max})$ dependence is weak, so we believe that the linear extrapolation would suffice to determine B_c. By contrast, the accuracy of determination of R_c is poor.

The derivative $\partial R/\partial B$ near B_c is shown as a function of temperature in Fig. 3. Within the experimental accuracy, the exponents turned out to be identical for the film states 1 and 3, in agreement with the results

---

[2] The films were kindly presented by A. Frydman and Z. Ovadyahu from Jerusalem University.

[3] Observation of the so-called quasi-reentrant states for the field-driven SIT was reported in [7, 15, 16] and explained by the inhomogeneities and single-particle tunneling between superconducting grains [16]. This interpretation was supported in our experiments by the fact that the quasi-reentrant behavior observed for some film states disappeared upon the annealing of the sample in vacuum for several additional hours after its resistance had been saturated. We do not discuss quasi-reentrant states in this paper.

[4] A similar extrapolation procedure for determining R_c was employed in [17], where the metal–insulator transition in a 2D electron system was studied and the carrier density was used as a driving parameter.
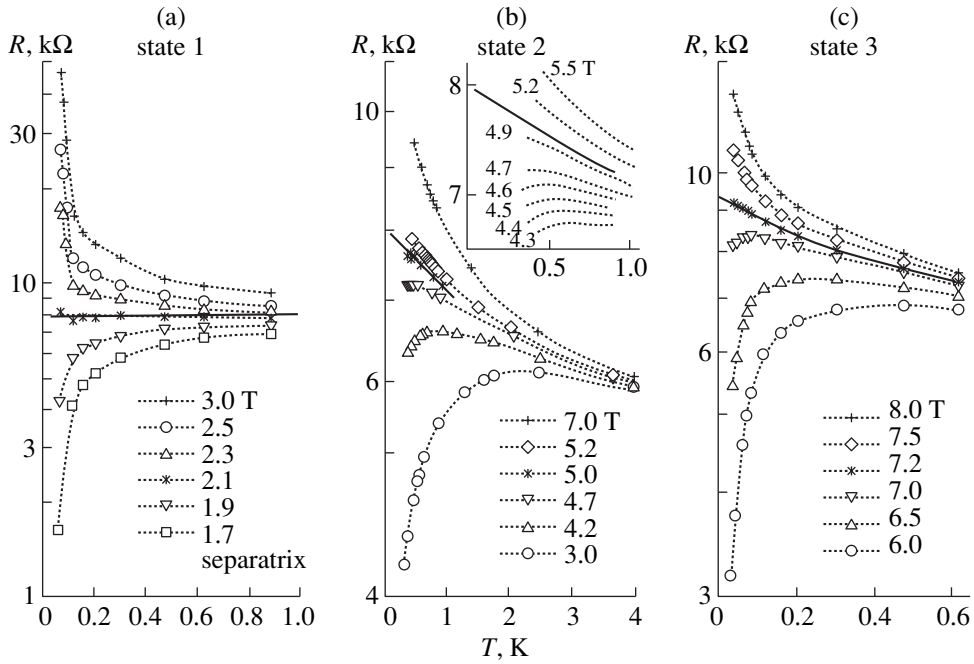
Fig. 1. Temperature-dependent resistances for the states studied at different magnetic fields. The separatrices $R_c(T)$ are shown by solid lines. For state 2, a close-up view of the critical region is displayed in the inset.
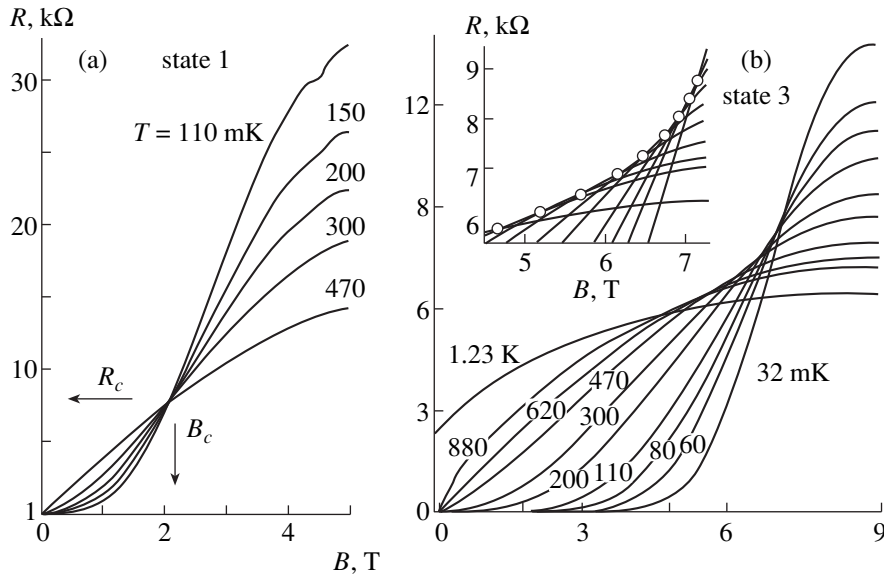

Fig. 2. Isotherms in the (B, R) plane for states (a) 1 and (b) 3. The curve intersection region for state 3 is blown up in the inset. The circles mark the crossing points of the isotherms with neighboring temperatures.

obtained in [7, 8], where the authors claimed observation of the field-induced 2D SIT for the states close to the zero-field SIT. This fact counts in favor of the 2D SIT scenario for the deeper film states of the superconducting phase as well.

Knowing B_c and the scaling exponent, we can replot the experimental data as a function of scaling variable

u (Fig. 5). As seen from Figs. 5a and 5b, the data for state 1 collapse onto a single curve, whereas for state 3 we obtain a set of similar curves shifted along the vertical axis. Subtracting the linear temperature term $R_c\alpha T$ (where α is a factor) formally from $R(T, B)$, we reveal the 2D scaling behavior for state 3 (Fig. 5c). Note that the procedure of dividing the experimental data in
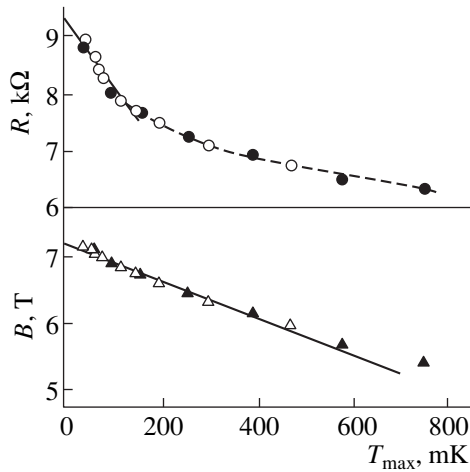
Fig. 3. $R(T_{max})$ and $B(T_{max})$ dependences, as determined from the data in Fig. 1c (open symbols) and Fig. 2b (filled symbols). The values of R_c and B_c are obtained by linear extrapolations (solid lines). The dotted line is a guide to the eye.
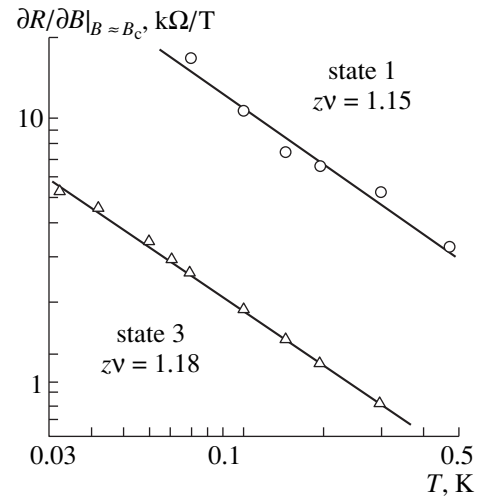
Fig. 4. Behavior of $\partial R/\partial B$ with temperature for states 1 and 3. The values of exponent $z\nu$ are indicated.
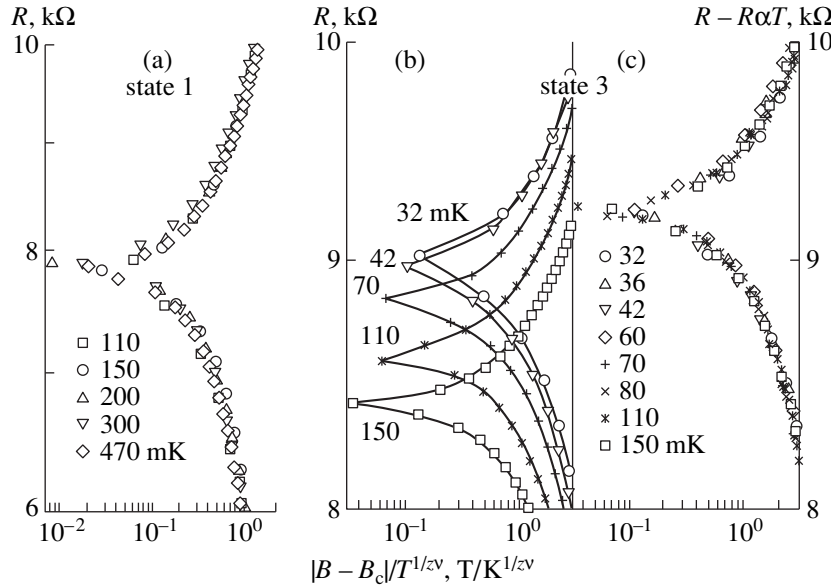
Fig. 5. Scaling plots for (a) state 1 and (b) for state 3 without and (c) with the linear temperature term.

Fig. 5b by $R_c(T)$, which corresponds to formula (2) for the 3D scaling, has not met with success.

Thus, we find that the 2D scaling holds for the states near the zero-field SIT, while the data for the deeper states of the superconducting phase are best described by relation (1) with an additive temperature-dependent correction $f(T)$:

$$R(T, B) \equiv R_c[r(u) + f(T)]. \qquad (4)$$

To get a basis for the formal analysis of the experimental data, one should answer two questions:

(i) whether our film is really 2D, and (ii) what is the physical origin for the temperature dependence of $R_c(T)$. In the first case, we need to compare film thickness h with the characteristic lengths. These are the coherence length $\xi_{sc} = c\hbar/2eB_{c2}l$ (where l is the mean free path in the normal state) in the superconducting state and the dephasing length $L_\phi(T) \simeq \hbar^2/m\xi_{sc}T$ [1, 2] that restricts the diverging correlation length ξ in the vicinity of quantum SIT. Knowing the film resistance $R \approx 5$ kΩ in the normal state at $T \approx 4$ K and assuming that we deal with an amorphous 3D metal in which the

mean free path is normally close to the lowest possible value $l \approx 1/k_F$, we estimate the length $l \approx 8$ Å. If we roughly estimate the field B_{c2} at $B_c = 7.2$ T, as was found for state 3, we get the upper limit for $\xi_{sc} \sim 500$ Å and the value $L_\phi \sim 400$ Å at $T = 0.5$ K. This confirms the 2D scenario of quantum SIT, although in the normal state the film turns out to be 3D.

As to the temperature-dependent $R_c(T)$, the conductivity of the film near B_c at finite temperatures should include a contribution from the localized normal electrons, in addition to the conductivity caused by the diffusion of the fluctuation-induced Cooper pairs [3, 8]. It is the normal electron conductivity that explains the nonuniversality of the critical resistance [8] and the additional term in (4). We write this term in the general form, because the linear extrapolation used is likely to break in the vicinity of $T = 0$.

Thus, all the experimental observations can be reconciled with the 2D scaling scenario. Curiously, the same scaling behavior was established for a parallel magnetic field [18]. Although not in favor of the 2D concept, this fact can also indicate that the restrictions imposed by the theory [1] are too severe.

It is worth mentioning an alternative way of constructing the $f(T)$ term in (4): introduction of the temperature-dependent field $B_c(T)$ defined through the constancy of R_c. Formally, both ways are equivalent and correspond to shifting the isotherms in Fig. 2 either along the R-axis or along the B-axis, so that a common crossing point is attained in the vicinity of the transition. Unlike the normal behavior of the critical fields in superconductors, the $B_c(T)$ thus defined increases with temperature. This can be interpreted in terms of the temperature-induced boson delocalization.

In summary, in the experiments with a-In–O films with different oxygen contents, a change of the field-driven 2D SIT scenario was observed as the film state departed from the zero-field SIT. For the deep film states in the superconducting phase, the temperature-dependent contribution to the film resistance emerges, in addition to the universal function of a scaling variable that describes the conductivity of fluctuation-induced Cooper pairs. This contribution can be attributed to the conductivity of normal electrons.

REFERENCES

1. M. P. A. Fisher, Phys. Rev. Lett. **65**, 923 (1990); M. P. A. Fisher, G. Grinshtein, and S. M. Girvin, Phys. Rev. Lett. **64**, 587 (1990).
2. S. L. Sondhi, S. M. Girvin, J. P. Carini, and D. Shahar, Rev. Mod. Phys. **69**, 315 (1997).
3. A. Larkin, Ann. Phys. (Leipzig) **8**, 785 (1999).
4. A. Gold, Z. Phys. B **52**, 1 (1983).
5. L. Bulaevskiĭ, A. Varlamov, and M. Sadovskiĭ, Fiz. Tverd. Tela (Leningrad) **28**, 1799 (1986) [Sov. Phys. Solid State **28**, 997 (1986)].
6. M. P. A. Fisher, P. B. Weichman, G. Grinshtein, and D. S. Fisher, Phys. Rev. B **40**, 546 (1989).
7. A. F. Hebard and M. A. Paalanen, Phys. Rev. Lett. **65**, 927 (1990).
8. A. Yazdani and A. Kapitulnik, Phys. Rev. Lett. **74**, 3037 (1995).
9. S. Okuma, T. Terashima, and N. Kokubo, Solid State Commun. **106**, 529 (1998).
10. V. F. Gantmakher, M. V. Golubkov, J. G. S. Lok, and A. K. Geim, Zh. Éksp. Teor. Fiz. **109**, 1765 (1996) [JETP **82**, 951 (1996)].
11. V. F. Gantmakher, M. V. Golubkov, V. T. Dolgopolov, *et al.*, Pis'ma Zh. Éksp. Teor. Fiz. **68**, 337 (1998) [JETP Lett. **68**, 363 (1998)].
12. J. A. Chervenak and J. M. Valles, Jr., cond-mat/9909329.
13. M. A. Paalanen, A. F. Hebard, and R. R. Ruel, Phys. Rev. Lett. **69**, 1604 (1992).
14. D. Shahar and Z. Ovadyahu, Phys. Rev. B **46**, 10917 (1992).
15. J. J. Kim, J. Kim, and H.-L. Lee, Phys. Rev. B **46**, 11709 (1992).
16. Y. Liu, D. B. Haviland, B. Nease, and A. M. Goldman, Phys. Rev. B **47**, 5931 (1993).
17. Y. Hanein, D. Shahar, J. Yoon, *et al.*, Phys. Rev. B **58**, R7520 (1998).
18. V. F. Gantmakher, M. V. Golubkov, V. T. Dolgopolov, *et al.*, Ann. Phys. (Leipzig) **8** (SI), 73 (1999).

CONDENSED
MATTER

Neutron Diffraction Evidence for the Spin-Reorientational Transition in FeBO₃ at High Pressures

V. P. Glazkov, V. V. Kvardakov*, and V. A. Somenkov

Russian Research Centre Kurchatov Institute, pl. Kurchatova 1, Moscow, 123182 Russia
*e-mail: kvardako@isssph.kiae.ru
Received January 27, 2000

Abstract—The spin-reorientational transition from the state with "easy-plane" anisotropy to the state with "easy-axis" anisotropy—a pressure analogue of the Morin temperature transition in hematite—was detected in iron borate at a pressure of $P \sim 17$ kbar at room temperature by the neutron diffraction method. © 2000 MAIK "Nauka/Interperiodica".

PACS numbers: 75.30.Kz; 61.12.Ex; 75.25.+z

At temperatures below the Neél point $T_N \cong 348$ K, iron borate FeBO₃ is a weak ferromagnet with anisotropy of the "easy-plane" type [1]. The magnetic moments of its sublattices lie in the crystallographic (111) plane and are almost mutually antiparallel. The noncollinearity of these moments is caused by weak relativistic (spin–lattice and magnetic dipole) interactions and by specific features of magnetic symmetry of the crystal [2] and gives rise to a small nonzero ferromagnetic moment.

Hematite (α-Fe₂O₃) is isomorphous with iron borate at room temperature and is also a weak ferromagnet with anisotropy of the easy-plane type, but it undergoes spin-reorientational transition (Morin transition [3]) upon cooling below the $T_M \cong 250$ K temperature, as a result of which the magnetic moments of sublattices are aligned with the crystallographic [111] axis, so that the crystal becomes an antiferromagnet with anisotropy of the easy-axis type [4]. The phenomenological theory suggests [2] that the Morin transition is due to the change in sign of the uniaxial magnetic anisotropy constant.

It has been established that the hydrostatic pressure raises the Morin transition temperature [5, 6]. It was predicted that pressure could induce the transition even at room temperature [7]: the θ angle between the magnetic moments and the [111] axis should decrease with the buildup of pressure up to a certain critical value, after which the angle should jumpwise turn to zero. However, although the θ angle was found to experimentally decrease with pressure [8], no complete transition to the easy-axis phase was observed up to a pressure of 100 kbar.

Considering that the magnetic structures of iron borate and hematite are similar, we assumed that external pressure could induce the Morin-type spin-reorientational transition in FeBO₃ as well, where such a tran-

sition was not observed in the absence of pressure. It was thus the purpose of this work to investigate the pressure effect on the magnetic structure of iron borate.

To determine magnetic structure, neutron diffraction ($\lambda = 2.343$ Å) was measured on a DISK diffractometer [9] on an IR-8 reactor at the Russian Research Centre Kurchatov Institute. The experiment was conducted with a powder of FeBO₃ at pressures up to 50 kbar. Pressure was produced with the use of sapphire anvils [10] and measured from the shift of a ruby fluorescence line. The sample volume between the anvils was ~1 mm³. The characteristic time of measuring the diffraction curve was 24 h at a reactor power of about 5 MW.

The diffraction curve exhibits peaks corresponding to the scattering from the magnetic and nuclear sublattices and from both sublattices simultaneously (mixed reflections). No new diffraction peaks appear with pressure buildup, but the intensities of the magnetic peaks change appreciably. For example, the intensity of the magnetic reflection (100) increased with pressure by ~1.7 times, whereas the intensity of the magnetic reflection (111) became virtually zero at a pressure of ~17 kbar (figure).

As is known, the intensity of magnetic reflection is proportional to the square of the sine of the angle between the atomic magnetic moment and the scattering vector [11]. Denoting the angle between the [111] axis and the magnetic moments of the sublattices by θ and the angle between the scattering vector and the [111] axis by Δ, one obtains the following expression for the intensity of magnetic reflections from the powder sample:

$$I \sim (1 - (\sin\Delta\sin\theta)^2/2 - (\cos\Delta\cos\theta)^2).$$

Taking into account that the Δ angles for the reflections (111) and (100) are equal to 0° and 72.4°, respectively,
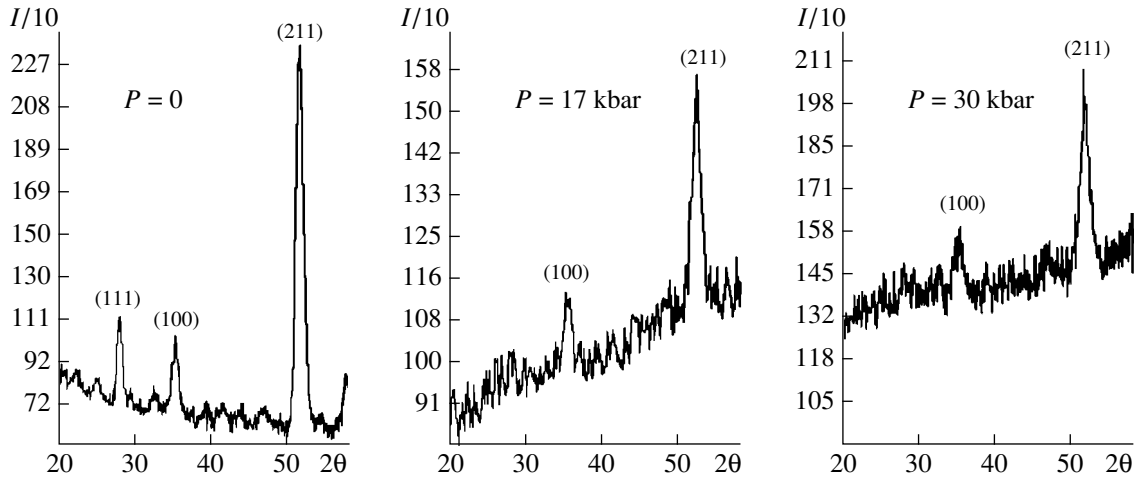
Neutron diffraction patterns for iron borate at different pressures.

one can estimate that the intensity of reflection (111) should turn to zero upon the reorientation of magnetic moments from easy plane ($\theta = 90°$) to easy axis ($\theta = 0$) (the magnetic moments become parallel to the scattering vector), while the intensity of reflection (100) should increase by a factor of $2\sin^2\Delta/(2 - \sin^2\Delta) \approx 1.66$, which is close to the experimentally measured value (table). The changes in intensities of other magnetic reflections are also in compliance with this transition model.

Thus, the experiment gives evidence for the occurrence of the pressure-induced spin-reorientational easy-plane–easy-axis transition in iron borate at room temperature, similar to the Morin transition in hematite. The phenomenological approach suggests that the magnetic anisotropy constant can change its sign not only under the action of temperature but also upon changing pressure. One can expect that the analogous pressure-induced spin-reorientational transitions can occur in other weak ferromagnets as well ($MnCO_3$, $CoCO_3$, $CsMnF_3$, etc.), whose atomic and magnetic structures are similar to those of iron borate and hematite.

Pressure-induced changes in the relative intensities of magnetic reflections (111) and (100) [$I_{(211)}$ is the intensity of the nuclear reflection]

P, kbar	$I_{(111)}/I_{(211)}$	$I_{(100)}/I_{(211)}$
0	0.22	0.19
17	≈ 0	0.29
30	≈ 0	0.32

REFERENCES

1. R. Diehl, W. Jantz, B. I. Nolang, *et al.*, in *Current Topics in Mater. Science*, Ed. by E. Kaldis (Elsevier, Amsterdam, 1984), Vol. 11, p. 241.
2. I. E. Dzyaloshinskiǐ, Zh. Éksp. Teor. Fiz. **32**, 1947 (1957) [Sov. Phys. JETP **5**, 1259 (1957)].
3. F. J. Morin, Phys. Rev. **78**, 819 (1950).
4. C. G. Shull, W. A. Strauser, and E. O. Wollan, Phys. Rev. **83**, 333 (1951).
5. N. Kawai and F. Ono, Phys. Lett. **21**, 279 (1966).
6. H. Umebayashi, B. C. Frazer, G. Shirane, *et al.*, Phys. Lett. **22**, 407 (1966).
7. A. S. Pakhomov, Fiz. Met. Metalloved. **25**, 769 (1968).
8. I. N. Goncharenko, J.-M. Mignot, G. Andre, *et al.*, High Press. Res. **14**, 41 (1995).
9. V. P. Glazkov, I. V. Naumov, V. A. Somenkov, *et al.*, Nucl. Instrum. Methods Phys. Res. A **264**, 367 (1988).
10. V. P. Glazkov and I. N. Goncharenko, Fiz. Tekh. Vys. Davleniǐ **1**, 56 (1991).
11. G. E. Bacon, *Neutron Diffraction* (Clarendon, Oxford, 1955; Inostrannaya Literatura, Moscow, 1957).

Translated by V. Sakun

CONDENSED
MATTER

Molecular-Dynamics Simulation of Rarefaction Waves in Media That Can Undergo Phase Transitions

V. V. Zhakhovskiĭ[1, 2], K. Nishihara[2], S. I. Anisimov[3, 4], and N. A. Inogamov[3]

[1]*Joint Institute of High Temperatures, Russian Academy of Sciences, Izhorskaya ul. 13/19, Moscow, 127412 Russia*
[2]*Institute of Laser Engineering, Osaka University Suita, Osaka 565-0871, Japan*
[3]*Landau Institute for Theoretical Physics, Russian Academy of Sciences, Chernogolovka,
Moscow oblast, 142432 Russia*
[4]*Department of Particle Physics, Weizman Institute of Science, 76100 Rehovot, Israel*
Received January 27, 2000

Abstract—The expansion of an instantly heated planar layer of condensed matter into a vacuum is investigated. It is shown that, as the result of a phase transition, a liquid shell characterized by a constant density and filled with matter in a two-phase state is formed in a rarefaction wave. By measuring the velocity of the shell and its density and mass, it is possible to obtain important information about the behavior of matter in the near-critical region of the phase diagram, where both experimental and theoretical investigations are complicated. Problems associated with the kinetics of the phase transition in rarefaction waves are investigated in detail. This investigation is based on a direct computer simulation of the dynamics of atoms and is free from any assumptions usually used in phenomenologically describing the fluctuation kinetics of the liquid–vapor transition. © 2000 MAIK "Nauka/Interperiodica".

PACS numbers: 47.40.-x; 62.50.+p; 64.70.Fx; 65.70.+y

The effect of femtosecond laser pulses on metal, semiconductor, and dielectric targets was studied experimentally in [1–3]. In those experiments, laser irradiation resulted in the heating of the surface layer. In metals, radiation is absorbed in a skin layer. Owing to the smallness of the electron heat capacity and a slow energy exchange between the electrons and the crystal lattice, overheating of the electron subsystem occurs [4–6]. Relaxation processes and electron thermal conductivity determine the temperature and the thickness of the layer that has been heated at the onset of hydrodynamic motion. The motion begins after a lapse of time τ_h since the propagation of the laser pulse. Under the conditions of the experiments reported in [1–3], $\tau_h \gg \tau_l$, where τ_l is the laser-pulse duration. Therefore, we can adopt the approximation where the motion begins at the instant $t = 0$, the matter in question being therefore at rest for $t < 0$ in this approximation. The initial density of the heated layer is equal to the normal density ρ_0 of condensed matter. In the cases of interest, the temperature T_0 is such that the adiabatic curve of relaxation intersects the liquid–pair equilibrium curve between the critical and triple points.

The ratio l_0/c_0 provides a natural time scale over which the sound wave traverses the heated layer. For $t < l_0/c_0$, the density $\rho(x, t)$ decreases monotonically in x toward a vacuum. In a medium capable of undergoing a phase transition, the interaction of rarefaction waves results in this profile gradually becoming nonmonotonic over a time interval of about l_0/c_0. Concurrently,

there arises a structure featuring a liquid shell that contains matter in a two-phase state [7–9]. A solution to the important problem of the Newton's rings that are observed in the experiments reported in [1–3] may be associated with interference at precisely this structure.

It should be emphasized that not only in experiments with femtosecond laser pulses can a liquid shell split off the expanding matter—this situation is quite general. In many other experiments, thermal or shock-wave loads result in the target acquiring such an amount of entropy that the adiabatic curve of relaxation intersects a binodal above the triple point but below the critical point. That part of matter which occurs within the liquid shell remains on the binodal for a time interval much greater than the acoustic time scale calculated by using the initial (large) speed of sound c_0. This offers the possibility of obtaining macroscopic volumes of matter (for example, metals) at an arbitrary point of the binodal.

Let us dwell on the problem of the interaction of rarefaction waves in a medium capable of undergoing a phase transition. This is necessary for explaining the results of a molecular-dynamics simulation. A typical phase diagram is shown in Fig. 1. Here, the equilibrium curve $Vcbti_0$ bounds the two-phase liquid–vapor region; the state V ($\rho = 0$, $p = 0$) represents a vacuum; c is the critical point; b is the point where the isentrope a intersects the binodal; the segment t corresponds to the triple point on the (T, p) plane; and i_0 is the initial state ($\rho = \rho_0$, $p = 0$) on the equilibrium curve. The physical
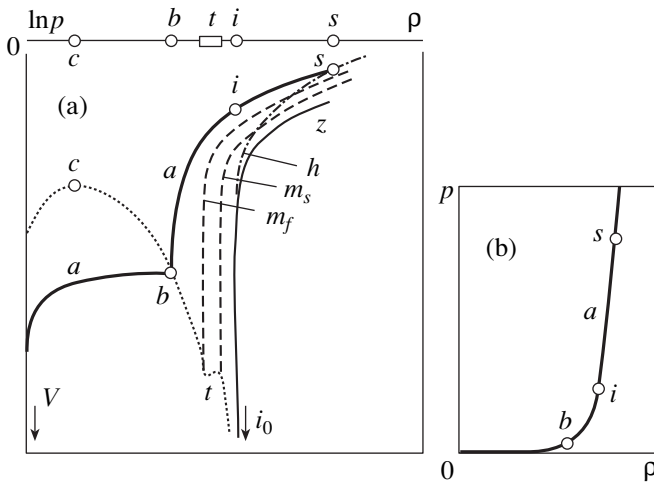
Fig. 1. (a) Phase diagram showing the binodal (dotted curve); two-phase melting region bounded by the curves m_s and m_f (dashed curves) on the sides of the solid and the liquid phase, respectively; and one curve (*sibV*) belonging to the one-parameter family of adiabatic curves covering the (ρ, p) plane above the curve z. (b) Decrease in the pressure as the result of adiabatic expansion [s, i, and b label points where the isentrope a intersects (s) the Hugoniot adiabatic curve, (i) the isochore ρ_0, and (b) the binodal].

region is bounded from below by the zero isotherm z; h is the Hugoniot adiabatic curve issuing from the point i_0, which corresponds to a normal state. In the case of instantaneous (isochoric) heating, matter goes over from the point i_0 to the point i whose position on the isochore ρ_0 is determined by the heating temperature. The $i_0 \longrightarrow s$ transition occurs in the case of a shock compression.

The reasons behind the separation of a liquid shell are clarified by Fig. 2, which shows the symmetric part of the flow process. The Lagrange coordinate m is reckoned from the symmetry plane. At $t = 0$, the matter being considered is at rest and the density and pressure are constant. At the first stage of expansion, the flow is self-similar over the entire region. In Fig. 2a, the segment sb_1 of the centered wave sb_1b_2M refers to the segment ib or sb of the isentrope a in Fig. 1. The cusp b is stretched into the segment b_1b_2 of the uniform flow (plateau). At stages 1 and 2, the points b_1 and b_2 are the limiting points on the sides of the single- and the two-phase medium, respectively. The tail b_2M at all stages and the region $0b_1$ of the two-phase flow at stage 3 correspond to the two-phase segment of the isentrope a. If the point b on the binodal (Fig. 2a) occurs at a pressure much less than its critical value, the mass of matter in the tail b_2M (evaporated mass) constitutes only a small fraction of the total mass.

At the second stage, the wave $0R$ reflected from the symmetry plane $m = 0$ propagates through the matter. Now the flow is self-similar only for $m > m_R(t)$, where m_R is the coordinate of the first characteristic of the reflected wave. At the instant t_f, the points R and b_1 merge and the third stage begins.

Figure 2b displays the graphs of the acceleration of Lagrange particles. If we disregard evaporated particles, which constitute the tail, the remaining particles can be broken down into two groups—that which comprises particles with Lagrange coordinates in the range $0 < m < m_{lw}$ and that which comprises particles with Lagrange coordinates in the range $m_{lw} < m < M$ (the subscript "lw" labels the coordinate referring to a liquid wall). Particles belonging to the $m > m_{lw}$ group form the
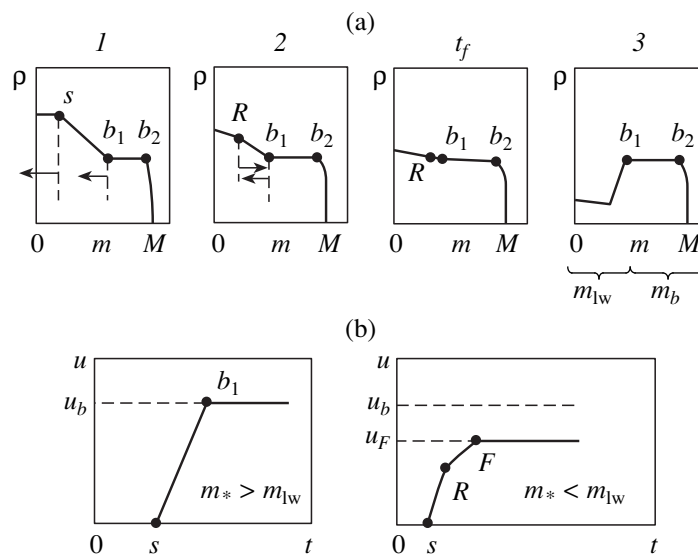

Fig. 2. (a) Three stages of expansion (m is the Lagrange coordinate, while M is the boundary with a vacuum). (b) Stages of the acceleration of matter particles belonging to (left panel) the liquid shell and (right panel) the internal liquid–vapor region.

liquid shell over the time interval $0 < t < t_f$. Particles from the $m < m_{lw}$ group do not reach the liquid shell. At the third stage, they occur in the region $0b_1$, which is characterized by a reduced density and is filled with a two-phase liquid–vapor mixture. Let us consider a particle with a coordinate m_* greater than m_{lw}. For $0 < t < t_s(m_*)$, it is at rest (Fig. 2b). For $t > t_s$, this particle is captured by the sb_1 wave shown in Fig. 2a. Over the time interval $t_s < t < t_{b1}$, the m_* particle is accelerated by the pressure gradient $\partial p(m_*, t)/\partial m$. At the instant t_{b1}, it reaches the point b_1 on the profile in Fig. 2a, its image reaching the point b on the phase diagram (Fig. 1a). After that, the gradient $\partial p/\partial m$ decreases sharply and the particle is no longer accelerated. Over the time of acceleration, the particle acquires the velocity u_b, entering the region of constant flow, b_1b_2 (Fig. 2a).

In the course of time, matter with coordinates $m < m_{lw}$ occurs in the two-phase region. It is at rest for $t < t_s$ and is accelerated by the sb_1 wave over the time interval $t_s(m) < t < t_R(m)$; for $t_R(m) < t < t_f(m)$, this matter has a smaller acceleration, but it is still pushed forward by the concerted effect of the incident and reflected rarefaction waves acting to the right and to the left, respectively. The pressure gradient is smaller in the region of two $0R$ waves than in the region of one Rb_1 wave. Concurrently, the velocity gradient $\partial u/\partial m$ is greater in the region of two waves. This gradient determines the rate of the decrease in the density with time. At the instant t_f, the image of the relevant particle on the phase diagram intersects the binodal, the pressure gradient decreases sharply, and the velocity at which this particle flies away reaches a maximum value $u_F(m)$. It is important that, because of the reduction in the acceleration due to the reflected wave, $u_F < u_b$ (Fig. 2b, right panel); therefore, all $m < m_{lw}$ particles cannot overtake the liquid layer.

All particles constituting the liquid shell move at a constant velocity u_b, and the density ρ_b of the shell remains constant in time. At the third stage, the velocity of particles with coordinates $0 < m < m_{lw}$ depends on the coordinate m, $u(0) = 0$ and $u(m) \longrightarrow u_b$ for $m \longrightarrow m_{lw}$. It follows that, for $m < m_{lw}$, the density continues decreasing for $t > t_f$. This is the reason behind the formation of the dip $0b_1$, a two-phase region where the density is reduced (Fig. 2a).

The above structure of the flow was obtained by solving the equations of gas dynamics. In doing this, it was assumed that the medium under study is in local thermodynamic equilibrium and that kinetic effects are inoperative. The validity of these assumptions is not quite obvious. A numerical experiment performed by the method of molecular dynamics provides an interesting possibility for testing the correctness of the gas-dynamics solution. Computational procedures on the basis of molecular dynamics are described in detail
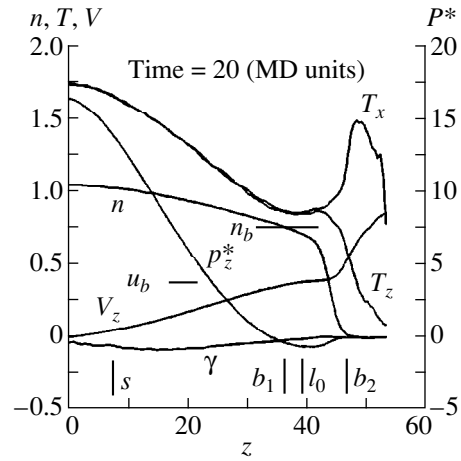
Fig. 3. Stages of rarefaction-wave motion toward the center (l_0 stands for the initial position of the boundary with a vacuum). Dashes indicate the positions of the basic details of the distributions calculated with the aid of the Ree polynomial equation of state [12] and with the aid of the Riemann invariant [8, 9]; s stands for the position of the first characteristic; b_1 and b_2 represent the boundaries of the plateau (Fig. 2a); and u_b and n_b are the velocity and density in the region of a uniform flow (plateau), respectively. We can see that the results of gas-dynamics calculations are in good agreement with the results of our simulation performed by the method of molecular dynamics.
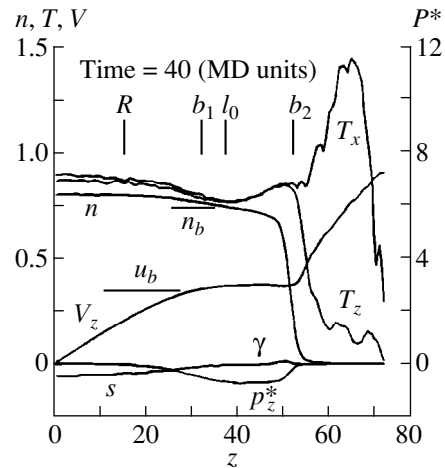

Fig. 4. Profiles of relevant quantities at the second stage of expansion at the instant $t = 0.7t_f$. The dash R indicates the position of the reflected characteristic (compare with Fig. 2a); the rest of the notation is identical to that in Fig. 3.

elsewhere [10, 11]. For this reason, we immediately proceed to formulate the problem and to describe the results of our simulation.

The results of a typical version of our calculations employing the Lennard-Jones potential of interaction between atoms $U(r) = 4\epsilon[(\sigma/r)^{12} - (\sigma/r)^6]$ are displayed in Figs. 3–8. The equation of state of this medium is well known (see, for example, [12, 13]). In particular, the critical parameters are $n_c \approx 0.36/\sigma^3$, $T_c \approx 1.36\epsilon$, and
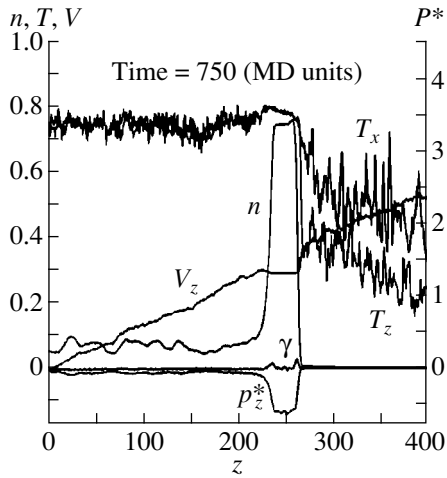
Fig. 5. Third stage of expansion ($t/t_f = 12.5$). The evolution of the cloud upon the instant of boiling t_f manifests itself in that the difference in the density between the liquid shell and the dip increases.
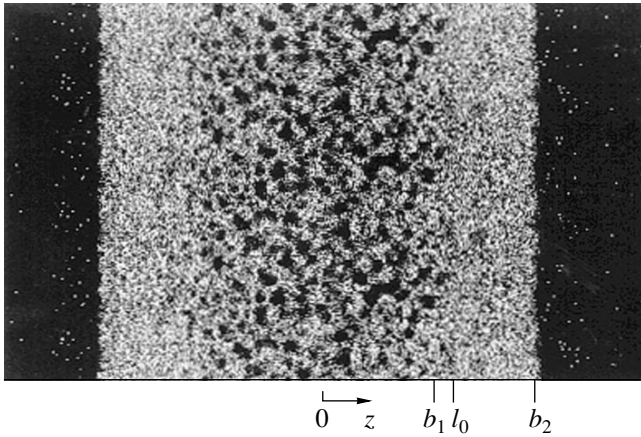
Fig. 6. Onset of a phase separation in the region of the would-be reduction in the density ($t/t_f = 1.16$). Points represent atoms. The arrow z indicates the direction of expansion. The figure was obtained by a repetition of three periods λ in the coordinate x, which is orthogonal to z. In this version of the calculation, the parameters n_0, T_0, and N_{at} were taken to have the same values as those in the main body of the text, but the geometric parameter was set to the different value of $2l_0/\lambda = 131\sigma/65.5\sigma$. The dashes indicate the position of the plateau according to the gas-dynamics calculation.

$p_c \approx 0.15\epsilon/\sigma^3$. The phase diagram of the model is qualitatively similar to that in Fig. 1a. We simulated the expansion of a planar layer into a vacuum. In the present calculation, the initial density and temperature were set to $n_0 = 1.05/\sigma^3$ and $T_0 = 1.8\epsilon$. The initial thickness of the layer $2l_0$ was taken to be 76σ. The initial number of atomic layers was then $2l_0/l_{at0} = 77$ ($l_{at0} = n_0^{-1/3}$). In the coordinates x and y, which are transverse

with respect to the direction of expansion (z axis), we imposed periodic boundary conditions with period $\lambda_x = \lambda_y = \lambda = 86\sigma$ (see Fig. 8). In our calculations, we varied, first, the values of n_0 and T_0; second, the geometric ratio $2l_0/\lambda$ within the range 0.5–4 (in order to estimate the effect of the side boundary conditions); and, third, the number of atoms N_{at} within the range 10^5–10^6. In the present version of the calculation, N_{at} is sufficiently large ($N_{at} = 590\,000$).

The objective of our simulation was to test the results of the gas-dynamic calculations reported in [7–9]. In particular, we aimed at clarifying the possible effect of metastable states on the dynamics of expansion. With this in view, we chose the initial values n_0 and T_0 in such a way as to ensure that (i) n_0 corresponded to the normal state of matter, (ii) the initial state was above the region of melting (Fig. 1a), (iii) the ratio p_0/p_c had a value close to those in the calculations from [7–9], and (iv) the adiabatic curve of relaxation intersected the binodal below the critical point but above the triple point.

Figures 3–5 show the evolution of distributions of hydrodynamic variables in the symmetric half of an expanding cloud. Figure 3 displays these data for the first stage illustrated in Fig. 2a. The rarefaction wave travels to the center, $t < l_0/c_0$; in the present version of the calculation, $l_0/c_0 = 25$ MD units (all values are presented here in MD units). Hereafter, V_z is the velocity at which matter flies away; n is the density; p_z^* is the virial component of the longitudinal pressure; $p_z = p_z^* + nT_z$ is the pressure along the z axis; $\gamma = p_z^* - p_x^*$; and T_z and T_x are, respectively, the longitudinal and the transverse temperature. The plateau b_1b_2 (Fig. 2a) clearly manifests itself in the profile of V_z in Fig. 3. It can be seen that the plateau corresponds to a liquid state ($p_z^* < 0$) and that, in the tail b_2M (Fig. 2a), atoms fly away in a free molecular regime.
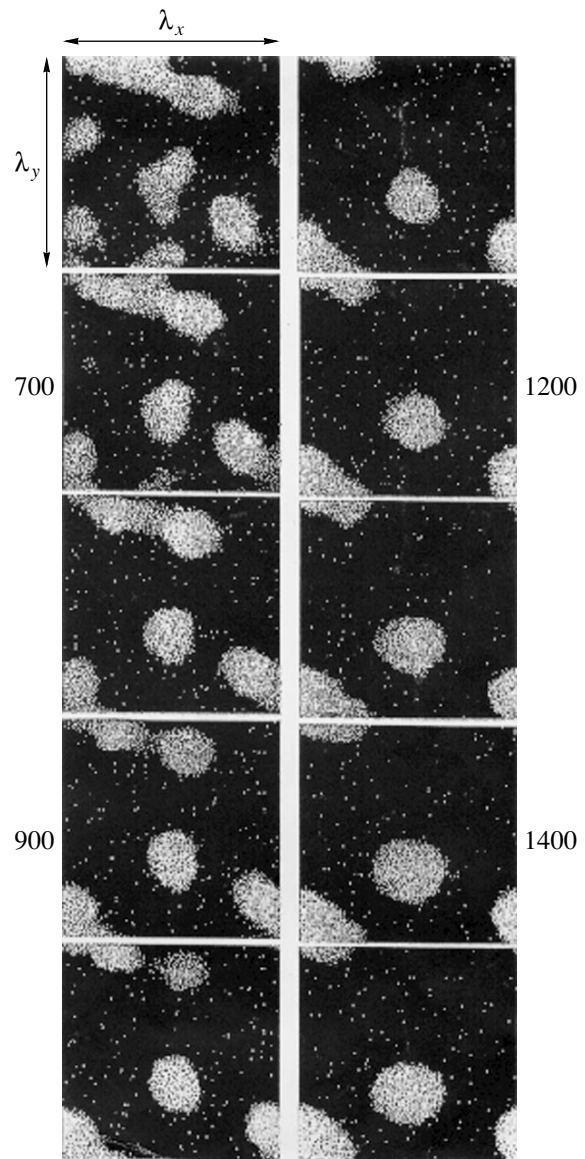
Figure 4 corresponds to the instant preceding t_f (for our choice of n_0, T_0, and l_0, we have $t_f = 60$ MD units). The plateau is clearly seen in the distributions of n, V_z, and p_z^* as well. At the instant t_f, the first characteristic R of the reflected wave reaches the plateau edge b_1 (Fig. 2a). As soon as this occurs, the matter boils over the entire region $0b_1$ of the would-be dip in the density (Fig. 6) and the third (last) stage begins. During its initial period ($t/t_f \approx 1$), the density n_h in the region of the would-be dip is virtually identical to the density n_b of the liquid shell. However, the ratio n_b/n_h increases with time. As a result, there arises a structure featuring a clear-cut shell (Fig. 5, profile of n, $t/t_f = 12.5$).

From an analysis of the results, it follows that, at all three stages, the density n_b and the temperature T_b in the region b_1b_2 remain constant and coincide with the val-
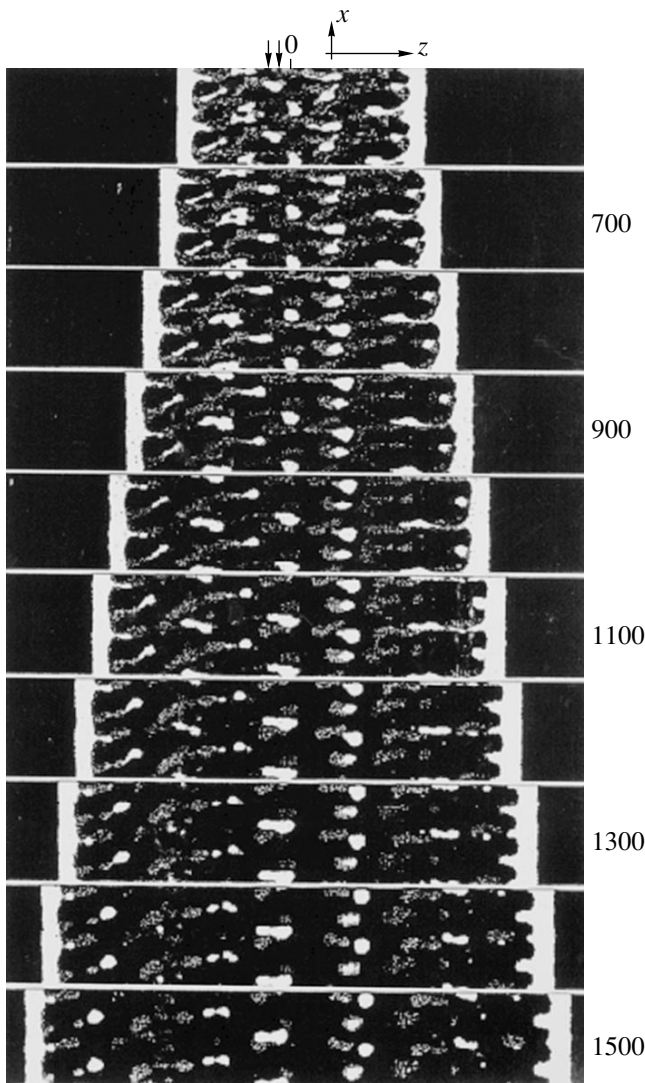
Fig. 7. Transformation of the two-phase mixture over a wide time interval. The time changes from top to bottom between $t = 600$ and 1500 MD units with a step of 100 MD units ($10 < t/t_f < 25$). The (x, z) plane is shown, and the expansion occurs along the z axis. Two periods λ along the x axis are repeated on each frame.

Fig. 8. Transverse (orthogonal to the z axis) cross section of the two-phase region. The square $x \times y = \lambda \times \lambda$, $\lambda = 86\sigma$, represents one period of the flow. The figure shows atoms occurring at a given instant of time in the gap $-40\sigma < z < -20\sigma$ indicated by two arrows in Fig. 7. Large round light spots are the cross sections of liquid fragments. Rare individual small points in the dark space between the fragments correspond to evaporated atoms. Time grows from top to bottom with a step of 100 MD units from $t = 600$ to 1000 MD units along the left column of the frames and then from 1100 to 1500 MD units along the right column in just the same way.

ues obtained by calculating the point at which the adiabatic curve intersects the binodal. At the values chosen in this calculation for n_0 and T_0, the temperature T_b only slightly exceeds the temperature T_t at the triple point ($T_b = 0.75$, $T_t = 0.68$). At this temperature, the density of the saturated vapor is much less than the density of the condensed matter. Over the entire time of integration ($t_{fin} = 1500$ MD units; see Figs. 7, 8), the tail remains nonequilibrium, featuring different longitudinal and transverse temperatures. The evaporated mass grows slowly, and the temperatures T_z and T_x gradually approach each other (compare Figs. 3 and 4 with

Fig. 5). The temperature T_x proved to be higher than the temperature T_b at early times, because a small fraction of atoms were evaporated over a short time interval from the commencement of integration to equilibration, when the temperature of the condensed matter was high (the initial temperature was higher than the critical one).

The initial stage of vapor-phase formation in the would-be low-density region $0b_1$ (Fig. 2a) is illustrated in Fig. 6. Over the entire time of integration, the matter of the liquid shell is free of vapor bubbles. Gradually, the fraction of the liquid phase in the two-phase layer $0b_1$ decreases and a liquid featuring bubbles (Fig. 6) breaks up into liquid fragments stretched in the direction of the motion. The impressive sequence of frames in Fig. 7 illustrates the process. The topology of fragmentation is clarified by Fig. 8. The two-phase mixture is bounded from the left and from the right by the walls of the liquid shell (Fig. 7). In the present calculation, the relative wall thickness was $\Delta z_{\mathrm{lw}}/l_0 = 0.73$. It is determined by the quantities n_0 and T_0. The mass of the two walls constitutes 54% of the total mass. The width and the mass do not change with time.

Here, it is appropriate to mention the study of Toxvaerd [14], who used the method of molecular dynamics to simulate the microstructure of a two-phase medium in the case of a uniform expansion. There, the mean-velocity profile linear in coordinates was specified even at $t = 0$. In the present study, the expansion of the layer begins from the state at rest. The velocity field is then formed self-consistently under the effect of rarefaction waves.

In the experiments reported in [1–3], the thickness of the heated layer amounted to a few hundred interatomic spacings, while the expansion time was a few nanoseconds. In the numerical experiment based on the method of molecular dynamics, the analogous quantities were an order of magnitude smaller. An analysis of the results of our simulation revealed, however, that the pattern following from gas-dynamic calculation can be formed even at such small scales.

REFERENCES

1. K. Sokolowski-Tinten, J. Bialkowski, A. Cavalleri, *et al.*, Proc. SPIE **3343**, 46 (1998).
2. K. Sokolowski-Tinten, J. Bialkowski, A. Cavalleri, and D. von der Linde, Appl. Surf. Sci. **127**–**129**, 755 (1998).
3. K. Sokolowski-Tinten, J. Bialkowski, A. Cavalleri, *et al.*, Phys. Rev. Lett. **81**, 224 (1998).
4. S. I. Anisimov, Zh. Éksp. Teor. Fiz. **54**, 339 (1968) [Sov. Phys. JETP **27**, 182 (1968)].
5. S. I. Anisimov, Ya. A. Imas, G. S. Romanov, and Yu. V. Khodyko, *Effect of High-Power Radiation on Metals* (Nauka, Moscow, 1970).
6. S. I. Anisimov and B. Rethfeld, Proc. SPIE **3093**, 192 (1997).
7. N. A. Inogamov, Yu. V. Petrov, S. I. Anisimov, *et al.*, Pis'ma Zh. Éksp. Teor. Fiz. **69**, 284 (1999) [JETP Lett. **69**, 310 (1999)].
8. S. I. Anisimov, N. A. Inogamov, A. M. Oparin, *et al.*, Appl. Phys. A **69**, 617 (1999).
9. N. A. Inogamov, S. I. Anisimov, and B. Rethfeld, Zh. Éksp. Teor. Fiz. **115**, 2091 (1999) [JETP **88**, 1143 (1999)].
10. V. V. Zhakhovskiĭ and S. I. Anisimov, Zh. Éksp. Teor. Fiz. **111**, 1328 (1997) [JETP **84**, 734 (1997)].
11. S. I. Anisimov, D. O. Dunikov, S. P. Malyshenko, and V. V. Zhakhovskiĭ, J. Chem. Phys. **110**, 8722 (1999).
12. F. H. Ree, J. Chem. Phys. **73**, 5401 (1980).
13. B. Smit, J. Chem. Phys. **96**, 8639 (1992).
14. S. Toxvaerd, Phys. Rev. E **58**, 704 (1998).

Translated by A. Isaakyan

Information for Authors

PACS numbers: 01.30.-y

The journal *Pis'ma Zh. Éksp. Teor. Fiz.* (and its English edition *JETP Letters*) publishes short papers that need to be urgently published and are of broad physical interest. These papers should report first observations of new physical phenomena or new fundamental theoretical results.

This journal accepts and publishes manuscripts submitted in Russian or English. All manuscripts submitted in English are put to a lingual test. If the English text appears unreadable, the Editorial Board may request that the authors submit the Russian variant of the manuscript for publication.

All articles in *JETP Letters* are published in English. The translation of manuscripts submitted in Russian, as well as the editing of manuscripts submitted in English, is performed by the International Academic Publishing Company (IAPC) "Nauka/Interperiodica."

The total length of any paper should not exceed six journal pages in the Russian edition. This length approximately corresponds to 20 KB in *LATeX* format, including 1 KB for each figure. You can estimate the manuscript length more accurately by preparing it according to an example that is available on the Web server for the journal (http://kapitza.ras.ru/journals/jetpl) by using the style file (jetpl.sty) available on the same server.

Manuscripts may be submitted to the Editorial Board by the following ways:

(1) Conventional mail to the following address: *Pis'ma Zh. Éksp. Teor. Fiz.*, ul. Kosygina 2, Moscow, 117334 Russia. A manuscript should be submitted in duplicate with figures on separate sheets (for half-tone figures, one additional copy should be submitted). Please append the e-mail and postal addresses (including the postal code), the office and home phone numbers, and the complete name and patronymic of the author to whom correspondence should be addressed. The authors of English manuscripts should also submit a floppy disk containing the text in the *LATeX* format.

(2) Electronic mail to the e-mail address letters@kapitza.ras.ru. In this case, each figure should be submitted in the form of an individual file in PostScript (*.ps), EncapsulatedPostScript (*.eps), or PaintBrush (*.pcx) formats.

Acceptance or rejection of a paper for publication is decided by the Editorial Board with a proposal from the Editorial Board member specialized in the appropriate section. A manuscript can be rejected if it is not topical enough, does not provide considerable development as compared to other publications in this field, considers a too specific subject, etc. As a rule, the referee reports on rejected papers are not sent. The authors may resubmit a rejected manuscript, appending it with an explanatory letter. In this case, the manuscript will be put under additional review.

The Editorial Board sends (or hand delivers if the authors live in Moscow) five reprints of the papers published in the Russian edition. The English version is sent to the authors in electronic mode by IAPC "Nauka/Interperiodica."

MANUSCRIPT PREPARATION

The first page of a manuscript should have the following form:

THE TITLE

Initials and Surnames of the Authors

Institutions where the authors work, including city and postal code (the e-mail address of one of the authors is desirable)

Text of the Abstract

PACS: … (Physics and Astronomy Classification Scheme, see Pis'ma Zh. Éksp. Teor. Fiz. **58** (7 and 9), (1993) [JETP Lett. **58** (7 and 9), (1993)]).

Then, after one empty line, the main text follows.

Because abstracts may now be distributed separately from the papers (data bases, online systems, etc.), the abstract text should be self-contained with no references or abbreviations but with understandable notation.

Abbreviations must be given in capital letters with no points and should be explained as they are first introduced. Footnotes in the main text must be numbered consecutively in the order of their appearance.

Cited references must be given in a general list at the end of a manuscript and should be numbered with an ordinal number (e.g., [1]) consecutively as they are mentioned in the main text. The reference to a journal article should cite the following: the initials and surnames of the authors, journal name, volume number (in boldface type), the first page of the paper, and year enclosed in parentheses. If an article is written by more than four authors, indicate only the first three, e.g.,

1. A. B. Ivanov, V. G. Petrov, I. M. Sergeev, *et al.*, Zh. Éksp. Teor. Fiz. **98**, 290 (1990) [JETP **71**, 161 (1990)].

The reference to books must cite the following: the initials and surnames of the authors, the complete book title, year and place of publication (in the case of translated books, give the information for the original in parentheses).

Use decimal points instead of commas. Three-vectors and dyadics with no arrow above them must be underlined with blue pencil.

We recommend that the authors preparing figures electronically adhere to the following rules: prepare figures in the frame; direct dashes on the axes inside the figure; when possible, use Arial font; use numerals (including those on the axes in an insert) and lower case letters with a height of 3–4% of the maximum figure size (height or width) of the figures; put measurement units on the axes in parentheses.

Examples of the preparation of manuscript and figures, as well as style file, are available on our Web server (http://kapitza.ras.ru/journals/jetpl).

The English variant proof is sent (via e-mail) to the author for agreement for a span of five days. If the author does not agree with the terminology used or decides that the translation of some sentences distorts their semantic meaning, he submits his proposals for changes. The author should not intrude into the lingual aspect of the translation. The absence of an answer from the author in above-indicated time is considered as the author's agreement with the text. If the author has no criticisms, he should inform the publisher about his agreement.

Translated by R. Tyapaev